1   Revision 2

2   Comparison of fluid processes in coexisting wolframite and quartz from a giant vein-

3   type tungsten deposit, South China: Insights from detailed petrography and LA-ICP-

4   MS analysis of fluid inclusions

5

6   Jun-Yi Pan, Pei Ni[†], Ru-Cheng Wang

7

8   State Key Laboratory for Mineral Deposits Research, Institute of Geo-Fluids, School of Earth

9   Sciences and Engineering, Nanjing University, Nanjing 210093, China

10

11   [†]Corresponding author (Pei Ni): peini@nju.edu.cn

12   Tel: +86 25 89680883 Fax: +86 25 89682393

13

14   Abstract:

15   Granite-related wolframite-quartz veins are the world's most important economic tungsten

16   mineralization style. Recent progress in revealing their hydrothermal processes has been greatly

17   facilitated by the use of infrared microscopy and laser ablation-inductively coupled plasma-mass

18   spectrometry (LA-ICP-MS) analysis of both quartz- and wolframite-hosted fluid inclusions.

19   However, owing to the paucity of detailed petrography, previous fluid inclusion studies on

20   coexisting wolframite and quartz are associated with a certain degree of ambiguity. To better

21   understand the fluid processes forming these two minerals, free-grown crystals of intergrown

22   wolframite and quartz from the giant Yaogangxian W deposit in South China were studied using

23   integrated in situ analytical methods including cathodoluminescence (CL) imaging, infrared

24   microthermometry, Raman microspectroscopy and fluid inclusion LA-ICP-MS analysis. Detailed

25   crystal-scale petrography with critical help from CL imaging shows repetition of quartz, wolframite

26   and muscovite in the depositional sequence, which comprises a paragenesis far more complex than

27   previous comparable studies. The reconstruction of fluid history in coexisting wolframite and quartz

28   recognizes at least four successive fluid inclusion generations, two of which were entrapped

29   concurrently with wolframite deposition.

30   Fluctuations of fluid temperature and salinity during precipitation of coexisting wolframite and

31   quartz are reflected by our microthermometry results, according to which wolframite-hosted fluid

32   inclusions do not display higher homogenization temperature or salinity than those in quartz.

33   However, LA-ICP-MS analysis shows that both primary fluid inclusions in wolframite and quartz-

34   hosted fluid inclusions associated intimately with wolframite deposition are characterized by strong

35   enrichment in Sr and depletion in B and As, compared to quartz-hosted fluid inclusions that are not

36   associated with wolframite deposition. The chemical similarity between the two fluid inclusion

37   generations associated with wolframite deposition implies episodic tungsten mineralization derived

38   from fluids exhibiting distinct chemical signatures. Multiple chemical criteria including

39   incompatible elements and Br/Cl ratios of fluid inclusions in both minerals suggest a magmatic-

40   sourced fluid with possible addition of sedimentary and meteoric water. Combined with

41   microthermometry and Raman results, fluid chemical evolution in terms of B, As, S, Sr, W, Mn, Fe

42   and carbonic volatiles collectively imply fluid phase separation and mixing with sedimentary fluid

43   may have played important roles in wolframite deposition, whereas fluid cooling and addition of Fe

44   and Mn do not appear to be the major driving factor.

45   This study also shows that fluid inclusions in both wolframite and coexisting quartz may contain
46   substantial amount of carbonic volatiles ($CO_2 \pm CH_4$) and H_3BO_3. Ignoring the occurrence of these
47   components can result in significant overestimation of apparent salinity and miscalculation of LA-
48   ICP-MS elemental concentrations. We suggest that these effects should be considered critically to
49   avoid misinterpretation of fluid inclusion data, especially for granite-related tungsten-tin deposits.
50
51   Key Words: wolframite-quartz vein, fluid inclusion petrography, LA-ICP-MS, SEM-CL, infrared
52   microscopy, fluid geochemistry, metallogenic mechanism.
53

Introduction

55   Vein-type tungsten deposits, mostly referring to wolframite-quartz veins, provide approximately 44 %
56   of the world's known economic tungsten resource next to scheelite-skarn and contribute over 70 %
57   of the global tungsten production (Werner et al., 2014). Wolframite-quartz veins consist of
58   wolframite and quartz as the chief ore and gangue minerals, respectively, although variable amount
59   of other W/Sn oxides and a variety of sulfides may also occur up to economic grade. Genetically,
60   these veins and the commonly associated greisen-type mineralization are products of hydrothermal
61   systems connected with shallow-seated (ca. 1.5 ~ 5 km) and highly fractionated granitic intrusions
62   (Shcherba, 1970; Cerny et al., 2005).
63   The hydrothermal processes controlling wolframite precipitation in wolframite-quartz veins have
64   been debated for many decades. Early studies revealing fluid nature forming these veins were based
65   mainly on fluid inclusion in quartz, and to a lesser extent in other coexisting transparent minerals
66   such as cassiterite, scheelite, fluorite and topaz (e.g., Kelly and Rye, 1979; Zaw and Thet, 1983;
67   Shepherd and Waters, 1984; Higgins, 1980, 1985; Guiliani et al., 1988; Lynch, 1989). In 1984,
68   infrared microscopy was first applied to visualize internal textures of opaque minerals and thus
69   enabled microthermometry measurement of wolframite-hosted fluid inclusion (Campbell et al.,
70   1984). Since then, comparative studies have been carried out on fluid inclusion in coexisting
71   wolframite and quartz (e.g., Campbell and Robinson-Cook, 1987; Campbell and Panter, 1990;
72   Lüders, 1996; Rios et al., 2003; Wei et al., 2012; Ni et al., 2015; Li et al., 2018; Chen et al., 2018;
73   Korges et al., 2018; Legros et al., 2018). Among these works, a consensus is developing that most
74   wolframite was precipitated from fluids displaying diverse temperature and/or salinity compared to
75   the coexisting quartz, so that the two intergrown minerals are usually not cogenetic. Accordingly, it
76   has been concluded that only wolframite-hosted fluid inclusions provide the true properties of ore-
77   forming fluid, whereas quartz-hosted fluid inclusions are unrepresentative (Campbell and Panter,
78   1990; Lüders, 1996; Wei et al., 2012; Ni et al., 2015; Li et al., 2018 and Chen et al., 2018).
79   However, the complexity of hydrothermal processes forming coexisting ore and gangue minerals
80   has been increasingly recognized either based on elaborated petrography of free-grown crystal
81   samples (e.g., Audétat et al., 1998, 2000) or via the application of scanning electron microscope-
82   cathodoluminescence (SEM-CL) imaging on quartz (e.g., Boiron et al., 1992; Van den Kerkhof and
83   Hein, 2001; Rusk and Reed, 2002; Lambrecht and Diamond, 2014; Frelinger et al., 2015). A number
84   of detailed fluid inclusion studies have demonstrated that millimeter-scale porphyry-type quartz
85   veins can be products of multi-stage hydrothermal fluids featured by distinct physical and chemical
86   properties, so that discrimination of the detailed fluid history is critical for revealing the
87   metallogenic mechanism (Rusk and Reed, 2002; Landtwing et al., 2005; Klemm et al., 2007, 2008;
88   Pudack et al., 2009; Stefanova et al., 2014 and Ni et al., 2017). Likewise, one may find it hard to

89   imagine that quartz in larger scale wolframite-quartz veins (up to tens of centimeter thick) was

90   precipitated from a rather monotonous fluid. Nevertheless, most previous fluid inclusion studies on

91   coexisting wolframite and quartz from vein-type tungsten (± tin) deposits lack detailed petrography

92   based on CL-revealed quartz textures (e.g., Campbell and Robinson-Cook, 1987; Campbell and

93   Panter, 1990; Lüders, 1996; Wei et al., 2012; Ni et al., 2015; Li et al., 2018; Chen et al., 2018;

94   Korges et al., 2018; Legros et al., 2018). Consequently, the complexity of hydrothermal history in

95   wolframite-quartz veins is still poorly documented, and the affinity between fluid inclusions hosted

96   by quartz and the intergrown wolframite remains elusive.

97   From the late 1990s, laser ablation-inductively coupled plasma-mass spectrometry (LA-ICP-MS)

98   analysis of single fluid inclusion serves as one of the most powerful analytical techniques allowing

99   quantitative determination of most major and trace elements with their detection limit lower to ppm

100   level (Günther et al., 1998; Heinrich et al., 2003; Pettke et al., 2012). Previous quantitative fluid

101   inclusion studies on vein-type tungsten deposits are particularly scarce, and only limited data from

102   fluid inclusions in cassiterite and few gangue minerals have been reported (Heinrich et al., 1999;

103   Audétat et al., 2000; Hulsbosch et al., 2016; Lecumberri-Sanchez et al., 2017; Legros et al., 2018).

104   Recently, Korges et al. (2018) reported chemical compositions of both wolframite- and quartz-

105   hosted fluid inclusions from Sn-W quartz veins in the Zinnwald district. However, since the

106   measured fluid inclusions are not from intergrown wolframite and quartz, and the paragenetic

107   relationships between the fluid inclusion types are unclear, attempts to compare the chemical

108   process of fluids forming coexisting wolframite and quartz are not applicable.

109   In this contribution, a carefully selected sample comprising free-grown wolframite and quartz

110   crystals from the giant Yaogangxian W deposit in South China is dissected using a combined in situ

111   microanalytical protocol including SEM-CL imaging, infrared microthermometry, Raman

112   microspectroscopy and single fluid inclusion LA-ICP-MS analysis. This paper aims to compare and

113   better understand the detailed fluid processes forming coexisting wolframite and quartz via an

114   elaborated petrography and quantitative analysis of fluid inclusion in both minerals. The

115   complexities of hydrothermal history recorded in wolframite-quartz veins are demonstrated with

116   special emphasis on mineral paragenesis and fluid inclusion entrapment sequence. Possible

117   misinterpretation on fluid inclusion microthermometric and elemental composition data in previous

118   studies are evaluated based on our results. This study also reports the first LA-ICP-MS analysis of

119   wolframite-hosted fluid inclusions from vein-type tungsten deposit in China, and it is complemented

120   by a preliminary discussion on wolframite deposition mechanism in light of fluid geochemistry.

121

122   **Geological Settings**

123   China is the world's largest tungsten producer and hosts over 60 % of the world's known tungsten

124   resources (USGS, 2017). The majority of China's tungsten resources and production are contributed

125   by the world's famous Nanling region in South China (Fig. 1, Hsu, 1943; RGNTD, 1985; Liu and

126   Ma, 1993; Mao et al., 2007; Chen et al., 2008, 2013; Hu and Zhou, 2012; Ni et al., 2015). The

127   Nanling region covers the joint area of ca. 2×10^5 km^2 among the Jiangxi, Hunan, Guangdong and

128   Guangxi Provinces (Shu, 2007). It is characterized by pervasively developed granitoids that are

129   genetically related to the W-Sn mineralization (Hua et al., 2005; Chen et al., 2008, 2013). Except

130   for few scheelite-skarn such as the giant Shizhuyuan W-Sn-Mo-Bi deposit (Lu et al., 2003), tungsten

131   deposits in the Nanling region are predominately attributed to wolframite-quartz vein type (Fig. 1;

132   Lu et al., 1986), among which Yaogangxian is the largest (Peng et al., 2006; Hu et al., 2012; Li et

133 al., 2018). Tremendous previous geochemistry and geochronology studies have demonstrated that
134 most of these deposits were formed in response to the emplacement of the Upper Jurassic granitoids
135 during a limited time interval between ca. 165 and 150 Ma (Mao et al., 2007; Chen et al, 2013; Zhao
136 et al., 2018; Yuan et al., 2018).

137 The Yaogangxian W deposit is located in the Chenzhou Prefecture of Hunan Province (Fig. 1). The
138 deposit was initially explored in 1908, and it has being mined since 1914 with total WO_3 production
139 of over 60,000 tons to date (Hunan Yaogangxian Mining Co. Ltd., 2013). The total proven WO_3
140 reserve at Yaogangxian reaches approximately 500,000 tons (Zhu et al., 2015), which comprises
141 two distinct types of W mineralization, i.e. wolframite-quartz vein (~ 200,000 tons) and scheelite-
142 skarn (~ 300,000 tons, Hsu, 1957; Zhu et al., 2015). Although scheelite has larger reserves,
143 wolframite is mined predominately by far. The surface lithology of Yaogangxian is mainly featured
144 by the Jurassic Yaogangxian composite granitic pluton (170 to 157 Ma, Dong et al., 2014) which
145 intrudes the surrounding Paleozoic sedimentary strata (Fig. 2). The Yaogangxian composite granitic
146 pluton is further divided into three phases, namely, coarse-grained biotite granite (ca. 170 Ma),
147 medium- to fine-grained biotite granite (ca. 163 Ma) and fine-grained muscovite granite (ca. 155
148 Ma, Dong et al., 2014). The two later phases are temporally associated with both types of W
149 mineralization (ca. 155 ~ 163 Ma, Peng et al., 2006; Mao et al., 2007; Li et al., 2011).

150 Over 200 NW- to NNW-striking, steeply dipping wolframite-quartz veins occur in the north and
151 east contact zones between the granitic pluton and the surrounding sandstone (Fig. 2). These veins
152 have variable thickness ranging from 0.01 to 22.3 m averaging at 0.5 to 1.5 m, and they display
153 vertical extension mainly between 500 and 1,400 m (Hunan Yaogangxian Mining Co. Ltd., 2013).
154 The massive scheelite-skarn orebody, measuring 2,000 m along strike by 1,433 m down dip and
155 averaging 21.7 m in thickness, occurs in the west contact zone between the granitic pluton and the
156 Devonian limestone (Fig. 2, Hunan Yaogangxian Mining Co. Ltd., 2013). Previous geology and
157 geochronology studies suggest both types of W mineralization are cogenetic products of the same
158 magmatic-hydrothermal system controlled by different host sediments (Hsu, 1957; Li et al., 2011).
159 See Hsu (1957), Lin et al. (1987), Zhu et al. (2015) and Li et al. (2018) for more details on the
160 deposit geology of Yaogangxian.

161

162   **Mineral Cavities & Sampling**
163 In addition to its significant role in tungsten production, the Yaogangxian deposit is one of the
164 world's renowned mineral specimen producers (Ottens and Cook, 2005; Cook, 2005). At
165 Yaogangxian, over 60 mineral species have been recognized from open cavities in the wolframite-
166 quartz veins, where wolframite, bournonite and fluorite are well-known for developing into
167 spectacularly brilliant crystals. Chen (1995) provides a systemic description of mineral cavities at
168 Yaogangxian by summarizing the morphological features of 482 cavities from 22 major wolframite-
169 quartz veins. According to Chen (1995), open cavities are found mostly in wolframite-quartz veins
170 occurring from 700 to 1,500 m ASL (above sea level), and they are best developed between 700 and
171 1,150 m ASL, showing heterogeneous distribution among different veins. Over 90 % of cavities
172 have volumes less than 0.34 m^3, whereas large cavities with volume over 0.85 m^3 are invariably
173 found between 700 and 1,150 m ASL. However, due to intensive mining activities in the past decade
174 with extra profits from selling specimen, outcropped cavities are nearly extinct below 1,200 m ASL.
175 As a result, the examined free-grown crystal samples in this study are collected from veins above
176 1200 m ASL or given by local miners.

177   Six cavity samples containing euhedral wolframite and quartz crystals (Fig. 3) are obtained from
178   wolframite-quartz veins at Yaogangxian. These crystals provide the best opportunity for fluid
179   inclusion study because they usually contain large, well-preserved fluid inclusions and allow
180   reconstruction of a clear chronological entrapment sequence (e.g., Audétat et al., 1998, 2000; Müller
181   et al., 2001). However, because the cavities have more or less suffered from explosion during mining,
182   all examined samples exhibit a certain degree of damage, and each only tells part of the cavities'
183   mineralogy and paragenesis. Except for wolframite and quartz, euhedral crystals of muscovite,
184   arsenopyrite, pyrite, chalcopyrite, scheelite, calcite and fluorite selectively occur in different
185   samples. Even though mineral assemblages of each sample can vary significantly from one another,
186   a highly consistent paragenetic sequence is recognized according to the contact relationships
187   between minerals. To be specific, quartz usually grows on the tip of coexisting wolframite crystals
188   (e.g., Fig. 3a-b), whereas sulfides, calcite, fluorite and scheelite, if occur, commonly precipitate on
189   the crystal surfaces of quartz or wolframite. Such relationships agree well with many previous
190   studies (e.g., Campbell and Panter, 1990; Lüders, 1996; Wei et al., 2012; Ni et al., 2015; Li et al.,
191   2018; Chen et al., 2018) by roughly suggesting wolframite deposition at an earlier stage than
192   coexisting quartz, which in turn is earlier than other minerals.

193   However, detailed observation indicate a rather complicate story. Here, a suitable-sized sample
194   (*crystal 1-2*, Fig. 3c-h) containing relatively intact coexisting wolframite and quartz crystals is
195   selected for detailed dissection of mineral paragenesis and fluid history. As shown in Figure 3c-g,
196   the studied sample mainly comprises a long tabular wolframite crystal and an intergrown prismatic
197   quartz. Additional coexisting minerals include muscovite, arsenopyrite, chamosite and fluorite.
198   Magnified photos show small quartz crystals grow on top of muscovite (Fig. 3f), as well as small
199   wolframite grains trapped within the prismatic quartz (Fig. 3h). Due to crowded muscovite growth
200   at the contact site, paragenetic relationship between the main wolframite and quartz crystals is
201   difficult to tell. Nevertheless, a small branch of the main wolframite crystal is rooted into the main
202   quartz crystal (Fig. 3e), indicating at least part of the quartz postdates the main wolframite. Special
203   emphasis is given to the directional precipitation of arsenopyrite and chamosite on the 'back' side
204   of the sample (Fig. 3d). Careful observation also shows entrapment of small wolframite (and
205   muscovite) grains within the 'back' side of the main quartz crystal (Fig. 3h). Given their
206   precipitation planes are parallel to each other, these observations collectively suggest a series of
207   gravity-derived deposition of arsenopyrite, chamosite, wolframite and muscovite during vein
208   formation. In other words, the paleo gravity should be perpendicular to the precipitation plane or
209   'back' side, which was originally the upward face. Notably, although both arsenopyrite and
210   chamosite show gravity-derived features, the arsenopyrite only selectively occurs on muscovite and
211   wolframite, whereas the chamosite grains are scattered all over the exposed upward face. This
212   phenomenon implies the initial nucleation of arsenopyrite occurred after wolframite and muscovite
213   crystallization but prior to the prismatic quartz. The solo fluorite crystal also occurs on the upward
214   face of the wolframite crystal, but it does not necessarily indicate gravity-derived deposition (Fig.
215   3f).

216   To better clarify the mineral paragenetic sequence and accordingly reconstruct the entrapment
217   history of fluid inclusions, two doubly polished thin sections (300 μm in thickness) were made from
218   the prismatic quartz crystal in the direction parallel to c axis and perpendicular to the precipitation
219   plane. One doubly polished thin section (200 μm in thickness) of the main wolframite crystal was
220   cut parallel to the (010) face to improve the chances of finding primary fluid inclusions (e.g., Bailly

221 et al., 2002). These sections were mapped in detail using infrared and conventional microscopies,
222 and then studied via the analytical procedures described below.
223
224 **Analytical Methods**
225 **SEM-CL**
226 The scanning electron microscope-cathodoluminescence (SEM-CL) imaging was performed on two
227 quartz crystal sections to distinguish different quartz generations and their paragenetic contexts that
228 are usually not visible in hand sample or under transmitted light microscopy. The thin sections were
229 ultrasonically cleaned and then carbon-coated before analysis. In total, 142 CL images were
230 obtained using a Tescan MIRA3 LM instrument equipped with a CL detector at Nanjing
231 Hongchuang Geological Exploration Technology Service Co. The applied acceleration voltage and
232 current were set at consistent values of 15 kV and 1.2 nA, respectively. Each CL image was collected
233 by 60 s accumulation and shared about 15 % overlapping area with the surrounding images to insure
234 seamless stitching of panorama.
235
236 **Infrared microthermometry**
237 Fluid inclusion microthermometry was carried out using a Linkam THMSG600 Heating-Freezing
238 stage mounted on an Olympus BX51 microscope at the State Key Laboratory for Mineral Deposits
239 Research, Nanjing University. The microscopy is equipped with an infrared camera and filter to
240 allow infrared observation and microthermometry on wolframite-hosted fluid inclusions (Ni et al.,
241 2015; Li et al., 2018). Determination of synthetic fluid inclusion standards using both infrared and
242 normal transmitted light yielded identical phase transition temperatures within analytical precision,
243 so that temperature shift (Moritz, 2006) induced by infrared light is negligible. Quartz-hosted fluid
244 inclusions were measured using conventional approach in transmitted light. The Linkam Heating-
245 Freezing stage has a temperature range of -195 to $+600°C$. The stage was calibrated by measuring
246 the melting points of pure water ($0 °C$), pure CO_2 ($-56.6 °C$) in synthetic fluid inclusions and
247 potassium bichromate ($398 °C$). The measurement accuracy of phase transition temperatures in fluid
248 inclusions is $\pm 0.1 °C$ during cooling and about $\pm 2 °C$ between 100 and 600 °C. Although nearly
249 all measured fluid inclusion in this study may contain a certain amount of CO_2 ($\pm CH_4$), the melting
250 temperature of clathrate, if occurs, is particularly difficult to determine since no liquid CO_2 can be
251 observed during heating. In this case, the clathrate melting temperature is not a monotonic function
252 of salinity (Collins, 1979; Darling, 1991). Assuming that the CO_2 content is relatively minor,
253 salinities of fluid inclusions are calculated using the final ice melting temperatures (Bodnar, 1993).
254 Possible overestimation of salinity by ignoring the minor CO_2 is discussed in detail below. Notably,
255 homogenization temperatures of all quartz-hosted fluid inclusions were measured prior to the
256 destructive LA-ICP-MS analysis. However, for wolframite chips containing large but flat fluid
257 inclusions, homogenization temperature were obtained from smaller inclusions in the same fluid
258 inclusion assemblage (FIA, Goldstein and Reynolds, 1994) after LA-ICP-MS analysis to minimize
259 the risk of decrepitation during heating.
260
261 **Raman microspectroscopy**
262 Gas and liquid compositions of single quartz-hosted fluid inclusion at room temperature were
263 analyzed with a Renishaw RM2000 Raman microprobe using an Ar-ion laser with a surface power

264 of 5 mW for exciting the radiation (514.5 nm). The area of the charge-coupled device (CCD)

265 detector is 20 μm^2, and the scanning range for spectra was set between 500 and 4000 cm^{-1}.

266 Calibration of Raman spectrum using monocrystalline silicon and neon lamp standards was done

267 prior to analysis. An accumulation time of 60 s for each scan with spectral resolution of ± 2 cm^{-1}

268 was applied and a Lecia objective lens of 50x/0.75 (magnification/numerical aperture) is used for

269 fluid inclusion analysis. The grating is 1800 lines/mm and the slit size is set to 50 μm. For fluid

270 inclusions with small bubbles, independent gas composition analysis is difficult due to relatively

271 large detection area.

272

Fluid inclusion LA-ICP-MS analysis

274 More than 200 individual fluid inclusions hosted in the coexisting wolframite and quartz crystals

275 were measured by LA-ICP-MS to obtain their major and trace element compositions. The

276 measurement was performed using a Coherent GeolasHD system equipped with a 193 nm excimer

277 laser coupled to a Perkin Elmer 350x quadrupole ICP mass spectrometer at the single inclusion LA-

278 ICP-MS lab in Nanjing University.

279 To precisely locate the wolframite-hosted fluid inclusions under the non-infrared optical camera

280 in the laser ablation system, careful fluid inclusion mapping using infrared microscopy is critical

281 prior to analysis. Additional scratches were initially added to the fine polished surface as references.

282 Then, a transmitted light image of the fluid inclusion (Fig. S1a) was taken together with a reflected

283 light image of the surface using the infrared microscopy to locate the fluid inclusion projection on

284 the reflected light image (Fig. S1b). The reflected image with fluid inclusion position marked was

285 then used to relocate the fluid inclusion during LA-ICP-MS analysis (Fig. S1c). Similar positioning

286 procedure for LA-ICP-MS analysis of fluid inclusion in opaque minerals was previously applied in

287 pyrite and enargite from high-sulfidation epithermal deposit (Kouzmanov et al., 2010).

288 Table S1 summaries the instrumental conditions and data acquisition parameters used for LA-ICP-

289 MS analysis of both quartz- and wolframite-hosted fluid inclusions. For quartz-hosted fluid

290 inclusions, a stepwise increase of beam size was applied to avoid quartz decrepitation (Günther et

291 al., 1998), whereas a fixed beam size was used for wolframite-hosted fluid inclusions. The final

292 crater size is ideally slightly larger than the target fluid inclusion to ensure complete ablation.

293 However, this criterion was not applied on few large but elongated fluid inclusions (e.g., 100×20

294 μm) in wolframite to avoid intensive surface contamination derived from the condensation-

295 deposition effect of massive host ablation. Compared with quartz, the energy density on wolframite

296 was reduced to 5 J/cm^2 to avoid excessively high ^{182}W intensity (over 10^9 cps) of the host signal,

297 while the pulse frequency was set higher ($10 \sim 15$ Hz) because of the slow ablation rate. The quartz

298 and wolframite samples were loaded and analyzed along with two external standards in a rhomb-

299 shaped plexiglass cell and a round silica glass cell, respectively. Both cells are covered by an anti-

300 reflection coated glass window and have relatively small internal volume (ca. $1 \sim 3$ cm^3) which

301 enables fast washout of aerosol in 3 s. All wolframite samples were analyzed in the silica glass cell

302 that is specially designed to withstand cleaning by aqua regia (Schlöglova et al., 2017). Prior to

303 injection into the plasma, the He-based aerosol was admixed with nebulizer gas via a T-junction

304 immediately after ablation cells and then flow through a smoothing device to optimize signals. The

305 ICP-MS was tuned to achieve maximum sensitivity and low oxide production rate by lower the

306 ThO/Th ratios to < 0.5 % before analysis. The fluid inclusions in quartz and wolframite were

307 analyzed for different isotope listed in Table S1. The dwell time of elements that are detectable but

308 have low concentration or high background (e.g., S, Cl, Br) were increased to improve their counting

309 statistics, whereas dwell time of those major host elements were shortened to minimize the readings

310 per replicate.

311 Generally, measurement of each fluid inclusion consists of 20 ~ 30 s instrumental background

312 followed by 50 ~ 100 s ablation depending on the depth of fluid inclusion. Wolframite tends to have

313 slower ablation rate than quartz (ca. 1 µm/s), thus taking longer time to reach the fluid inclusion at

314 a given depth. All measured fluid inclusions in this study are within a depth range of 10 to 60 µm

315 as suggested by Pettke (2008). Fluid inclusions at greater depth are not measured to avoid increasing

316 down-hole fractionation effect (Guillong and Pettke, 2012). For most fluid inclusions, a pre-ablation

317 procedure was applied to eliminate surface contamination derived from previously ablated materials.

318 Maximum amount of 25 fluid inclusions are analyzed in each run bracketed by measurement of

319 external standards. The standard reference material NIST 610 and an in-house scapolite Sca-17 (Seo

320 et al., 2011) from ETH Zurich are used as external standards. The Sca-17 has relatively higher

321 concentrations of S, Cl and Br than NIST 610, and it is thus used to better quantify the S, Cl and Br

322 contents (Guillong et al., 2008a; Seo et al., 2011), whereas NIST 610 is used for all other elements.

323 LA-ICP-MS data reduction is performed using the SILLS software (Guillong et al., 2008b). Internal

324 standards used for host composition quantification are 100% SiO_2 for quartz and 100% total oxide

325 ($FeO / (FeO + Fe_2O_3) = 1$) for wolframite. For fluid inclusions, apparent NaCl equivalent salinities

326 obtained from microthermometry are used in combination with empirical mass or charge balance

327 algorithms (Heinrich et al., 2003; Allan et al., 2005) to calculate the Na concentration and

328 accordingly convert all other element/Na ratios into absolute concentrations. Major cations such as

329 Na and K are included into the salt correction. However, B is inapplicable to the empirical mass or

330 charge balance algorithms due to its dominant occurrence as oxyacid in aqueous solution, and

331 therefore it is not included in the salt correction despite its relatively high concentration in fluid

332 inclusion. This will introduce a certain degree of overestimation for all element concentrations

333 (discussed below, Sirbescu et al., 2013). In this study, salinity of each individual fluid inclusion were

334 determined prior to LA-ICP-MS analysis. For host (i.e. matrix) correction, a major host element

335 with overwhelmingly higher concentrations than in fluid inclusion is used as a matrix-only tracer to

336 remove host contribution from the mixed signal. Here, Si and W are selected as matrix-only tracers

337 for fluid inclusion signal correction in quartz and wolframite, respectively. All element

338 concentrations are reported as weight percent (wt. %) or ppm by weight (µg/g). The reliability of

339 the reported values are double-checked according to their signal peaks, i.e., only element signals

340 displaying clearly synchronous peak with Na are considered valid. The detection limits for all

341 measured elements are calculated using the 3σ standard deviation of the background intensities

342 (Heinrich et al., 2003; Pettke et al., 2012). Average elemental concentrations with uncertainties of ±

343 1σ standard deviation are calculated using all obtained values in each FIA.

344

345 **Mineral & Fluid Inclusion Petrography**

346 Transmitted light (Fig. 4a) and SEM-CL (Fig. 4b) panoramas of the thin section made from the

347 coexisting wolframite and quartz crystals show complex mineralogical textures and fluid history.

348 Interpretation of these complexities are elaborated below in four major aspects, namely, (1) multi-

349 stage quartz generations; (2) gravity-derived precipitation; (3) mineral paragenesis; and (4) fluid

350 inclusion entrapment. Stepwise magnified petrographic details of the thin section are illustrated in

351 Figure 5, 6 and 7.

352

Multi-stage quartz generations

353
354 According to the CL features and crosscutting relationships (Fig. 4), four major quartz generations
355 i.e., Q1 to Q4 can be identified in the prismatic quartz crystal. Q1 occupies over 90 % of the central
356 area, and it is generally characterized by CL-gray color with uniform growth bands following the
357 crystallographic forms of the quartz crystal. Slightly darker sectoral zones at both edges and
358 intrasectoral zones (e.g., Onasch and Vennemann, 1995) indicated by the tapered wedges also
359 belong to Q1. Two successive thin overgrowth zones extended from both upward and downward
360 sides of Q1 are defined as Q3 and Q4, respectively. Q3 is featured by heterogeneous luminosity with
361 irregular oscillatory growth bands, whereas Q4 shows homogeneous CL-dark color as the outmost
362 shell (Fig. 5e & g). Notably, a continuous transition of Q1, Q3 and Q4 is observed at the tip of the
363 prismatic quartz crystal, where Q4 exhibits both CL-dark and bright colors owing to different sectors
364 (right of Fig. 4b). In the upward part of the quartz crystal, physical boundaries of Q1/Q3 and Q3/Q4
365 are meanwhile outlined by two gravity-derived mineral precipitation zones that are visible under
366 transmitted and cross-polarized light (Fig. 5c-d). In contrast, these boundaries are invisible in the
367 downward part unless told from the CL image (Fig. 5f-g).

368 In addition to the continuous overgrowth, the quartz crystal has obviously undergone repeated
369 hydraulic fracturing and sealing. However, owing to similar CL features, discrimination of quartz
370 generations in healed cracks is only achieved according to the crosscutting relationships between
371 cracks and quartz overgrowth zones. Based on this criterion, quartz in the two major cracks and
372 their subordinate fissures that are strictly truncated by the Q1/Q3 boundary is classified as Q2 (Fig.
373 4b-c, 5e & g). In fact, Q2 may comprise at least two sub-generations (e.g., Fig. 5g) but they are not
374 further differentiated here. Similarly, healed cracks that are truncated by the Q3/Q4 boundary are
375 classified as $Q3_{Ps}$ (Fig. 5g, 7b), whereas healed cracks terminated within Q4 are classified as $Q4_{Ps}$
376 (Fig. 6b, 7b).

377

Gravity-derived precipitation

378
379 Several near parallel planes outlined by find-grained minerals in the upward part of the main quartz
380 crystal are attributed to gravity-derived mineral precipitation zones (i.e. GD zone; Fig. 5c-d). The
381 GD zone-1 which defines the Q1/Q3 boundary consists merely of crystalline muscovite and quartz
382 (Fig. 5c, 6c), whereas the GD zone-2 which defines the Q3/Q4 boundary contains wolframite in
383 addition to muscovite and quartz (Fig. 5c, 6c). This observation indicates that a wolframite
384 mineralization event (wf3) had occurred between crystallization of Q3 and Q4. Several GD
385 subzones consisting of only muscovite and quartz also occur within Q3 and Q4 (Fig. 5d, 6c). The
386 chamosite grains outlines the outermost GD zone as observed in hand specimen (Fig. 3g-h). The
387 occurrence of gravity-derived precipitation texture implies occasional static fluid environments in
388 the hydrothermal processes.

389

Mineral paragenesis

390
391 Paragenetic sequence of minerals in the studied sample is further constrained from their contact
392 relationships in thin sections. According to Figure 4, the coarse-grained muscovite occurring along
393 euhedral wolframite crystals is considered to form after wolframite. Similarly, all quartz generations
394 are inferred postdating the main wolframite and coarse-grained muscovite by enveloping their
395 euhedral crystals. This hypothesis also explains the facts that gravity-derived arsenopyrite

396 precipitation only occurs within the coarse-grained muscovite, and that it is absent in all quartz
397 generations. Moreover, in both thin sections, blade-shaped wolframite crystals are observed
398 occurring strictly along an early growth band of Q1 (Fig. 5a-b). This suggests another wolframite
399 precipitation event (wf2) during Q1 crystallization. Nevertheless, these wolframite blades are not
400 likely gravity-derived precipitates because they occur on both sides of the band.

401 Figure 8 summarizes a detailed crystal-scale mineral paragenesis described above. Generally, the
402 studied sample is consistent with other cavity samples by showing the main wolframite crystal
403 predates the intergrown quartz (e.g., Fig. 3a-b). However, the repeated formations of quartz,
404 wolframite and muscovite demonstrate the complexities of the hydrothermal processes.

405

406 **Fluid inclusion entrapment**

407 In the studied sample, two-phase aqueous inclusions constitute the solo fluid inclusion type in both
408 wolframite and quartz at room temperature. Nearly all fluid inclusions show relatively consistent
409 vapor proportions between 20 and 30 vol %. Rarely, small mica-like mineral occurs in quartz-hosted
410 fluid inclusions, and it is interpreted as accidentally trapped solid phase due to its occasional
411 occurrence. Post-entrapment modifications such as necking-down, stretching or decrepitation (e.g.,
412 Bodnar, 2003) are absent. Most quartz-hosted inclusions exposed at surface are surrounded by CL-
413 dark patches, which indicates refining of their host quartz during ripening process (Lambrecht and
414 Diamond, 2014). However, fluid inclusion migration (Audétat and Günther, 1999; Lambrecht and
415 Diamond, 2014) is not evident in the studied quartz crystal. The characteristics of all studied fluid
416 inclusions are described below in terms of their host minerals and entrapment sequence.

417 **Wolframite**: Primary fluid inclusions in the earlier formed main wolframite crystal represent the
418 initial fluid record in the studied sample. Characterizing the fluid inclusion genesis in wolframite is
419 greatly facilitated by the oriented sections, i.e., cutting parallel to the (010) face, where flat or
420 elongated primary fluid inclusions lying along growth planes can be easily identified (Pw, Fig. S1a).
421 Most primary fluid inclusions exhibit sizes between 10 and 40 μm in length, with exceptions of
422 some very large inclusions sized up to 100 μm (e.g., Fig. 10). In contrast, fluid inclusion trails
423 crosscutting the growth planes are attributed to secondary or pseudosecondary in origin (Roedder,
424 1984; Goldstein and Reynolds, 1994). Because these fluid inclusions are usually smaller in size
425 (mostly < 10 μm) and obscure under infrared microscopy, they are not studied in the current work.

426 **Quartz**: The prismatic quartz crystal contains abundant fluid inclusions that generally show
427 random distribution mainly in Q1. The CL imaging helps greatly in reconstructing their entrapment
428 sequence by providing unambiguous growth textures and truncation relationships. Fluid inclusions
429 occurring strictly along quartz growth zones are classified as primary in origin, whereas inclusions
430 trails trapped within healed cracks truncated by later quartz growth zones are classified as
431 pseudosecondary in origin. Essentially, pseudosecondary fluid inclusions are primarily trapped fluid
432 that healed the crack, so that the inclusions are expected to form synchronously with the quartz
433 generation in cracks.

434 According to the criteria mentioned above, four successively trapped fluid inclusion generations
435 are recognized in the prismatic quartz crystal. The first fluid generation refers to pseudosecondary
436 fluid inclusions confined within Q1 and Q2 (Ps1-2, Fig. 6c, 7d). Because no primary fluid inclusion
437 is identified in Q1 or Q2, the Ps1-2 inclusions actually represent a combination of fluids trapped
438 between complete crystallization of Q1 and initiation of Q3. Ps1-2 inclusions usually have negative
439 crystal shape and large sizes mainly from 20 to 100 μm in length. The second fluid generation refers

440   to pseudosecondary trails terminated at the Q3/Q4 boundary (Ps3, Fig. 7c-d). Similarly, Ps3
441   inclusions record the specific fluid occurring between complete crystallization of Q3 and initiation
442   of Q4. Importantly, this timing is contemporaneous with the gravity-derived wolframite
443   precipitation in GD zone-2 (Fig. 5c-d), suggesting a strong affinity between Ps3 fluid and wolframite
444   mineralization. In contrast to Ps1-2 type, Ps3 inclusions have much smaller population, irregular
445   shape, and they typically have size between 5 and 30 μm. The third and fourth fluid generations
446   refer to primary inclusions occurring along Q4 growth zone (P4) and pseudosecondary trails
447   terminated at GD subzone within Q4 (Ps4, Fig. 6c, 7c), respectively. Both P4 and Ps4 inclusions
448   record the fluids from which Q4 precipitated, and they are very small in size (mostly < 5 μm).
449   Interestingly, no secondary fluid inclusion (i.e., postdating all quartz generations) is identified in
450   quartz.

451   Summarized entrapment sequence of fluid inclusion assemblages and their correspondence to
452   mineral paragenesis are illustrated in Figure 8. Note that Pw and Ps3 inclusions demonstrably
453   provide the direct records of ore-forming fluids that are responsible for two wolframite precipitation
454   events, i.e. wf1 and wf3, respectively.

455

456   **Fluid Geochemistry**
457   **Microthermometric results**
458   Homogenization temperatures and salinities measured from 212 fluid inclusions in seventy FIAs
459   are summarized in Table 1 and plotted in Figure 9a. The number of studied FIAs for each fluid
460   generation varies greatly according to their relative abundances. Microthermometric data for each
461   FIA of Pw, Ps1-2 and Ps3 types are listed in Table 2 with individual fluid inclusion data available
462   in Table S2. Note that few FIAs are petrographically defined nice assemblages but only have one
463   measurable fluid inclusion because of the size.

464   **Wolframite-hosted FIAs**: Twenty-eight fluid inclusions from twelve Pw FIAs yield
465   homogenization temperatures between 263 and 305 °C, and all except one homogenize between 263
466   and 288 °C (Fig. 9a). Salinities of Pw FIAs range from 4.5 to 7.2 wt. % NaCl equiv. based on ice
467   melting temperatures. During cooling of few large and flat Pw inclusions, an additional liquid phase
468   is condensed (Fig. 10a), and it indicates the presence of CO_2 in the vapor bubble. This hypothesis is
469   confirmed by the melting of solid CO_2 phase around −58 °C during heating (Fig. 10b-c, see caption
470   for details). In addition, the slight depression on the triple point of CO_2 (ideally at −56.6 °C) implies
471   the presence of other gases (Seitz et al., 1987). Upon heating to a temperature range from 0 to 10 °C,
472   the occurrence of clathrate in these fluid inclusions can be easily recognized from bubble
473   deformation. However, the liquid CO_2 that occurs during cooling does not regenerate in the heating
474   run, suggesting the condensation of liquid CO_2 was in clathrate metastable field (Diamond, 1992).
475   For most Pw inclusions that are smaller or not flat-shaped, liquid CO_2 phase is not observed during
476   cooling. This is because either they have less CO_2 that is insufficient to intersect the metastable
477   extension of the L_{aq}-L_{carb}-V curve (e.g., Diamond, 1992, 2001; Steele-MacInnis, 2018), or the poor
478   visibility to distinguish CO_2 liquid phase from smaller but darker bubbles. Although few Pw
479   inclusions show clathrate-derived bubble deformation above 0 °C during heating, the clathrate
480   melting temperatures exhibit bad reproducibility, and thus they are not determined. In contrast, most
481   Pw inclusions show no signs of clathrate formation above 0 °C, and they are inferred to contain only
482   minor CO_2, i.e., less than 1.5 mol% (relative to $H_2O + CO_2$; Diamond, 1992, 1994). In such scenario,
483   CO_2 contributes to the ice melting point depression as a dissolved component rather than forming

484   clathrate, and it can result in a maximum ice melting depression of about −1.5 °C at Q1 point

485   (Hedenquist and Henley, 1985). Accordingly, the calculated salinities for most Pw inclusions may

486   be overestimated by maximum amount of 30 % to 50 % based on ice melting temperatures.

487   **Quartz-hosted FIAs**: In general, microthermometry results are similar for all quartz-hosted fluid

488   inclusion assemblages (Table 1). Measurements on forty-four Ps1-2 FIAs yield relatively variable

489   homogenization temperatures from 233 to 297 °C, and consistent salinities from 5.9 to 6.6 wt. %

490   NaCl equiv. (Fig. 9a). Average homogenization temperatures of eleven Ps3 FIAs vary from 250 to

491   310 °C, with only one assemblage exceeding 300 °C (Fig. 9a). Obtained salinities of Ps3 FIAs are

492   slightly variable from 5.2 to 8.4 wt. % NaCl equiv., and they apparently show a positive correlation

493   with homogenization temperatures (Fig. 9b). Only a few microthermometric data are obtained from

494   the P4 and Ps4 FIAs owing to their small sizes and numbers. Three individual fluid inclusions in

495   the solo P4 assemblage give consistent homogenization temperatures at 268 °C and salinity of 5.9

496   wt. % NaCl equiv. Two Ps4 FIAs containing seven fluid inclusions yield average homogenization

497   temperatures of 274 and 280 °C, and salinities of 6.0 and 6.9 wt. % NaCl equiv., respectively.

498   Although no liquid CO_2 is observed during microthermometry, very few Ps1-2 inclusions are

499   inferred to contain CO_2 by showing signs of clathrate melting at temperature above 0 °C. Raman

500   analysis confirms that nearly all Ps1-2 and Ps3 inclusions contain a certain amount of $CO_2 \pm CH_4$,

501   so that their salinities are overestimated based on ice melting temperatures. Similar to the

502   wolframite-hosted fluid inclusions, a maximum CO_2-derived ice melting depression of about

503   −1.5 °C is expected for most quartz-hosted fluid inclusions that do not show clathrate formation.

504   This corresponds to salinity overestimation by ca. 25 % to 45 % in maximum.

505

506   **Raman characteristics**

507   Prior to the destructive LA-ICP-MS analysis, Raman analysis has been carried out on several

508   representative Ps1-2 and Ps3 inclusions to qualitatively identify their gas compositions and

509   polyatomic ions in aqueous solutions. Pw inclusions are not suitable for Raman analysis owing to

510   their host's opacity, whereas P4 and Ps4 inclusions are too small to obtain workable Raman signals.

511   Typical Raman spectra collected from Ps1-2 and Ps3 inclusions are illustrated in Figure 11.

512   Because Ps1-2 inclusions sometimes have huge size (up to 200 µm), their Raman spectra can display

513   excellent SNR (signal to noise ratio) which enables identification of very week vibrations that are

514   not recognizable in Ps3 inclusions. In addition to the dominated H_2O peak, dissolved H_3BO_3 (876

515   cm^{-1}, Schmidt et al., 2005) and CO_2 (1278 and 1385 cm^{-1}, Davis and Oliver, 1972) in aqueous

516   solution are identified in the liquid phase of Ps1-2 inclusions (Fig. 11a-b). The vapor phase of Ps1-

517   2 inclusions contain CO_2 (1284 and 1387 cm^{-1}, Rosso and Bodnar, 1995) and CH_4 (2920 and 3020

518   cm^{-1}, Brunsgaard-Hansen et al., 2002) as the dominant gas species, while minor H_2S (2611 cm^{-1},

519   Burke, 2001) and N_2 (2331 cm^{-1}, Herzberg, 1950) are also detected (Fig. 11c-e). The occurrences of

520   both boron and sulfur species are verified by subsequent LA-ICP-MS analysis with their

521   concentrations quantitatively determined. In contrast, CO_2 and CH_4 are the only detectable species

522   in addition to H_2O in Ps3 inclusions owing to poorer SNR (Fig. 11f). Both CO_2 and CH_4 peaks show

523   strong decrease in relative intensities compared to Ps1-2 inclusions, implying less CO_2 and CH_4 in

524   Ps3 fluid.

525

526   **Elemental compositions**

527   LA-ICP-MS microanalysis was carried out on 202 individual fluid inclusions from sixty-seven FIAs

528   of Pw, Ps1-2 and Ps3 types in both wolframite and quartz. Most FIAs contain 2 to 5 individual fluid

529   inclusions, although few FIAs only allow LA-ICP-MS analysis on one inclusion because others are

530   too small to yield workable signals. The average elemental concentrations and corresponding ratios

531   X/(Na+K) with 1σ standard deviation for most detectable elements determined are tabulated in

532   Table 2 and plotted in Figure 12, respectively. Complete dataset of all detectable elements for each

533   individual fluid inclusion is available in Table S2 in the supplementary materials. Note that absolute

534   elemental concentrations are calculated based on the applied internal standard, which in our case is

535   the Na concentration derived from apparent salinity. The presence of carbonic volatiles can affect

536   the apparent salinity and the relatively high B content will introduce errors in salt correction. Both

537   may significantly result in overestimations of absolute Na concentration that in turn affects all other

538   elements. However, the element ratios are independent of the applied internal standard (Günther et

539   al., 1998), and they are thus used for most plots and discussions below.

540   Figure S2 illustrates the time-resolved LA-ICP-MS signals of liquid-rich fluid inclusions in quartz

541   (Fig. S2a) and wolframite (Fig. S2b), respectively. Most elements occur synchronously with the

542   narrow Na peak, suggesting their presence in the aqueous solution (and vapor), whereas delayed

543   peaks are attributed to solid minerals as exemplified by the second Al peak in Figure S2a. As shown

544   in Table 2, all fluid inclusions contain NaCl and KCl as major dissolved salts. Regardless of the

545   internal standard issue, K, B, Li, As and Cs are mostly at concentrations of 100s to 1000s of ppm,

546   along with variable Rb, Cu, Sb and Sr concentrations from several to over 100 ppm. If detected, S

547   and Al yield concentrations of few 1000s and few 100s ppm, respectively. Notably, Al is nearly

548   absent in wolframite-hosted inclusions but is detectable in most quartz-hosted fluid inclusions, and

549   its concentrations are much more variable than other elements. Even though some unexpected high

550   Al values are subject to the small mica in these fluid inclusions, the measured Al concentrations are

551   too high given its poor solubility in NaCl-H$_2$O solution (e.g., Manning, 2006). The elevated Al

552   concentrations can be resulted from either fluid inclusion ripening process (Lambrecht and Diamond,

553   2014) which extracts additional Al from host quartz, or enhanced Al solubility in the presence of

554   fluorine (Yardley et al., 1993; Tagirov et al., 2002) or borate complex (Tagirov et al., 2004).

555   Nevertheless, our current data do not allow further identification on this point. W and Mn

556   concentrations are only determined from quartz-hosted fluid inclusions at 10 ppm level. Given the

557   three obtained Fe values and the minimum detection limit of Fe in most other fluid inclusions, Fe

558   concentrations in Ps1-2 and Ps3 inclusions are generally less than few 10s of ppm. Ca concentrations

559   are merely obtained from two Ps3 FIAs and yield values around 200 to 400 ppm.

560   Evolution and comparison of fluid chemistry among three different fluid stages are illustrated in

561   Figure 12 and 13, respectively. In general, element ratios X/(Na+K) for alkali metals such as Li, Na,

562   K, Cs and Rb remain largely uniform (i.e., within one order of magnitude) among the three fluid

563   stages irrespective of salinity and paragenetic sequence (Fig. 12). Compared with Pw inclusions,

564   Ps1-2 and Ps3 inclusions show slightly lower Li and K contents, which are best explained by

565   precipitation of Li-rich muscovite between entrapment of Pw and Ps1-2 fluids (Fig. 8b). The

566   covariant depletion of K and Rb in some Ps1-2 FIAs probably implies that Ps1-2 inclusions actually

567   comprise more than one fluid stage, which agrees with our inference from petrographic observation.

568   Most strikingly, element ratios for B, As and Sr show strong variations between different fluid stages.

569   Compared with Pw and Ps3 inclusions, B and As are distinctly enriched in Ps1-2 inclusions, whereas

570   Sr is significantly depleted (Fig. 12, Fig. 13a-b). On the other hand, although Pw and Ps3 inclusions

571   are both temporally and spatially separated, the chemical characteristics of the two fluid stages are

572   remarkably consistent (Fig. 13c), particularly in terms of B, As and Sr (Fig. 13d). Using the
573   minimum detection limit as the highest estimation, Cu and to a lesser extent S are likely enriched in
574   Ps1-2 inclusions relative to Ps3, similar to the preference of B and As. However, this hypothesis
575   does not apply to Pw inclusions because of the higher detection limits for Cu and S. In addition,
576   despite a coeval wolframite precipitation event had occurred at Ps3 stage, the Mn/(Na+K) and
577   W/(Na+K) ratios are generally consistent in both Ps1-2 and Ps3 fluid inclusions (Fig. 12), and they
578   do not present obvious correlations with homogenization temperatures (Fig. 14).

579

580   **Discussion**

581

582   **Fluid processes in coexisting wolframite and quartz**
583   Based on detailed petrography and quartz CL imagining, at least four successive quartz generations,
584   three independent wolframite mineralization events and five stages of muscovite precipitation are
585   identified in a single sample (Fig. 8). The degree of repetition of many minerals in the depositional
586   sequence produces a paragenesis unusually complex among otherwise comparable studies on
587   coexisting wolframite and quartz (e.g., Campbell and Robinson-Cook, 1987; Campbell and Panter,
588   1990; Lüders, 1996; Rios et al., 2003; Wei et al., 2012; Ni et al., 2015; Li et al., 2018; Chen et al.,
589   2018; Legros et al., 2018). In these studies, coexisting wolframite and quartz are regarded as either
590   cogenetic or not, whereas detailed paragenesis in the crystal scale is usually ignored. To better
591   reconstruct the hidden paragenesis in wolframite-quartz veins, CL imagining on quartz can be
592   indispensable (e.g., Rusk and Reed, 2002; Landtwing et al., 2005; Klemm et al., 2007, 2008; Pudack
593   et al., 2009; Stefanova et al., 2014 and Ni et al., 2017). It is particularly important to use CL when
594   the studied samples do not exhibit straightforward textures as those from free-grown euhedral
595   crystals (e.g., Audétat et al., 1998, 2000). Even in our case where the gravity-derived mineral zones
596   serve as natural boundaries, the complete quartz paragenesis would remain obscure without CL
597   revealed textures. Besides, the elaborated petrography provides new insights on some specific fluid
598   processes that have occurred during vein formation. For example, the repeated hydrofracturing and
599   sealing of the studied quartz crystal likely reflect pressure fluctuation and turbulence of the fluid
600   system. The gravity-derived precipitation of muscovite, wolframite, arsenopyrite and chamosite, on
601   the other hand, implies occasional static fluid environment during vein formation. These findings
602   demonstrably indicate the complexity of fluid processes that may be critical for better understanding
603   the hydrothermal metallogenic system.
604   The detailed paragenesis allows establishment of a clear entrapment sequence of fluid inclusion in
605   the crystal scale. In the studied sample, at least four episodic fluid pulses are recognized and two of
606   them, i.e., Pw and Ps3 are intimately concurrent with wolframite deposition (Fig. 8). This finding
607   demonstrates the potential of trapping the true ore-forming fluid in both quartz and coexisting
608   wolframite rather than only in wolframite, as many previous studies suggested (e.g., Campbell and
609   Panter, 1990; Lüders, 1996; Wei et al., 2012; Ni et al., 2015; Li et al., 2018; Chen et al., 2018). As
610   shown in Figure 9, wolframite-hosted inclusions do not exhibit significantly higher homogenization
611   temperatures than those from coexisting quartz, although some quartz-hosted fluid inclusions do
612   have lower temperatures. Contrastingly, comparative studies on samples from other wolframite-
613   quartz veins in the Nanling region (Wei et al., 2012; Ni et al., 2015; Li et al., 2018; Chen et al., 2018;
614   Legros et al., 2018) invariably show that fluid inclusions in wolframite have higher homogenization
615   temperatures than those in coexisting quartz. Such relationship is commonly reinforced by the

616   earlier precipitation of wolframite than quartz (e.g., Li et al., 2018; Chen et al., 2018), but our results
617   suggest that there are exceptions. Note the homogenization temperatures discussed above should be
618   close to the true temperature because fluid boiling is suggested to have occurred during the
619   crystallization of both wolframite and quartz (discussed in details below). In such scenario, pressure
620   correction on the trapping temperature is less significant and thus is ignored. Owing to the presence
621   of carbonic volatiles, the apparent salinity of our fluid inclusions can be overestimated by up to
622   50 %. In spite of this, some fluid evolution trends are inferred from the microthermometry results
623   (Fig. 9). For Ps1-2 inclusions, temperature fluctuation (both heating and cooling) is obvious, and it
624   is probably coeval with quartz hydraulic fracturing and sealing. For Ps3 inclusions, the positive
625   correlation between salinity and temperature is best interpreted by low-pressure boiling of a CO_2-
626   bearing low salinity fluid, where variable degree of CO_2 (and heat) loss to the vapor phase can
627   increase the ice melting temperature of the residual liquid and result in extended salinity variation
628   (Wilkinson, 2001). Raman results also show significant depletion of CO_2 and CH_4 in Ps3 inclusion
629   relative to Ps1-2 (Fig. 11), suggesting fluid degassing had occurred. Although no boiling assemblage
630   is observed, the hypothesis agrees with many previous studies on wolframite-quartz veins that fluid
631   boiling or unmixing is commonly seen in quartz (e.g., Kelly and Rye, 1979; Higgins, 1985; Lüders,
632   1996; Wei et al., 2012; Ni et al., 2015; Li et al., 2018; Chen et al., 2018).
633   LA-ICP-MS analysis shows that fluids precipitating coexisting wolframite and quartz display
634   distinct chemical signatures despite sharing similar overall ranges of salinity and homogenization
635   temperature. Most strikingly, chemistries of Pw and Ps3 fluids coeval with wolframite deposition
636   are remarkably similar, but both show strong enrichment in Sr and depletion in B and As relative to
637   the Ps1-2 fluid. Given the above discussed fluid evolution, the selective depletion of B and As in
638   Ps3 fluids could be straightforwardly explained as a result of fluid boiling, because B and As are
639   both confirmed to preferentially partitioning into the vapor phase during fluid boiling (Heinrich et
640   al., 1999; Audétat et al., 2000; Williams-Jones and Heinrich, 2005; Landtwing et al., 2010). To better
641   examine this hypothesis, the relative ratios of B, As and two other elements Sb and S, which are
642   also supposed to partition in favor of the vapor phase (Heinrich et al., 1999; Williams-Jones and
643   Heinrich, 2005), are plotted against Na (Fig. 15). Considering the true sulfur concentrations in Ps3
644   inclusions are lower than the detection limit, all elements except Sb show concurrent fractionation
645   between Ps1-2 and Ps3. The trend is possibly indicative of fluid boiling at lower pressure, in which
646   condition the salinity of the residual liquid does not change significantly (Heinrich, 2007). On the
647   other hand, the consistent Sb ratios do not necessarily contradict fluid boiling because in some cases
648   Sb can remain in the liquid phase, such as the boiling assemblages in Sn-W veins from Mole Granite
649   (Audétat et al., 2000). Since Pw inclusions display strong chemical affinities with Ps3 inclusions
650   and both are coeval with wolframite mineralization, it is reasonable to infer that Pw fluid had also
651   undergone boiling before entrapment, and the ore-forming fluids characterized by special chemical
652   signatures were injected episodically into the conduit veins. Nevertheless, the lack of constraint on
653   fluid prior to Pw does not allow further discussion in the current study. Possible interpretation for
654   the enrichment of Sr in Pw and Ps3 inclusions is the mixing with sedimentary fluids that are usually
655   enriched in Sr (Kharaka and Hanor, 2014), similar to the fluid evolution revealed in Carlin-type gold
656   deposit (Large et al., 2016). Such hypothesis is plausible at Yaogangxian given the majority of
657   wolframite-quartz veins are hosted in sandstones and slate (Hunan Yaogangxian Mining Co. Ltd.,
658   2013).
659   In summary, the studied intergrown wolframite and quartz crystals were precipitated from fluids

660   exhibiting similar temperature and salinity but diverse chemistry. The fluids responsible for
661   wolframite deposition are episodic and may have undergone fluid boiling and mixing to generate
662   the distinct chemical features from those precipitating quartz.

663

664   **Misinterpretation of fluid inclusion data**
665   It should be noteworthy that the accuracy of fluid inclusion data from microthermometry and LA-
666   ICP-MS analysis can be significantly affected by the occurrence of carbonic volatiles and boric acid,
667   which have been largely neglected among previous comparable study. In principle, the addition of
668   carbonic volatiles and boric acid in fluid inclusions can both lead to miscalculation of element
669   concentrations via two different ways. For microthermometry, the presence of CO_2 ($\pm$ CH_4) up to
670   ca. 10 mol % in low salinity aqueous fluid inclusion does not allow salinity estimation at Q2 point
671   using clathrate melting temperature (Steele-MacInnis, 2018), so that significant overestimation by
672   as much as 50 % on apparent salinity calculated from ice melting temperature can be achieved
673   (Collins, 1979; Hedenquist and Henley, 1985). For LA-ICP-MS analysis, whether included in the
674   salt correction or not, the relatively high boron content in fluid inclusion can yield large error in
675   internal standardization of Na from apparent salinity (Sirbescu et al., 2013) which leads to
676   miscalculation of all element concentrations. To be specific, including B into salt correction as BCl_3
677   can result in underestimation of absolute concentration, whereas excluding B from salt correction
678   can do the opposite (Sirbescu et al., 2013). A preliminary text on our LA-ICP-MS data obtained
679   from Ps1-2 inclusions shows maximum four times higher concentration for excluding than including
680   B into salt correction (e.g., 8000 ppm vs. 2000 ppm for B). Assuming the true B concentration lies
681   in the middle between the endmember values, all elemental concentrations reported for Ps1-2
682   inclusions can be overestimated by over 50 % depending on the B to Na ratios. Combined with the
683   CO_2-derived error on apparent salinity, the occurrence of both carbonic volatiles and boric acid can
684   collectively lead to overestimation by as much as 75 % for all element concentrations, although the
685   elemental ratios are unaffected.

686   Accordingly, misinterpretation of fluid inclusion data in many previous fluid inclusion studies on
687   vein-type tungsten deposit can be significant. In particular, case studies worldwide have
688   demonstrated the formation of wolframite-quartz veins by low salinity (generally < 10 wt. % NaCl
689   eq.) CO_2-bearing fluids, while CO_2-rich fluid inclusion showing liquid CO_2 phase at room
690   temperature is not scarce (e.g., Kelly and Rye, 1979; Higgins, 1980, 1985; Ramboz et al., 1985;
691   Guiliani et al., 1988; Campbell and Panter, 1990; Lüder, 1996; Wei et al., 2012; Rios et al., 2003;
692   Ni et al., 2015; Chen et al., 2018; Li et al., 2018; Legros et al., 2018). Thus, possible salinity
693   overestimation may be derived from those fluid inclusions that contain substantial amount of CO_2
694   ($\pm$ CH_4) but do not generate liquid carbonic phase during cooling, in which condition the salinity is
695   conventionally calculated using ice melting temperature by assuming CO_2 content is minor. This
696   scenario may also help to explain why CO_2-rich fluid inclusions commonly display lower salinity
697   than coexisting CO_2-bearing inclusions in some wolframite-quartz veins (e.g., Chen et al., 2018;
698   Legros et al., 2018).

699   In addition to carbonic volatiles, the presence of boron may introduce even greater error on the
700   LA-ICP-MS elemental concentrations of fluid inclusion from vein-type tungsten ($\pm$ tin) deposits.
701   As an incompatible element during magma crystallization, B is generally enriched in evolved
702   magma and the associated hydrothermal systems (e.g., Pollard et al., 1987; Peretyazhko et al., 2000;
703   Thomas et al., 2003). Recent fluid inclusion studies from W-Sn deposits in the Panasqueira

704   (Lecumberri-Sanchez et al., 2017) and the Erzgebirge districts (Thomas et al., 2003; Korges et al.,
705   2018) illustrate elevated B contents in ore-forming fluids derived from highly fractionated granites.
706   Accordingly, the high B content in Ps1-2 fluid inclusions from Yaogangxian is not surprising, and
707   it is presumably the same case for other granite-related quartz-vein type tungsten deposits in the
708   Nanling region. Notably, Legros et al. (2018) reports fluid inclusion LA-ICP-MS data obtained from
709   the Piaotang and Maoping W (-Sn) deposits in the Nanling region. Nevertheless, since B is not
710   measured in their study, the reported elemental concentrations might be biased to a certain degree.

711

Source of ore-forming fluid

713   Multiple criteria based on element concentrations and ratios measured by LA-ICP-MS analysis are
714   used to trace the fluid source at Yaogangxian (Fig. 16). Given the relatively high contents of CO_2
715   and reducing volatiles such as CH_4 and H_2S, fluids derived from the host sediments are possibly
716   involved in the formation of wolframite-quartz veins in addition to magmatic fluids (Rios et al.,
717   2003; Burnard and Polya, 2004). To illustrate this assumption, fluid inclusion data are plotted in the
718   Rb/Na vs. K/ Na and Mn vs. Na diagrams (Fig. 16a-b) with characteristic areas of magmatic-
719   hydrothermal fluids and basinal brines acquired from Samson et al. (2008) and Williams-Jones et
720   al. (2010). The Rb/Na vs. K/ Na diagram shows clear magmatic source for most fluid inclusions in
721   both wolframite and quartz, except for few Ps1-2 inclusions exhibiting slightly lower K/Na ratios
722   likely due to massive precipitation of muscovite (Fig. 8). Because Mn cannot be determined in
723   wolframite-hosted inclusions, only data from quartz-hosted fluid inclusions are plotted in the Mn
724   vs. Na diagram. Contrastingly, these fluid inclusions show stronger affinity to basinal brines rather
725   than magmatic fluids, even though the dilution effect from overestimation of absolute
726   concentrations or meteoric water mixing is considered (Fig. 16b). Seemingly, the low Mn/Na ratio
727   implies a sedimentary source for Mn, which is a major component in the studied wolframite.
728   Nevertheless, an alternative explanation is preferred that the low Mn/Na ratios in quartz-hosted fluid
729   inclusions are resulted from previous wolframite precipitation, which consumed most Mn from the
730   initial magmatic fluid. If this is true, the hypothesized Mn concentrations in initial Pw fluid
731   precipitating the major wolframite crystals should be one to two orders of magnitude higher than
732   Ps1-2 and Ps3 fluids.
733   Considering the non-reactive heavy alkalis i.e., Cs and Rb as largely conservative fluid components
734   during hydrothermal mineralization, the Cs/Rb ratios can be applied to identify the diversity of fluid
735   source (e.g., Klemm et al., 2008; Korges et al., 2018). Fluid inclusion Cs/Rb ratios from both
736   wolframite and quartz are mostly confined within a narrow range between 4 and 20 (Fig. 16c),
737   corresponding to a maximum 5-fold variation. Since the 100-fold variation in fluid inclusion Cs/Rb
738   ratios reported from the Zinnwald Sn-W deposit in Erzgebirge is interpreted to suggest a single fluid
739   source (Korges et al., 2018), our data should be confidently indicative of an identical magmatic fluid
740   source by integrating previous isotopic data (Li et al., 2018). In addition, given the degree of fluid
741   Cs enrichment is conventionally used to monitor the crystallization degree of the source magma in
742   evolved magmatic-hydrothermal systems (e.g., Audétat and Pettke, 2003; Audétat et al., 2008;
743   Klemm et al., 2008; Kouzmanov et al., 2010), the nearly constant Cs/(Na + K) ratio in all measured
744   FIAs (Fig. 12) reflects a negligible change in crystallization degree of the parental granitic magma
745   during the deposition of the studied wolframite and quartz crystals.
746   The fluid Br/Cl ratio serves as another excellent tracer for fluid source and origin because it is
747   largely conservative during fluid-rock interactions but particularly sensitive to fluid reservoirs

748   originating ultimately from seawater evaporation (Böhlke and Irwin, 1992; Yardley et al., 1993;
749   Irwin and Roedder, 1995; Nahnybida et al., 2009; Kendrick and Burnard, 2013; Lecumberri-
750   Sanchez and Bodnar, 2018). Figure 16d shows the fluid Br/Cl ratios obtained from this study and
751   their correlation to other W-Sn deposits worldwide as well as typical fluid reservoirs for a variety
752   of metallogenic environments. Eleven molar Br/Cl ratios obtained from quartz-hosted fluid
753   inclusions exhibit a narrow range between 0.30×10^{-3} and 0.98×10^{-3}, whereas the wolframite-
754   hosted fluid inclusion yields a sole higher value at 2.3×10^{-3}. The Br/Cl ratios in quartz-hosted fluid
755   inclusions are similar to those from the St. Austell Sn-W deposit in England (Irwin and Roedder,
756   1995) and the Mole Granite Sn-W deposit in Australia (Seo et al., 2011), and they are generally
757   overlapping with the summarized fluid reservoir for granite-related deposits (Lecumberri-Sanchez
758   and Bodnar, 2018). Due to the strong S-type affinity for granites related to W-Sn deposits (Cerny et
759   al., 2005), the relatively low Br/Cl ratios are well explained by assimilation of Br-poor evaporitic
760   sedimentary rocks during crustal anatexis (e.g., Campbell et al., 1995; Seo et al., 2011). However,
761   the Panasqueira W-Sn deposit provides an exception by displaying significantly elevated fluid Br/Cl
762   ratios despite the S-type parental granite, and it is explained as a result of mixing with organic-rich
763   sedimentary fluid (Polya et al., 2000). This interpretation may equally explain the high Br/Cl ratio
764   obtained from wolframite-hosted fluid inclusion at Yaogangxian, but it is not conclusive based on
765   the sole datum.
766   In summary, our results favor the dominance of a single-sourced magmatic-hydrothermal fluid in
767   the formation of the studied coexisting wolframite and quartz, although additions of sedimentary
768   fluids and meteoric water are also likely.
769

770   **Wolframite deposition mechanism: an open question**
771   Along with recent applications of infrared microthermometry and LA-ICP-MS analysis on fluid
772   inclusion from vein-type tungsten (± tin) deposits, four major wolframite deposition mechanisms
773   have been proposed and debated, namely: (1) fluid cooling (Ni et al., 2015; Li et al., 2018; Chen et
774   al., 2018); (2) addition of Fe during fluid-rock interaction (Lecumberri-Sanchez et al., 2017); (3)
775   fluid boiling or unmixing (Lüders, 1996; Korges et al., 2018); and (4) mixing of magmatic fluid
776   with meteoric water (Wei et al., 2012; Legros et al., 2018). Here, we provide a preliminary
777   discussion on wolframite deposition mechanism based on our limited fluid inclusion data obtained
778   from the studied sample.
779   Given intense solubility decrease of wolframite from 350 to 300 °C in modeled magmatic-
780   hydrothermal fluid (Jaireth et al., 1990), fluid cooling may be one of the most effective mechanisms
781   for wolframite deposition (Heinrich, 1990). According to the statistical evolution trend reflected by
782   microthermometry data of wolframite-hosted fluid inclusions, previous studies on a number of vein-
783   type tungsten deposits in the Nanling region, including Yaogangxian, suggest fluid simple cooling
784   as a major wolframite deposition mechanism (Ni et al., 2015; Chen et al., 2018; Li et al., 2018).
785   Generally, our microthermometric data from Pw inclusions do not support such scenario (Fig. 9)
786   but meanwhile not negate it because they are too limited to reflect any statistical significance.
787   However, our LA-ICP-MS results do show that W and Mn concentrations in Ps1-2 and Ps3
788   inclusions are invariant to temperature variation in the range from 220 to 320 °C (Fig. 14). This
789   finding indicates at least some wolframite deposition events (e.g., wf3 in Fig. 8) are not simply
790   derived by fluid cooling.
791   Because W is mainly transported in the form of tungstic acids such as H_2WO_4, HWO_4^-, WO_4^{2-}

792   and/or other alkali metal tungstate in aqueous hydrothermal fluids (Gibert et al., 1992; Wood and
793   Samson, 2000), the addition of cation precipitators such as Fe and Mn can be important driving
794   factor for wolframite deposition. A recent fluid inclusion LA-ICP-MS study by Lecumberri-Sanchez
795   et al. (2017) reports significantly low Fe concentrations in quartz-hosted fluid inclusions from the
796   Panasqueira W-Sn deposit and shows the addition of Fe released from fluid-rock interaction with
797   host sediments controls the wolframite deposition. Our fluid inclusion data are comparable to theirs
798   by showing most Fe contents lower than the detection limit (Table S2). Nevertheless, the relatively
799   high detection limit for Fe, generally at 10s to few 100s ppm in both our study and Lecumberri-
800   Sanchez et al. (2017), does not necessarily indicate insufficient Fe to precipitate wolframite from
801   the initial fluids, especially considering the W concentrations that are also less than few 10s of ppm.
802   On the other hand, Mn is detectable in over half of the fluid inclusions, and the mole ratios of Mn/W
803   in fluid inclusions ($\sim$ 2 to 76, calculated from Table S2) are significantly higher than the coexisting
804   wolframite ($\sim$ 0.6, our unpublished data). Consequently, the addition of Fe or Mn from other source
805   cannot be concluded as a major wolframite deposition mechanism at Yaogangxian.
806   Korges et al. (2018) carried out another comparable fluid inclusion study on the Zinnwald Sn-W
807   deposit using both infrared microthermometry and LA-ICP-MS analysis. Based on the fluid
808   chemistry and the occurrence of boiling assemblages, fluid boiling is proposed as the main
809   mechanism for wolframite and cassiterite mineralization. This scenario is supported by several
810   previous studies suggesting boiling or unmixing can result in pH increase by degassing acidic
811   volatiles (e.g., HCl, CO_2), which in turn facilitates wolframite deposition (Higgins, 1985; Lynch,
812   1989; Wood and Samson, 2000; Krylova et al., 2012). As discussed above, our fluid inclusion data
813   strongly imply the occurrence of fluid boiling or unmixing in Ps3 stage that is coeval with
814   wolframite deposition. Raman and LA-ICP-MS analysis also suggests possible pH increase by loss
815   of acidic species such as CO_2, H_2S and H_3BO_3 in Ps3 stage. Thus, fluid boiling or unmixing is likely
816   the main driving mechanism for the late stage wolframite deposition (i.e., wf3). Given the similar
817   fluid chemical features in both Pw and Ps3 inclusions, fluid boiling might be equally involved in
818   the precipitation of the main wolframite crystal. However, this hypothesis cannot be confirmed in
819   our current study due to lack of further constraint. It is also noteworthy that hypersaline brine
820   inclusions are commonly observed in Sn dominated deposits but typically absent in W dominated
821   deposits (Wood and Samson, 2000), as exemplified by the Zinnwald Sn-W deposit (Korges et al.,
822   2018) and the Yaogangxian W deposit (Li et al., 2018 and this study). This phenomenon implies the
823   fluid unmixing at Yaogangxian occurred in relatively lower pressure and temperature conditions
824   than those in Sn dominated deposits.
825   A recent fluid inclusion LA-ICP-MS study on wolframite-quartz veins from the Maoping and
826   Piaotang deposits suggests multiple-sourced fluids are involved in the formation of W-Sn
827   mineralization (Legros et al., 2018). These two deposits are particularly comparable to Yaogangxian
828   because they are very close in distance (Fig. 1), and they share similar geology, geochronology and
829   mineralization characteristics (Ni et al., 2015; Chen et al., 2018). Based mainly on fluid inclusion
830   microthermometry and elemental composition data, Legros et al. (2018) recognizes four endmember
831   fluids in both Maoping and Piaotang, and interprets the dilution of magmatic fluids as the major
832   ore-forming mechanism. However, aside doubt on the small number of composition data collected
833   without using fluid inclusion assemblage, the reported salinities may be biased since the effect of
834   additional CO_2 is not considered. Therefore, the proposed fluid mixing mechanism at Maoping and
835   Piaotang should be treated with more caution. In contrast, our fluid inclusion data from sixty-seven

836 fluid inclusion assemblages demonstrably indicate the ore-forming fluids are derived mainly from
837 a stable magmatic source during the period when the studied wolframite and quartz crystalized.
838 Dilution of this magmatic fluid via mixing with meteoric water cannot be excluded according to the
839 microthermometric results, since both dilution and the presence of variable amount of CO_2 can result
840 in the apparent salinity variation of Pw and Ps3 inclusions (Fig. 9b-c). Nevertheless, dilution alone
841 cannot generate the significant chemical changes in Pw and Ps3 inclusions so that its association
842 with wolframite deposition is not suggested in the studied case. In addition, the elevated Sr contents
843 in both Pw and Ps3 inclusions imply the involvement of Sr-rich fluids likely derived from host
844 sediments (Kharaka and Hanor, 2014; Large et al., 2016). This hypothesis is partly supported by a
845 recent He-Ar isotope study, which proposes the ore-forming fluids at Yaogangxian are mixture of
846 crustal and magmatic fluids containing mantle components (Hu et al., 2012).
847 From the perspective of fluid chemistry in the studied sample, deposition of wolframite likely
848 depends on the specific fluid processes that meanwhile control the variations of carbonic volatiles,
849 B, As, S, Sr, and possibly Ca (presumably enriched in Ps3 inclusions) in the fluid. The depletion of
850 these elements is unlikely to be derived by mineral crystallization because precipitation of the
851 related minerals that can selectively extract some of these elements from fluid are either not coeval
852 with the specific fluid stage or absent in the wolframite-quartz veins. Collectively, we suggest that
853 fluid phase separation and mixing with sedimentary fluid may play important roles in controlling
854 the chemical variation of fluid and the concurrent wolframite deposition. Nevertheless, owing to the
855 limitation of our available data, the major wolframite deposition mechanism at Yaogangxian as well
856 as other analogous vein-type tungsten deposits in the Nanling region remains an open question to
857 solve.
858
859 **Implications**
860 The following implications can be made based on the observation and data presented:
861 1. Detailed petrographic observation and CL imaging on the studied coexisting wolframite and
862 quartz show repeated precipitation of quartz, wolframite and muscovite, suggesting the fluid
863 processes forming these two minerals can be much more complex than previously proposed.
864 Reconstruction of fluid history based on the crystal-scale paragenesis demonstrates that both quartz-
865 and wolframite-hosted fluid inclusions are capable of reflecting the true wolframite deposition
866 condition.
867 2. Microthermometry results show some fluctuation of homogenization temperature and salinity of
868 fluids trapped in coexisting wolframite and quartz. The measured wolframite-hosted fluid inclusions
869 do not display significantly higher homogenization temperature than those from coexisting quartz,
870 which provides an exception to the consensus reached from previous comparative studies in the
871 same region.
872 3. Distinct chemical features of quartz- and wolframite-hosted fluid inclusions are revealed by LA-
873 ICP-MS analysis. Fluid inclusions trapped concurrently with wolframite deposition are enriched in
874 Sr but depleted in B, As and possibly S, compared with fluid inclusions that are not associated with
875 wolframite deposition. The chemical similarity between the two wolframite-associated but spatially
876 and temporally separated fluid inclusion generations implies episodic injection of ore-forming fluids
877 characterized by similar chemical signatures.
878 4. Both wolframite- and quartz-hosted fluid inclusions are proved to contain certain amounts of CO_2
879 $\pm CH_4$, whereas H_3BO_3 in quartz-hosted fluid inclusions can occur as major solute second only to

880   NaCl. Ignoring the presence of both carbonic volatiles and high B contents in fluid inclusions may

881   lead to miscalculation and misinterpretation of fluid inclusion data. These effects should be

882   considered critically for fluid inclusion study on granite-related tungsten-tin deposits.

883   5. Multiple chemical criteria suggest the fluids that formed the studied wolframite and quartz

884   crystals are derived predominately from an identical magmatic source with possible additions of

885   sedimentary fluids and meteoric water.

886   6. Fluid phase separation and mixing with sedimentary fluid may have played important roles in

887   controlling the fluid chemical changes that are concurrent with wolframite deposition. Fluid cooling

888   or addition of Fe and Mn from other source does not appear to be the major driving factor in the

889   studied case. However, further investigation is necessary to better clarify the wolframite deposition

890   mechanism at Yaogangxian.

891

907

908   **Supplementary Materials**

909   Detailed instrumental and data acquisition parameters of fluid inclusion LA-ICP-MS analytical

910   system are summarized in Table S1. Elemental composition data for all measured fluid inclusions

911   are listed in Table S2. Ablation procedure of wolframite-hosted fluid inclusions is shown in Figure

912   S1, whereas characteristic LA-ICP-MS transient signals of fluid inclusions in quartz and wolframite

913   are shown in Figure S2. Supplementary data associated with this article can be found in the online

914   version.

915

916   **Reference**

917   Allan, M. M., Yardley, B. W., Forbes, L. J., Shmulovich, K. I., Banks, D. A., & Shepherd, T. J. (2005).

918   Validation of LA-ICP-MS fluid inclusion analysis with synthetic fluid inclusions. *American*

919   *Mineralogist*, *90*(11-12), 1767-1775.

920   Audétat, A., Günther, D., & Heinrich, C. A. (1998). Formation of a magmatic-hydrothermal ore deposit:

921   Insights with LA-ICP-MS analysis of fluid inclusions. *Science*, *279*(5359), 2091-2094.

922   Audétat, A., & Günther, D. (1999). Mobility and H_2O loss from fluid inclusions in natural quartz

923   crystals. *Contributions to Mineralogy and Petrology*, 137(1-2), 1-14.

924 Audétat, A., Günther, D., & Heinrich, C. A. (2000). Causes for large-scale metal zonation around
925   mineralized plutons: Fluid inclusion LA-ICP-MS evidence from the Mole Granite,
926   Australia. *Economic Geology*, *95*(8), 1563-1581.

927 Audétat, A., & Pettke, T. (2003). The magmatic-hydrothermal evolution of two barren granites: A melt
928   and fluid inclusion study of the Rito del Medio and Canada Pinabete plutons in northern New
929   Mexico (USA). *Geochimica et Cosmochimica Acta*, *67*(1), 97-121.

930 Audetat, A., Pettke, T., Heinrich, C. A., & Bodnar, R. J. (2008). The composition of magmatic-
931   hydrothermal fluids in barren and mineralized intrusions. *Economic Geology, 103*(5), 877-908.

932 Bailly, L., Grancea, L., & Kouzmanov, K. (2002). Infrared microthermometry and chemistry of
933   wolframite from the Baia Sprie epithermal deposit, Romania. *Economic Geology*, *97*(2), 415-423.

934 Bodnar, R. J. (1993). Revised equation and table for determining the freezing point depression of H2O-
935   NaCl solutions. *Geochimica et Cosmochimica Acta*, *57*(3), 683-684.

936 Bodnar, R. J. (2003). Reequilibration of fluid inclusions. In I. Samson, A. Anderson, & D. Marshall, eds.
937   Fluid Inclusions: Analysis and Interpretation. Mineral. Assoc. Canada, Short Course 32, 213-230.

938 Böhlke, J. K., & Irwin, J. J. (1992). Laser microprobe analyses of Cl, Br, I, and K in fluid inclusions:
939   Implications for sources of salinity in some ancient hydrothermal fluids. *Geochimica et*
940   *Cosmochimica Acta*, *56*(1), 203-225.

941 Boiron, M. C., Essarraj, S., Sellier, E., Cathelineau, M., Lespinasse, M., & Poty, B. (1992). Identification
942   of fluid inclusions in relation to their host microstructural domains in quartz by
943   cathodoluminescence. *Geochimica et Cosmochimica Acta*, *56*(1), 175-185.

944 Brunsgaard Hansen, S., Berg, R. W., & Stenby, E. H. (2002). How to determine the pressure of a
945   methane‐containing gas mixture by means of two weak Raman bands, v3 and 2v2. Journal of
946   Raman Spectroscopy, 33(3), 160-164.

947 Burke, E. A. (2001). Raman microspectrometry of fluid inclusions. *Lithos*, *55*(1-4), 139-158.

948 Burnard, P. G., & Polya, D. A. (2004). Importance of mantle derived fluids during granite associated
949   hydrothermal circulation: He and Ar isotopes of ore minerals from Panasqueira1. *Geochimica et*
950   *Cosmochimica Acta*, *68*(7), 1607-1615.

951 Campbell, A. R., Hackbarth, C. J., Plumlee, G. S., & Petersen, U. (1984). Internal features of ore minerals
952   seen with the infrared microscope. *Economic Geology*, *79*(6), 1387-1392.

953 Campbell, A. R., & Robinson-Cook, S. (1987). Infrared fluid inclusion microthermometry on coexisting
954   wolframite and quartz. *Economic Geology*, *82*(6), 1640-1645.

955 Campbell, A. R., & Panter, K. S. (1990). Comparison of fluid inclusions in coexisting (cogenetic?)
956   wolframite, cassiterite, and quartz from St. Michael's Mount and Cligga Head, Cornwall,
957   England. *Geochimica et Cosmochimica Acta*, *54*(3), 673-681.

958 Campbell, A. R., Banks, D. A., Phillips, R. S., & Yardley, B. W. (1995). Geochemistry of Th-U-REE
959   mineralizing magmatic fluids, Capitan mountains, New Mexico. *Economic Geology*,*90*(5), 1271-
960   1287.

961 Cerny, P., Blevin, P. L., Cuney, M., & London, D. (2005). Granite-related ore deposits. *Economic*
962   *Geology*, *100*, 337-370.

963 Chen, L. L., Ni, P., Li, W. S., Ding, J. Y., Pan, J. Y., Wang, G. G., & Yang, Y. L. (2018). The link between
964   fluid evolution and vertical zonation at the Maoping tungsten deposit, Southern Jiangxi, China:
965   Fluid inclusion and stable isotope evidence. *Journal of Geochemical Exploration*.

966 Chen, J., Lu, J. J., Chen, W. F., Wang, R. C., Ma, D. S., Zhu, J. C., ... & Ji, J. F. (2008). W-Sn-Nb-Ta-
967   bearing granites in the Nanling Range and their relationship to metallogengesis.*Geological Journal*

968   *of China Universities*, *14*(4), 459-473 (in Chinese with English abstract).

969   Chen, J., Wang, R., Zhu, J., Lu, J., & Ma, D. (2013). Multiple-aged granitoids and related tungsten-tin

970   mineralization in the Nanling Range, South China. *Science China Earth Sciences*,*56*(12), 2045-

971   2055.

972   Chen, Y. R. (1995). Geodes and the Significance of their Research in Yaogangxian Tungsten

973   Deposit. *HUNAN GEOLOGY*, *4* (in Chinese with English abstract).

974   Collins, P. L. (1979). Gas hydrates in CO_2-bearing fluid inclusions and the use of freezing data for

975   estimation of salinity. *Economic geology*, *74*(6), 1435-1444.

976   Cook, R. B. (2005). Connoisseur's Choice: Bournonite: Yaogangxian Mine, Chenzhou, Hunan Province,

977   China. *Rocks & Minerals*, *80*(1), 40-44.

978   Darling, R. S. (1991). An extended equation to calculate NaCl contents from final clathrate melting

979   temperatures in H_2O-CO_2-NaCl fluid inclusions: Implications for PT isochore location. *Geochimica*

980   *et Cosmochimica Acta*, *55*(12), 3869-3871.

981   Davis, A. R., & Oliver, B. G. (1972). A vibrational-spectroscopic study of the species present in the CO_2−

982   H_2O system. *Journal of Solution Chemistry*, *1*(4), 329-339.

983   Déruelle, B., Dreibus, G., & Jambon, A. (1992). Iodine abundances in oceanic basalts: implications for

984   Earth dynamics. *Earth and Planetary Science Letters*, *108*(4), 217-227.

985   Diamond, L. W. (1992). Stability of CO_2 clathrate hydrate+ CO_2 liquid+ CO_2 vapour+ aqueous KCl-

986   NaCl solutions: Experimental determination and application to salinity estimates of fluid

987   inclusions∗. *Geochimica et Cosmochimica Acta*, *56*(1), 273-280.

988   Diamond, L. W. (1994). Salinity of multivolatile fluid inclusions determined from clathrate hydrate

989   stability. *Geochimica et Cosmochimica Acta*, *58*(1), 19-41.

990   Diamond, L. W. (2001). Review of the systematics of CO2-H2O fluid inclusions. *Lithos*, *55*(1-4), 69-99.

991   Dong, S. H., Bi, X. W., Hu, R. Z., Chen, Y. W. (2014). Petrogenesis of the Yaogangxian granites and

992   implications for W mineralization, Hunan Province. *Acta Petrologica Sinica*, *30*(9), 2749-2765 (in

993   Chinese with English abstract).

994   Frelinger, S. N., Ledvina, M. D., Kyle, J. R., & Zhao, D. (2015). Scanning electron microscopy

995   cathodoluminescence of quartz: Principles, techniques and applications in ore geology. *Ore Geology*

996   *Reviews*, *65*, 840-852.

997   Gibert, F., Moine, B., Schott, J., & Dandurand, J. L. (1992). Modeling of the transport and deposition of

998   tungsten in the scheelite-bearing calc-silicate gneisses of the Montagne Noire,

999   France. *Contributions to Mineralogy and Petrology*,*112*(2-3), 371-384.

1000   Giuliani, G., Li, Y. D., Sheng, T. F. (1988). Fluid inclusion study of Xihuashan tungsten deposit in the

1001   southern Jiangxi Province, China. *Mineralium Deposita,* *23*(1), 24-33.

1002   Goldstein, R.H., Reynolds, T.J. (1994). Systematics of fluid inclusions in diagenetic minerals: SEPM

1003   short course. *Society for. Sediment. Geol. 31*, 1-199

1004   Günther, D., Audétat, A., Frischknecht, R., & Heinrich, C. A. (1998). Quantitative analysis of major,

1005   minor and trace elements in fluid inclusions using laser ablation–inductively coupled plasmamass

1006   spectrometry. *Journal of Analytical Atomic Spectrometry*, *13*(4), 263-270.

1007   Guillong, M., Latkoczy, C., Seo, J. H., Günther, D., & Heinrich, C. A. (2008a). Determination of sulfur

1008   in fluid inclusions by laser ablation ICP-MS. *Journal of Analytical Atomic Spectrometry*, *23*(12),

1009   1581-1589.

1010   Guillong, M., Meier, D. L., Allan, M. M., Heinrich, C. A., & Yardley, B. W. (2008b). Appendix A6:

1011   SILLS: A MATLAB-based program for the reduction of laser ablation ICP-MS data of

1012   homogeneous materials and inclusions. *Mineralogical Association of Canada Short Course*, *40*,
1013   328-333.

1014   Guillong, M., & Pettke, T. (2012). Depth dependent element ratios in fluid inclusion analysis by laser
1015   ablation ICP-MS. *Journal of analytical atomic spectrometry*, *27*(3), 505-508.

1016   Hedenquist, J. W., & Henley, R. W. (1985). The importance of CO 2 on freezing point measurements of
1017   fluid inclusions; evidence from active geothermal systems and implications for epithermal ore
1018   deposition. *Economic geology*, *80*(5), 1379-1406.

1019   Heinrich, C. A. (1990). The chemistry of hydrothermal tin (-tungsten) ore deposition. *Economic
1020   Geology*, *85*(3), 457-481.

1021   Heinrich, C. A., Gunther, D., Audétat, A., Ulrich, T., & Frischknecht, R. (1999). Metal fractionation
1022   between magmatic brine and vapor, determined by microanalysis of fluid inclusions. *Geology*, *27*(8),
1023   755-758.

1024   Heinrich, C. A., Pettke, T., Halter, W. E., Aigner-Torres, M., Audétat, A., Günther, D., & Horn, I. (2003).
1025   Quantitative multi-element analysis of minerals, fluid and melt inclusions by laser-ablation
1026   inductively-coupled-plasma mass-spectrometry. *Geochimica et Cosmochimica Acta*, *67*(18), 3473-
1027   3497.

1028   Heinrich, C. A. (2007). Fluid-fluid interactions in magmatic-hydrothermal ore formation. *Reviews in
1029   Mineralogy and Geochemistry*, *65*(1), 363-387.

1030   Herzberg, G. (1950). Molecular spectra and molecular structure. Vol. 1: Spectra of diatomic
1031   molecules. *New York: Van Nostrand Reinhold, 1950, 2nd ed.*

1032   Higgins, N. (1980). Fluid inclusion evidence for the transport of tungsten by carbonate complexes in
1033   hydrothermal solutions. *Canadian Journal of Earth Sciences*, *17*(7), 823-830.

1034   Higgins, N. (1985). Wolframite deposition in a hydrothermal vein system; the Grey River tungsten
1035   prospect, Newfoundland, Canada. *Economic Geology 80*(5): 1297-1327.

1036   Hsu, K. C. (1943). Tungsten deposits of southern Kiangsi, China. *Economic Geology*, *38*(6), 431-474.

1037   Hsu, K. C. (1957). Discovery of pyrometasometic scheelite deposits near a wolframite/producing district
1038   in southern China, and a discussion about the origin of these two classes of deposits. *Acta Geologica
1039   Sinica*, *37*(2), 117-151 (in Chinese with English abstract).

1040   Hu, R. Z., Bi, X. W., Jiang, G. H., Chen, H. W., Peng, J. T., Qi, Y. Q., ... & Wei, W. F. (2012). Mantle-
1041   derived noble gases in ore-forming fluids of the granite-related Yaogangxian tungsten deposit,
1042   Southeastern China. *Mineralium Deposita*,*47*(6), 623-632.

1043   Hu, R. Z., & Zhou, M. F. (2012). Multiple Mesozoic mineralization events in South China—an
1044   introduction to the thematic issue. *Mineralium Deposita*, *47*(6), 579-588.

1045   Hua, R. M., Chen, P. R., Zhang, W. L., Yao, J. M., Lin, J. F., Zhang, Z. S., & Gu, S. Y. (2005).
1046   Metallogeneses and their geodynamic settings related to Mesozoic granitoids in the Nanling
1047   Range. *Geological Journal of China Universities*, *3*, 291-304 (in Chinese with English abstract).

1048   Hulsbosch, N., Boiron, M. C., Dewaele, S., & Muchez, P. (2016). Fluid fractionation of tungsten during
1049   granite–pegmatite differentiation and the metal source of peribatholitic W quartz veins: Evidence
1050   from the Karagwe-Ankole Belt (Rwanda).*Geochimica et Cosmochimica Acta*, *175*, 299-318.

1051   Irwin, J. J., & Roedder, E. (1995). Diverse origins of fluid in magmatic inclusions at Bingham (Utah,
1052   USA), Butte (Montana, USA), St. Austell (Cornwall, UK), and Ascension Island (mid-Atlantic, UK),
1053   indicated by laser microprobe analysis of Cl, K, Br, I, Ba+ Te, U, Ar, Kr, and Xe. *Geochimica et
1054   cosmochimica acta*, *59*(2), 295-312.

1055   Jaireth, S., Heinrich, C. A., and Solomon, M. (1990). Chemical controls on the hydrothermal tungsten

1056   transport in some magmatic systems and the precipitation of ferberite and scheelite. *Geological*
1057   *Society of Australia Abstracts, 25*, 269–270.
1058   Jambon, A., Deruelle, B., Dreibus, G., & Pineau, F. (1995). Chlorine and bromine abundance in MORB:
1059   the contrasting behaviour of the Mid-Atlantic Ridge and East Pacific Rise and implications for
1060   chlorine geodynamic cycle. *Chemical Geology*, *126*(2), 101-117.
1061   Johnson, L. H., Burgess, R., Turner, G., Milledge, H. J., & Harris, J. W. (2000). Noble gas and halogen
1062   geochemistry of mantle fluids: comparison of African and Canadian diamonds.*Geochimica et*
1063   *Cosmochimica Acta*, *64*(4), 717-732.
1064   Kelly, W. C., & Rye, R. O. (1979). Geologic, fluid inclusion, and stable isotope studies of the tin-tungsten
1065   deposits of Panasqueira, Portugal. *Economic Geology*, *74*(8), 1721-1822.
1066   Kendrick, M. A., & Burnard, P. (2013). Noble gases and halogens in fluid inclusions: A journey through
1067   the Earth's crust. In *The noble gases as geochemical tracers* (pp. 319-369). Springer, Berlin,
1068   Heidelberg.
1069   Kharaka, Y. K., & Hanor, J. S. (2014). Deep fluids in sedimentary basins, in Holland, H., and Turekian,
1070   H.D.H.K., eds., *Treatise on geochemistry (second edition)*: Oxford, UK, Elsevier, p. 471–515,
1071   Klemm, L. M., Pettke, T., Heinrich, C. A., & Campos, E. (2007). Hydrothermal evolution of the El
1072   Teniente deposit, Chile: Porphyry Cu-Mo ore deposition from low-salinity magmatic
1073   fluids. *Economic Geology*, *102*(6), 1021-1045.
1074   Klemm, L. M., Pettke, T., & Heinrich, C. A. (2008). Fluid and source magma evolution of the Questa
1075   porphyry Mo deposit, New Mexico, USA. *Mineralium Deposita*, *43*(5), 533.
1076   Korges, M., Weis, P., Lüders, V., & Laurent, O. (2018). Depressurization and boiling of a single magmatic
1077   fluid as a mechanism for tin-tungsten deposit formation. *Geology*, *46*(1), 75-78.
1078   Kouzmanov, K., Pettke, T., & Heinrich, C. A. (2010). Direct analysis of ore-precipitating fluids:
1079   combined IR microscopy and LA-ICP-MS study of fluid inclusions in opaque ore
1080   minerals. *Economic Geology*, *105*(2), 351-373.
1081   Krylova, T. L., Pandian, M. S., Bortnikov, N. S., Gorelikova, N. V., Gonevchuk, V. G., & Korostelev, P.
1082   G. (2012). Degana (Rajasthan, India) and Tigrinoe (Primorye, Russia) tungsten and tin-tungsten
1083   deposits: Composition of mineral-forming fluids and conditions of wolframite deposition. *Geology*
1084   *of Ore Deposits*, *54*(4), 276-294.
1085   Lambrecht, G., & Diamond, L. W. (2014). Morphological ripening of fluid inclusions and coupled zone-
1086   refining in quartz crystals revealed by cathodoluminescence imaging: Implications for CL-
1087   petrography, fluid inclusion analysis and trace-element geothermometry. *Geochimica et*
1088   *Cosmochimica Acta*, *141*, 381-406.
1089   Landtwing, M. R., Pettke, T., Halter, W. E., Heinrich, C. A., Redmond, P. B., & Einaudi, M. T., et al.
1090   (2005). Copper deposition during quartz dissolution by cooling magmatic–hydrothermal fluids: the
1091   Bingham porphyry. *Earth & Planetary Science Letters, 235*(1–2), 229-243.
1092   Landtwing, M. R., Furrer, C., Redmond, P. B., Pettke, T., Guillong, M., & Heinrich, C. A. (2010). The
1093   Bingham Canyon porphyry Cu-Mo-Au deposit. III. Zoned copper-gold ore deposition by magmatic
1094   vapor expansion. *Economic Geology*,*105*(1), 91-118.
1095   Large, S. J., Bakker, E. Y., Weis, P., Wälle, M., Ressel, M., & Heinrich, C. A. (2016). Trace elements in
1096   fluid inclusions of sediment-hosted gold deposits indicate a magmatic-hydrothermal origin of the
1097   Carlin ore trend. *Geology*, *44*(12), 1015-1018.
1098   Lecumberri-Sanchez, P., Vieira, R., Heinrich, C. A., Pinto, F., & Wälle, M. (2017). Fluid-rock interaction
1099   is decisive for the formation of tungsten deposits. *Geology*, *45*(7), 579-582.

1100   Lecumberri-Sanchez, P., & Bodnar, R. J. (2018). Halogen geochemistry of ore deposits: contributions
1101   towards understanding sources and processes. In *The Role of Halogens in Terrestrial and*
1102   *Extraterrestrial Geochemical Processes* (pp. 261-305). Springer, Cham.

1103   Legros, H., Richard, A., Tarantola, A., Kouzmanov, K., Mercadier, J., Vennemann, T., ... & Bailly, L.
1104   (2018). Multiple fluids involved in granite-related W-Sn deposits from the world-class Jiangxi
1105   province (China). *Chemical Geology*. https://doi.org/10.1016/j.chemgeo.2018.11.021

1106   Li, S. T., Wang, J. B., Zhu, X. Y., & Li, C. (2011). Re-Os Dating of Molybdenite and Sulfur Isotope
1107   Analysis of the Yaogangxiang Tungsten Polymetallic Deposits in Hunan Province and Their
1108   Geological Significance. *Geoscience*,*25*(2), 228-235 (in Chinese with English abstract).

1109   Li, W. S., Ni, P., Pan, J. Y., Wang, G. G., Chen, L. L., Yang, Y. L., & Ding, J. Y. (2018). Fluid inclusion
1110   characteristics as an indicator for tungsten mineralization in the Mesozoic Yaogangxian tungsten
1111   deposit, central Nanling district, South China. *Journal of Geochemical Exploration*, *192*, 1-17.

1112   Lin, X. D., Zhang, C. L., Zhang, D. H. (1987). Vertical zonation of tungsten-bearing quartz veins and
1113   mineralizations in Yaogangxian, Hunan. *Geological Review*, *33*(6), 539-546 (in Chinese with
1114   English abstract).

1115   Liu, Y. J. & Ma, D. S. (1993). Vein-type tungsten deposits of China and adjoining regions. *Ore Geology*
1116   *Reviews*, *8*(3-4), 233-246.

1117   Lu, H. Z. (1986). The origin of tungsten mineral deposits in south China. *Chongqing: Chongqing*
1118   *Publishing House*, 1-230 (in Chinese with English abstract).

1119   Lu, H. Z., Liu, Y., Wang, C., Xu, Y., & Li, H. (2003). Mineralization and fluid inclusion study of the
1120   Shizhuyuan W-Sn-Bi-Mo-F skarn deposit, Hunan Province, China. *Economic Geology*, *98*(5), 955-
1121   974.

1122   Lüders, V. (1996). Contribution of infrared microscopy to fluid inclusion studies in some opaque minerals
1123   (wolframite, stibnite, bournonite); metallogenic implications. *Economic Geology, 91*(8), 1462-1468.

1124   Lynch, J. V. (1989). Hydrothermal alteration, veining, and fluid-inclusion characteristics of the Kalzas
1125   wolframite deposit, Yukon. *Canadian Journal of Earth Sciences, 26*, 2106-2115.

1126   Manning, C. E. (2006). Mobilizing aluminum in crustal and mantle fluids. *Journal of Geochemical*
1127   *Exploration*, *89*(1-3), 251-253.

1128   Mao, J. W., Xie, G. Q., Guo, C. L., & Chen, Y. C. (2007). Largescale tungsten-tin mineralization in the
1129   Nanling region, South China: metallogenic ages and corresponding geodynamic processes. *Acta*
1130   *Petrol. Sin.*, *23*, 2329-2338 (in Chinese with English abstract).

1131   McCaffrey, M. A., Lazar, B. H. D. H., & Holland, H. D. (1987). The evaporation path of seawater and
1132   the coprecipitation of Br (super-) and K (super+) with halite. *Journal of Sedimentary*
1133   *Research*, *57*(5), 928-937.

1134   Moritz, R. (2006). Fluid salinities obtained by infrared microthermometry of opaque minerals:
1135   Implications for ore deposit modeling—a note of caution. *Journal of Geochemical*
1136   *Exploration*, *89*(1-3), 284-287.

1137   Müller, B., Frischknecht, R., Seward, T., Heinrich, C., & Gallegos, W. C. (2001). A fluid inclusion
1138   reconnaissance study of the Huanuni tin deposit (Bolivia), using LA-ICP-MS micro-
1139   analysis. *Mineralium Deposita*, *36*(7), 680-688.

1140   Nahnybida, T., Gleeson, S. A., Rusk, B. G., & Wassenaar, L. I. (2009). Cl/Br ratios and stable chlorine
1141   isotope analysis of magmatic–hydrothermal fluid inclusions from Butte, Montana and Bingham
1142   Canyon, Utah. *Mineralium Deposita*, *44*(8), 837.

1143   Ni, P., Wang, X. D., Wang, G. G., Huang, J. B., Pan, J. Y., & Wang, T. G. (2015). An infrared

microthermometric study of fluid inclusions in coexisting quartz and wolframite from Late Mesozoic tungsten deposits in the Gannan metallogenic belt, South China. *Ore Geology Reviews*, *65*, 1062-1077.

Ni, P., Pan, J. Y., Wang, G. G., Chi, Z., Qin, H., Ding, J. Y., & Chen, H. (2017). A CO_2-rich porphyry ore-forming fluid system constrained from a combined cathodoluminescence imaging and fluid inclusion studies of quartz veins from the Tongcun Mo deposit, South China. *Ore Geology Reviews*, *81*, 856-870.

Onasch, C. M., & Vennemann, T. W. (1995). Disequilibrium partitioning of oxygen isotopes associated with sector zoning in quartz. *Geology*, *23*(12), 1103-1106.

Ottens, B., & Cook, R. B. (2005). The Yaogangxian Tungsten Mine: Yizhang County, Chenzhou, Hunan Province, China.*Rocks & Minerals*, *80*(1), 46-57.

Peng, J., Zhou, M. F., Hu, R., Shen, N., Yuan, S., Bi, X., ... & Qu, W. (2006). Precise molybdenite Re–Os and mica Ar–Ar dating of the Mesozoic Yaogangxian tungsten deposit, central Nanling district, South China. *Mineralium Deposita*, *41*(7), 661-669.

Peretyazhko, I. S., Prokof ev, V. Y., Zagorskii, V. E., & Smirnov, S. Z. (2000). Role of Boric Acids in the Formation of Pegmatite and Hydrothermal Minerals: Petrologic Consequences of Sassolite (H_3BO_3) Discovery in Fluid Inclusions. *PETROLOGY C/C OF PETROLOGIIA*, *8*(3), 214-237.

Pettke, T. (2008). Analytical protocols for element concentration and isotope ratio measurements in fluid inclusions by LA-(MC)-ICP-MS. *Laser Ablation ICP-MS in the Earth Sciences: Current Practices and Outstanding Issues. Mineralogical Association of Canada, Short Course Series*,*40*, 189-218.

Pettke, T., Oberli, F., Audétat, A., Guillong, M., Simon, A. C., Hanley, J. J., & Klemm, L. M. (2012). Recent developments in element concentration and isotope ratio analysis of individual fluid inclusions by laser ablation single and multiple collector ICP-MS. *Ore Geology Reviews*, *44*, 10-38.

Pollard, P. J., Pichavant, M., & Charoy, B. (1987). Contrasting evolution of fluorine-and boron-rich tin systems. *Mineralium Deposita*, *22*(4), 315-321.

Pudack, C., Halter, W. E., Heinrich, C. A., & Pettke, T. (2009). Evolution of magmatic vapor to gold-rich epithermal liquid: The porphyry to epithermal transition at Nevados de Famatina, northwest Argentina. *Economic Geology*, *104*(4), 449-477.

Polya, D. A., Foxford, K. A., Stuart, F., Boyce, A., & Fallick, A. E. (2000). Evolution and paragenetic context of low δD hydrothermal fluids from the Panasqueira W-Sn deposit, Portugal: new evidence from microthermometric, stable isotope, noble gas and halogen analyses of primary fluid inclusions. *Geochimica et Cosmochimica Acta*, *64*(19), 3357-3371.

Ramboz, C., Schnapper, D., Dubessy, J. (1985). The P-V-T-X-fO2 evolution of H2O-CO2-CH4-bearing fluid in a wolframite vein: Reconstruction from fluid inclusion studies. *Geochimica et Cosmochimica Acta, 49*, 205-219.

RGNTD (Research Group for Nanling Tungsten Deposits, Chinese Ministry of Metallurgy) (1985) Tungsten deposits in South China. Publishing House of Metallurgical Industry, Beijing, pp 1–496 (in Chinese with English abstract).

Rios, F. J., Villas, R. N., & Fuzikawa, K. (2003). Fluid evolution in the Pedra Preta wolframite ore deposit, Paleoproterozoic Musa granite, eastern Amazon craton, Brazil. *Journal of South American Earth Sciences*, *15*(7), 787-802.

Roedder, E. (1984). Fluid inclusions. Rev. Mineral. 12, 1-644.

Rosso, K. M., & Bodnar, R. J. (1995). Microthermometric and Raman spectroscopic detection limits of CO_2 in fluid inclusions and the Raman spectroscopic characterization of CO_2. *Geochimica et*

1188   *Cosmochimica Acta*, *59*(19), 3961-3975.

1189   Rusk, B., & Reed, M. (2002). Scanning electron microscope–cathodoluminescence analysis of quartz
1190   reveals complex growth histories in veins from the Butte porphyry copper deposit,
1191   Montana. *Geology*, *30*(8), 727-730.

1192   Samson, I. M., Williams-Jones, A. E., Ault, K. M., Gagnon, J. E., & Fryer, B. J. (2008). Source of fluids
1193   forming distal Zn-Pb-Ag skarns: Evidence from laser ablation-inductively coupled plasma-mass
1194   spectrometry analysis of fluid inclusions from El Mochito, Honduras. *Geology*, *36*(12), 947-950.

1195   Schlöglova, K., Wälle, M., & Heinrich, C. A. (2017). LA-ICP-MS analysis of fluid inclusions:
1196   contamination effects challenging micro-analysis of elements close to their detection limit. *Journal*
1197   *of Analytical Atomic Spectrometry*, *32*(5), 1052-1063.

1198   Schmidt, C., Thomas, R., & Heinrich, W. (2005). Boron speciation in aqueous fluids at 22 to 600 C and
1199   0.1 MPa to 2 GPa. *Geochimica et Cosmochimica Acta*, *69*(2), 275-281.

1200   Seitz, J. C., Pasteris, J. D., & Wopenka, B. (1987). Characterization of CO2-CH4-H2O fluid inclusions
1201   by microthermometry and laser Raman microprobe spectroscopy: Inferences for clathrate and fluid
1202   equilibria.*Geochimica et Cosmochimica Acta*, *51*(6), 1651-1664.

1203   Seo, J. H., Guillong, M., Aerts, M., Zajacz, Z., & Heinrich, C. A. (2011). Microanalysis of S, Cl, and Br
1204   in fluid inclusions by LA–ICP-MS. *Chemical Geology*, *284*(1-2), 35-44.

1205   Shcherba, G. N. (1970). Greisens. *International Geology Review*, *12*(2), 114-150.

1206   Shepherd, T. J., & Waters, P. (1984). Fluid inclusion gas studies, Carrock Fell tungsten deposit, England:
1207   implications for regional exploration. *Mineralium Deposita*, *19*(4), 304-314.

1208   Shu L S. (2007). Geological setting of the Nanling Range. In: Zhou X M, ed. Genesis of Late Mesozoic
1209   Granites and Lithospheric Evolution in the Nanling Range. Beijing: Science Press. 3–22 (in Chiese
1210   with English abstract).

1211   Sirbescu, M. L. C., Krukowski, E. G., Schmidt, C., Thomas, R., Samson, I. M., & Bodnar, R. J. (2013).
1212   Analysis of boron in fluid inclusions by microthermometry, laser ablation ICP-MS, and Raman
1213   spectroscopy: Application to the Cryo-Genie Pegmatite, San Diego County, California,
1214   USA. *Chemical Geology*, *342*, 138-150.

1215   Steele-MacInnis, M. (2018). Fluid inclusions in the system H2O-NaCl-CO2: An algorithm to determine
1216   composition, density and isochore. *Chemical Geology*, *498*, 31-44.

1217   Stefanova, E., Driesner, T., Zajacz, Z., Heinrich, C. A., Petrov, P., & Vasilev, Z. (2014). Melt and fluid
1218   inclusions in hydrothermal veins: The magmatic to hydrothermal evolution of the Elatsite porphyry
1219   Cu-Au deposit, Bulgaria. *Economic Geology*, *109*(5), 1359-1381.

1220   Tagirov, B., Schott, J., & Harrichoury, J. C. (2002). Experimental study of aluminum–fluoride
1221   complexation in near-neutral and alkaline solutions to 300 C. *Chemical Geology*, *184*(3-4), 301-310.

1222   Tagirov, B., Schott, J., Harrichoury, J. C., & Escalier, J. (2004). Experimental study of the stability of
1223   aluminate-borate complexes in hydrothermal solutions 1. *Geochimica et cosmochimica acta*, *68*(6),
1224   1333-1345.

1225   Thomas, R., Förster, H. J., & Heinrich, W. (2003). The behaviour of boron in a peraluminous granite-
1226   pegmatite system and associated hydrothermal solutions: a melt and fluid-inclusion
1227   study. *Contributions to Mineralogy and Petrology*, *144*(4), 457-472.

1228   USGS. (2017). *Mineral Commodity Summary (2012-2016)*.

1229   Van den Kerkhof, A. M., & Hein, U. F. (2001). Fluid inclusion petrography. *Lithos*, *55*(1-4), 27-47.

1230   Wei, W., Hu, R., Bi, X., Peng, J., Su, W., Song, S., & Shi, S. (2012). Infrared microthermometric and
1231   stable isotopic study of fluid inclusions in wolframite at the Xihuashan tungsten deposit, Jiangxi

1232   province, China. *Mineralium Deposita*, *47*(6), 589-605.

1233   Werner, A. B. T., Sinclair, W. D., & Amey, E. B. (2014). International strategic mineral issues summary
1234   report—Tungsten (ver. 1.1, November 2014): US Geological Survey Circular 930–O, 74 p.

1235   Wilkinson, J. J. (2001). Fluid inclusions in hydrothermal ore deposits. *Lithos*, *55*(1-4), 229-272.

1236   Williams-Jones, A. E., & Heinrich, C. A. (2005). 100th Anniversary special paper: vapor transport of
1237   metals and the formation of magmatic-hydrothermal ore deposits. *Economic Geology*, *100*(7),
1238   1287-1312.

1239   Williams-Jones, A. E., Samson, I. M., Ault, K. M., Gagnon, J. E., & Fryer, B. J. (2010). The genesis of
1240   distal zinc skarns: Evidence from the Mochito deposit, Honduras. *Economic Geology*, *105*(8), 1411-
1241   1440.

1242   Wood, S. A., & Samson, I. M. (2000). The hydrothermal geochemistry of tungsten in granitoid
1243   environments: I. Relative solubilities of ferberite and scheelite as a function of T, P, pH, and m
1244   NaCl. *Economic Geology*, *95*(1), 143-182.

1245   Yardley, B. W. D., Banks, D. A., Bottrell, S. H., & Diamond, L. W. (1993). Post-metamorphic gold-quartz
1246   veins from NW Italy: the composition and origin of the ore fluid. *Mineralogical Magazine*, *57*(388),
1247   407-422.

1248   Yuan, S., Williams-Jones, A. E., Mao, J., Zhao, P., Yan, C., & Zhang, D. (2018). The origin of the
1249   Zhangjialong tungsten deposit, South China: Implication for W-Sn mineralization in large granite
1250   batholiths. *Economic Geology*, *113*(5), 1193-1208.

1251   Zaw, U. K., & Thet, D. K. M. (1983). A note on a fluid inclusion study of tin-tungsten mineralization at
1252   Mawchi Mine, Kayah State, Burma. *Economic Geology*, *78*, 530-534.

1253   Zhao, P., Yuan, S., Mao, J., Yuan, Y., Zhao, H., Zhang, D., & Shuang, Y. (2018). Constraints on the timing
1254   and genetic link of the large-scale accumulation of proximal W–Sn–Mo–Bi and distal Pb–Zn–Ag
1255   mineralization of the world-class Dongpo orefield, Nanling Range, South China. *Ore Geology*
1256   *Reviews*, *95*, 1140-1160.

1257   Zhu, X. Y., Wang, Y. L., Cheng, X. Y., Tian, Y., Fu, Q. B., Li, S. T. (2015). Metallogenic system of
1258   Yaogangxian quartz vein type tungsten ore deposit in Hunan. *Mineral Deposits*, 34, 874–894 (in
1259   Chinese with English abstract).

1260

1261   Figure Captions

1262

1263   Fig. 1. Schematic geological map of the Nanling region in the Cathaysian Block, South China,
1264   showing distribution of multiple stage granites and major wolframite-quartz vein type tungsten
1265   deposits. Modified after Mao et al. (2007) and Chen et al. (2013). See online version for color
1266   interpretation.

1267

1268   Fig. 2. Detailed geologic map of the Yaogangxian tungsten deposits, illustrating the surface lithology,
1269   structure and mineralization of the deposits. Modified after unpublished data from Hunan
1270   Yaogangxian Mining Co. Ltd. (2013). See online version for color interpretation.

1271

1272   Fig. 3. Photographs of typical free-grown crystals of coexisting wolframite and quartz collected
1273   from the wolframite-quartz veins in underground mine working between 700 and 1400 m ASL at
1274   Yaogangxian. (a) Aggregation of short tabular wolframite crystals coexisting with several euhedral
1275   quartz and calcite crystals on the tip. (b) Group of parallel, long tabular to prismatic wolframite

1276 crystals with euhedral quartz grown as epitaxial extensions. Both (a) and (b) illustrate a relatively
1277 later paragenetic sequence of quartz than coexisting wolframite. (c-d) 'Front' and 'back' sides of the
1278 studied sample *crystal 1-2* in this paper, showing multi-stage mineral precipitation involving mainly
1279 wolframite, quartz, muscovite and arsenopyrite. Note the directional shadowing of arsenopyrite and
1280 the punctate chamosite on the 'back' side is derived by gravity (see text for discussion). (e)
1281 Magnified details of a euhedral wolframite crystal rooted slightly into the main quartz crystal. (f) A
1282 cubic purple fluorite crystal on the main wolframite crystal. Also shown are octahedral arsenopyrite
1283 and fine-grained euhedral quartz grown on the base of muscovite. (g) Fine-grained chamosite
1284 scattered on the 'back' side of the main quartz crystal, indicating a paleo gravity direction
1285 perpendicular to the precipitation plane which originally faced upward. (h) Small wolframite and
1286 muscovite grains floating beneath the main quartz crystal surface on which the chamosite
1287 precipitated, also indicating a gravity-derived genesis. Pseudosecondary fluid inclusion in the main
1288 quartz crystal can be observed under the given scale. The scales are 1 cm for thick bars and 3 mm
1289 for thin bars unless defined otherwise. Abbreviations: wf = wolframite, qz = quartz, ms = muscovite,
1290 asp = arsenopyrite, fl = fluorite, chm = chamosite, cal = calcite, py = pyrite.

1291

1292 Fig. 4. Panoramic photomicrographs of the whole thin section made from the wolframite-quartz
1293 sample shown in Fig. 3c-h. The section was cut in the direction parallel to the c axis of the main
1294 quartz crystal and perpendicular to the precipitation plane defined by chamosite grains. (a)
1295 Transmitted light panorama showing the contact relationship between different minerals and the
1296 distribution of fluid inclusion trails (clouds of black dots) in quartz. See Fig. 5 to 7 for more detailed
1297 textures and paragenetic relationships in the dashed boxes. (b) SEM-CL photomosaics showing
1298 multiple stages of quartz deposition and fracturing. (c) A derived sketch from SEM-CL, illustrating
1299 the time sequence of successive quartz generations (subscript 'Ps' stands for pseudosecondary) and
1300 the coexisting wolframite and muscovite. Also labeled are three gravity-derived mineral
1301 precipitation zones along the upper crystal face (see Fig. 5 for details). See online version for color
1302 interpretation.

1303

1304 Fig. 5. Magnified photomicrographs of the dashed areas in Fig. 4a, illustrating detailed textures and
1305 paragenetic relationships between minerals and fluid inclusions (see Fig. 6 & 7 for more details in
1306 the dashed boxes). (a-b) Transmitted light and CL images showing small wolframite blades occur
1307 along oscillatory growth zones of Q1. Note the CL-dark Q2 trails are the surface reflection of fluid
1308 inclusion trails underneath. (c-e) Transmitted light, cross-polarized light and CL images showing
1309 several gravity-derived mineral precipitation zones which also define the border of different quartz
1310 generations. Note that small wolframite grains previously observed in Fig. 3h only occur along GD
1311 zone-2. (f-g) Transmitted light and CL images showing multi-stage quartz deposition, fracturing and
1312 fluid inclusion entrapment. Absolute chronological sequence of quartz and fluid inclusion
1313 generations can be determined from their crosscutting relationships. Abbreviations: wf = wolframite,
1314 qz = quartz, ms = muscovite, GD = gravity-derived.

1315

1316 Fig. 6. Magnified photomicrographs of the dashed area in Fig. 5c. (a-b) Transmitted light and CL
1317 images illustrating the affinity between pseudosecondary fluid inclusion trails and quartz trails Q2
1318 and Q4$_{Ps}$. (c) Magnified area in (a), showing rigorous truncation of Ps1-2 trails by GD zone-1 and
1319 Ps4 trails by a GD subzone in Q4, respectively. Abbreviations: wf = wolframite, GD = gravity-

1320   derived.

1321

1322   Fig. 7. Magnified photomicrographs of the dashed area in Fig. 5f. (a-b) Transmitted light and CL

1323   images illustrating the affinity between pseudosecondary fluid inclusion trails and quartz trails Q2,

1324   Q3$_{Ps}$ and Q4$_{Ps}$. (c-d) Magnified area in (a), showing rigorous truncation of Ps1-2, Ps3 and Ps4 trails

1325   by the borders of Q1, Q3 and Q4, respectively. The borders between different quartz generations

1326   can be defined from CL images although no gravity-derived mineral precipitation zone occurs in

1327   the lower part of the crystal.

1328

1329   Fig. 8. Summarized petrographic relationship (a) and relative time sequence (b) between different

1330   mineral and fluid inclusion generations in the studied sample. Abbreviations: wf = wolframite, qz =

1331   quartz, ms = muscovite, asp = arsenopyrite, chm = chamosite.

1332

1333   Fig. 9. Homogenization temperature vs. salinity diagrams for all measured FIAs in the studied

1334   sample. (a) Plots of mean value of each FIA with 1σ error bars. Data are available in Table 1. (b)

1335   Comparison of four FIA data domains derived from (a). (c) Schematic diagram of different fluid

1336   evolution processes predicted from the data distribution trends. Modified after Wilkinson (2001).

1337   See online version for color interpretation.

1338

1339   Fig. 10. Identification of CO_2 in a large primary wolframite-hosted fluid inclusion during

1340   microthermometry. (a) Liquid CO_2 phase was condensed at ca. 3.0 °C only during cooling run,

1341   suggesting phase separation in the metastable absence of clathrate during initial cooling (Diamond,

1342   1992). (b-c) Melting of solid CO_2 phase can be inferred according to the shape of vapor bubble after

1343   overcooling to −95 °C and reheating to −55 °C. The solid CO_2 phase melted at ca. −57.2 °C that is

1344   lower than the CO_2 triple point at −56.6 °C, indicating possible presence of other gases (Seitz et al.,

1345   1987).

1346

1347   Fig. 11. Representative Raman spectra and relative wavenumbers of liquid and gas compositions of

1348   Ps1-2 and Ps3 type fluid inclusions in quartz crystal. All measured at room temperature. (a-b) Raman

1349   spectrum collected from the liquid phase of Ps1-2 type fluid inclusion, with magnified area between

1350   500 and 1500 cm^{-1}. The spectrum shows that minor H_3BO_3 and dissolved CO_2 can be detected in

1351   addition to the dominant H_2O. (c-e) Raman spectrum collected from the vapor phase of the same

1352   Ps1-2 type fluid inclusion measured in (a-b), with magnified areas from 500 to 1500 cm^{-1} and 2200

1353   to 3200 cm^{-1}, respectively. The spectrum shows that CO_2 and CH_4 are the dominant gases in the

1354   vapor phase, whereas minor N_2 and H_2S also occur. Note that unattributed peak centered at ca. 1235

1355   cm^{-1} is also detected in both liquid and vapor phases of Ps1-2 type fluid inclusion. (f) Raman

1356   spectrum of vapor phase of Ps3 type fluid inclusion, showing significantly weaker CO_2 and CH_4

1357   intensities compared with Ps1-2 fluid inclusion. Abbreviations: AS = aqueous solution; V = vapor.

1358

1359   Fig. 12. Summary plots showing average homogenization temperatures (Th), salinities and element

1360   concentration ratios X/(Na + K) of studied fluid inclusion assemblages of Pw, Ps1-2 and Ps3 types.

1361   All error bars are at 1σ. Within each FIA type the values are ordered according to the FIA No. For

1362   As, Sr, S, Sb and Cu, the minimum limits of detection (LODs) in each FIA are also plotted as

1363   estimated upper limit for actual values. S in all Pw type inclusions are below LODs in which all

1364   except one are too high to be plotted. The plotted LA-ICP-MS data are tabulated in Table 2 while
1365   data for all other elements are available in Table S2.

1366

1367   Fig. 13. Comparison of fluid chemistry between Pw, Ps1-2 and Ps3 type fluid inclusions. (a-c) Plots
1368   of average element concentration ratios X/(Na + K) of Pw vs. Ps1-2, Ps3 vs. Ps1-2 and Pw vs. Ps3,
1369   respectively. All error bars are at 1σ. In each diagram, only those elements detected in both fluid
1370   inclusion types are plotted. Most elements have consistent concentration ratios in all fluid inclusions
1371   except B, As, Sr and Cu. (d) Ternary plot of B, As, Sr in different fluid inclusion types, showing
1372   conspicuously distinct chemical domains with respect to these three elements. Each symbol
1373   represents a single fluid inclusion.

1374

1375   Fig. 14. Plots of homogenization temperatures versus W and Mn concentration ratios X/(Na + K)
1376   for all measured Ps1-2 and Ps3 type fluid inclusions. The nearly random-distributed symbols in both
1377   (a) and (b) suggest that W and Mn concentrations in ore-forming fluids are not controlled by fluid
1378   temperature within the plotted range (i.e. 220 to 320 °C).

1379

1380   Fig. 15. Plots of element concentration ratios of B, As, Sb and S against Na in Pw, Ps1-2 and Ps3
1381   FIAs. Note Pw inclusions data are slightly to the left because they have higher K concentration. All
1382   error bars are at 1σ. The hollow symbols indicate the minimum limits of detection (LODs) of
1383   element in each FIA.

1384

1385   Fig. 16. Diagrams of selected element concentrations and concentration ratios of Pw, Ps1-2 and Ps3
1386   FIAs used for discriminating fluid sources. All error bars are at 1σ. Data for magmatic-hydrothermal
1387   fluids and basinal brines in (a) and (b) are sourced from Samson et al. (2008) and Williams-Jones et
1388   al. (2010). Br/Cl ranges for evaporates and different ore deposit settings are modified from
1389   Lecumberri-Sanchez and Bodnar (2018); fluid Br/Cl values for Panasqueira W-Sn, Mole Granite
1390   Sn-W and St. Austell Sn-W deposits are from Polya et al. (2000), Seo et al. (2011) and Irwin and
1391   Roedder (1995), respectively. The reference value for seawater (1.54×10^{-3}) is from McCaffrey et
1392   al. (1987), whereas the mantle values (ca. $1-2 \times 10^{-3}$) are from Déruelle et al. (1992), Jambon et al.
1393   (1995) and Johnson et al. (2000). Dilution lines are added in (c) and (d) to overcome the
1394   miscalculation of absolute concentrations and possible dilution by meteoric water.
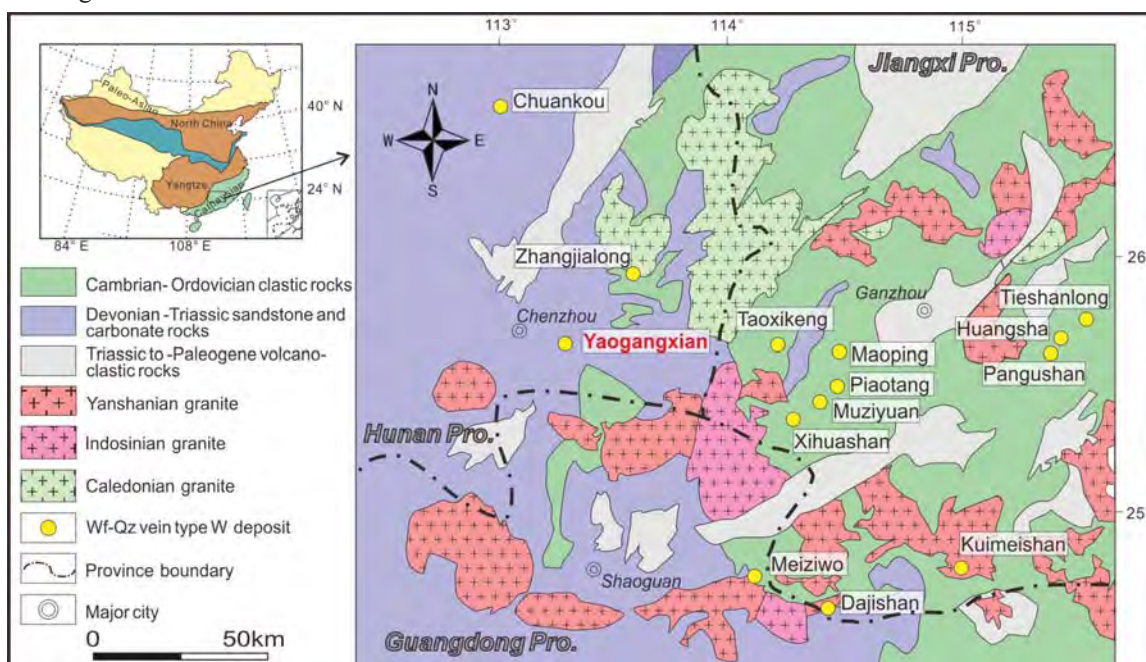
1395
1396

Fig. 1

Fig. 1. Schematic geological map of the Nanling region in the Cathaysian Block, South China, showing distribution of multiple stage granites and major wolframite-quartz vein type tungsten deposits. Modified after Mao et al. (2007) and Chen et al. (2013). See online version for color interpretation.
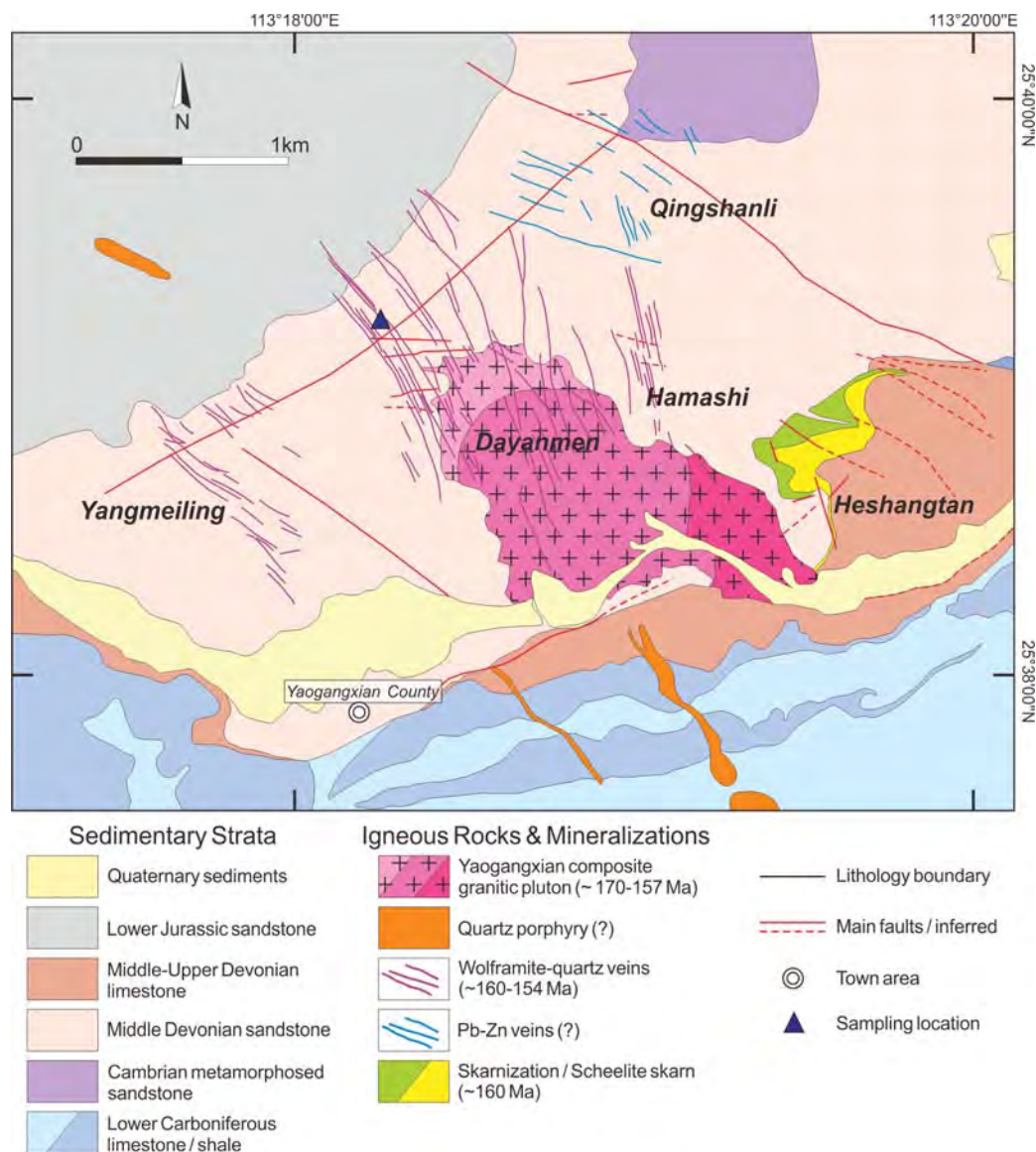
Fig. 2

Fig. 2. Detailed geologic map of the Yaogangxian tungsten deposits, illustrating the surface lithology, structure and mineralization of the deposits. Modified after unpublished data from Hunan Yaogangxian Mining Co. Ltd. (2013). See online version for color interpretation.
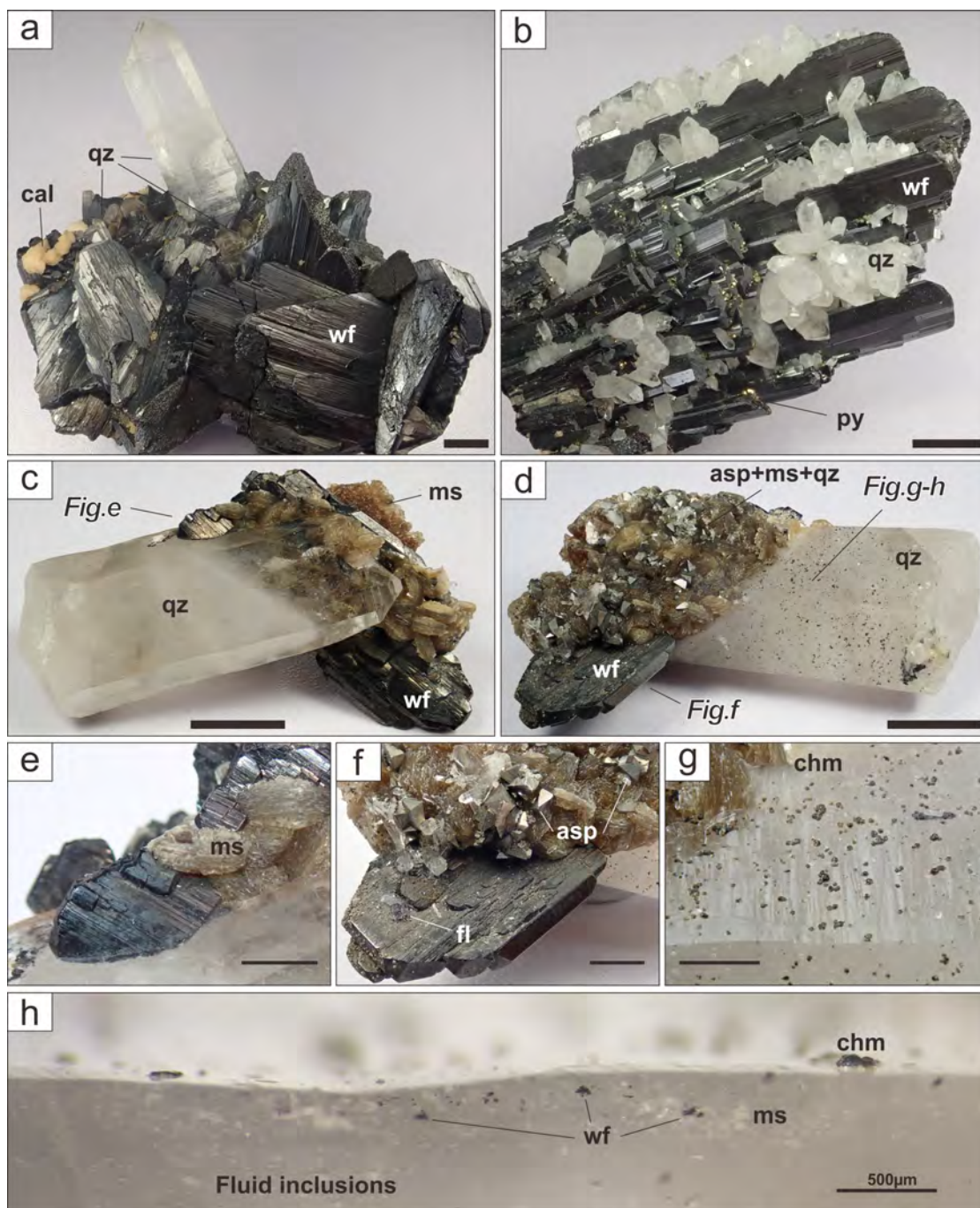
Fig. 3

Fig. 3. Photographs of typical free-grown crystals of coexisting wolframite and quartz collected from the wolframite-quartz veins in underground mine working between 700 and 1400 m ASL at Yaogangxian. (a) Aggregation of short tabular wolframite crystals coexisting with several euhedral quartz and calcite crystals on the tip. (b) Group of parallel, long tabular to prismatic wolframite crystals with euhedral quartz grown as epitaxial extensions. Both (a) and (b) illustrate a relatively later paragenetic sequence of quartz than coexisting wolframite. (c-d) 'Front' and 'back' sides of the studied sample *crystal 1-2* in this paper, showing multi-stage mineral precipitation involving mainly wolframite, quartz, muscovite and arsenopyrite. Note the directional shadowing of arsenopyrite and the punctate chamosite on the 'back' side is derived by gravity (see text for discussion). (e)

Magnified details of a euhedral wolframite crystal rooted slightly into the main quartz crystal. (f) A cubic purple fluorite crystal on the main wolframite crystal. Also shown are octahedral arsenopyrite and fine-grained euhedral quartz grown on the base of muscovite. (g) Fine-grained chamosite scattered on the 'back' side of the main quartz crystal, indicating a paleo gravity direction perpendicular to the precipitation plane which originally faced upward. (h) Small wolframite and muscovite grains floating beneath the main quartz crystal surface on which the chamosite precipitated, also indicating a gravity-derived genesis. Pseudosecondary fluid inclusion in the main quartz crystal can be observed under the given scale. The scales are 1 cm for thick bars and 3 mm for thin bars unless defined otherwise. Abbreviations: wf = wolframite, qz = quartz, ms = muscovite, asp = arsenopyrite, fl = fluorite, chm = chamosite, cal = calcite, py = pyrite.
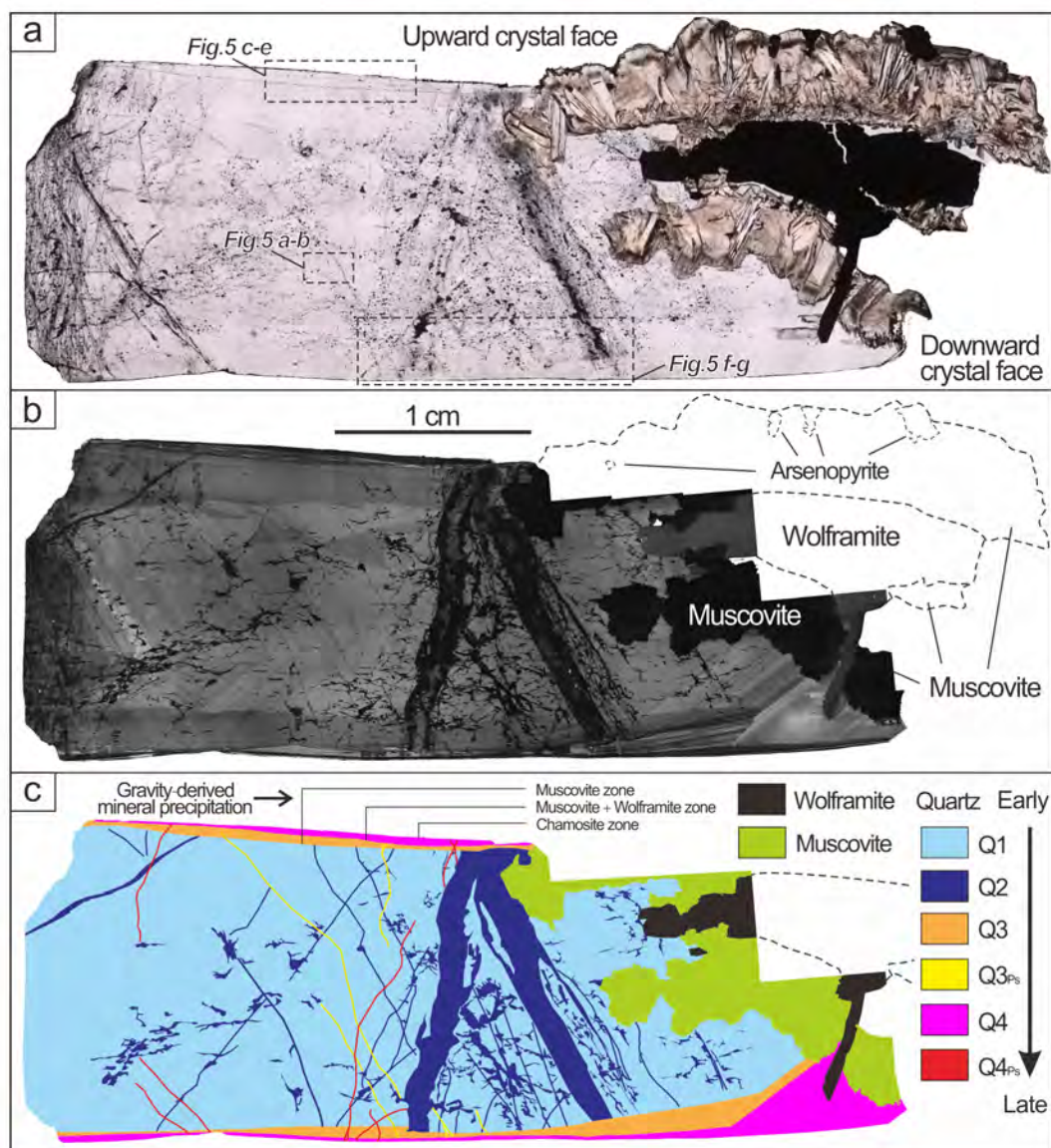
Fig. 4

Fig. 4. Panoramic photomicrographs of the whole thin section made from the wolframite-quartz sample shown in Fig. 3c-h. The section was cut in the direction parallel to the c axis of the main quartz crystal and perpendicular to the precipitation plane defined by chamosite grains. (a) Transmitted light panorama showing the contact relationship between different minerals and the distribution of fluid inclusion trails (clouds of black dots) in quartz. See Fig. 5 to 7 for more detailed textures and paragenetic relationships in the dashed boxes. (b) SEM-CL photomosaics showing multiple stages of quartz deposition and fracturing. (c) A derived sketch from SEM-CL, illustrating the time sequence of successive quartz generations (subscript 'Ps' stands for pseudosecondary) and the coexisting wolframite and muscovite. Also labeled are three gravity-derived mineral precipitation zones along the upper crystal face (see Fig. 5 for details). See online version for color interpretation.

Fig. 5

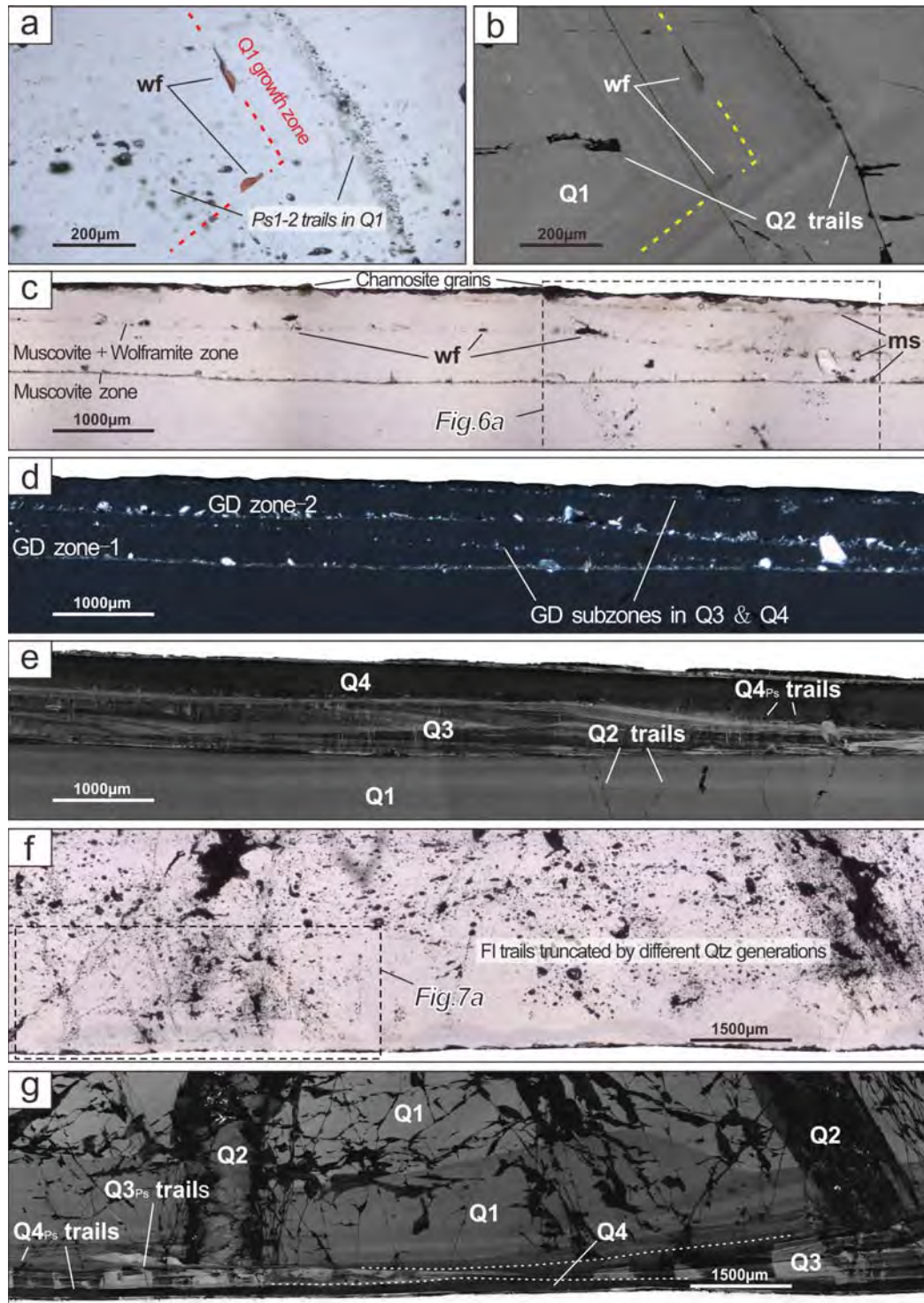Fig. 5. Magnified photomicrographs of the dashed areas in Fig. 4a, illustrating detailed textures and paragenetic relationships between minerals and fluid inclusions (see Fig. 6 & 7 for more details in the dashed boxes). (a-b) Transmitted light and CL images showing small wolframite blades occur along oscillatory growth zones of Q1. Note the CL-dark Q2 trails are the surface reflection of fluid

inclusion trails underneath. (c-e) Transmitted light, cross-polarized light and CL images showing several gravity-derived mineral precipitation zones which also define the border of different quartz generations. Note that small wolframite grains previously observed in Fig. 3h only occur along GD zone-2. (f-g) Transmitted light and CL images showing multi-stage quartz deposition, fracturing and fluid inclusion entrapment. Absolute chronological sequence of quartz and fluid inclusion generations can be determined from their crosscutting relationships. Abbreviations: wf = wolframite, qz = quartz, ms = muscovite, GD = gravity-derived.

Fig. 6

Fig. 6. Magnified photomicrographs of the dashed area in Fig. 5c. (a-b) Transmitted light and CL images illustrating the affinity between pseudosecondary fluid inclusion trails and quartz trails Q2 and Q4$_{Ps}$. (c) Magnified area in (a), showing rigorous truncation of Ps1-2 trails by GD zone-1 and Ps4 trails by a GD subzone in Q4, respectively. Abbreviations: wf = wolframite, GD = gravity-derived.
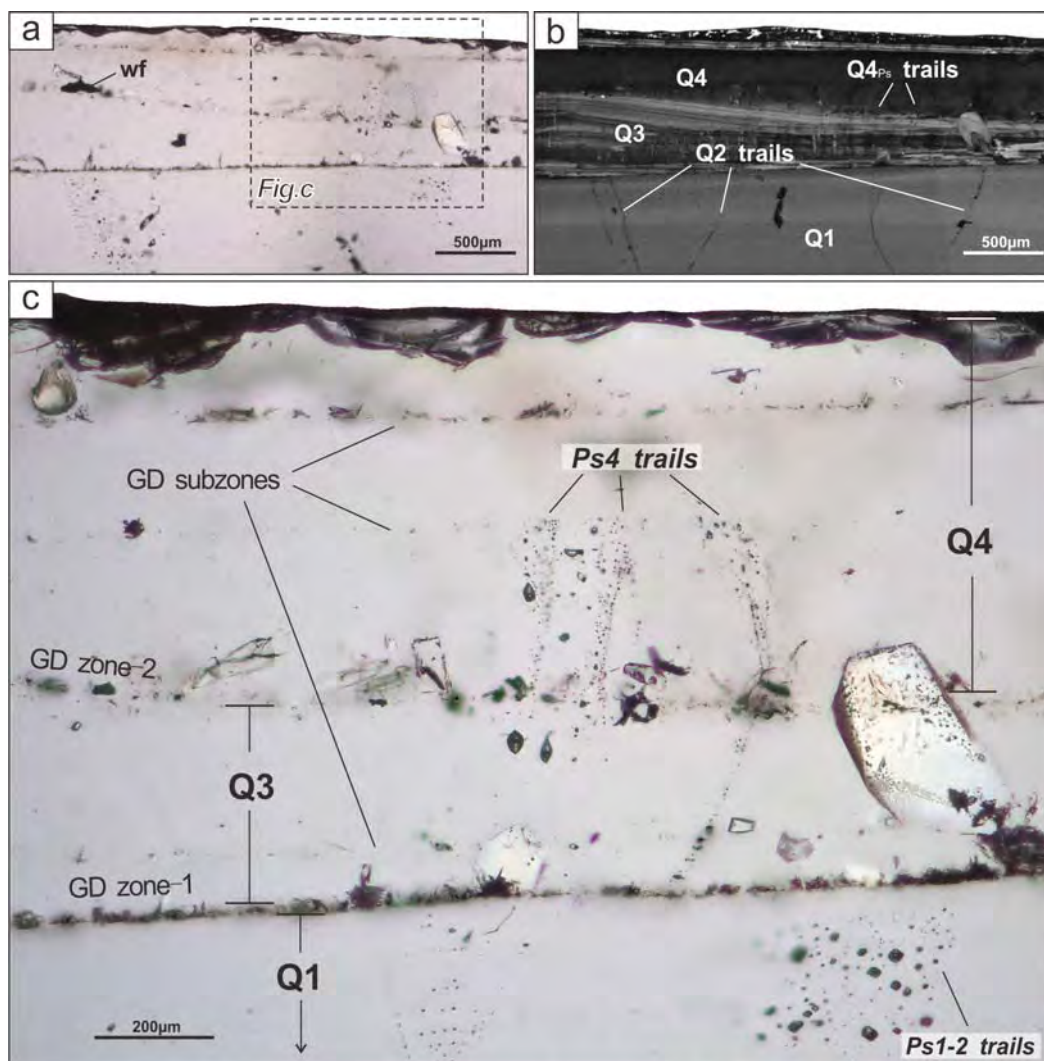
Fig. 7
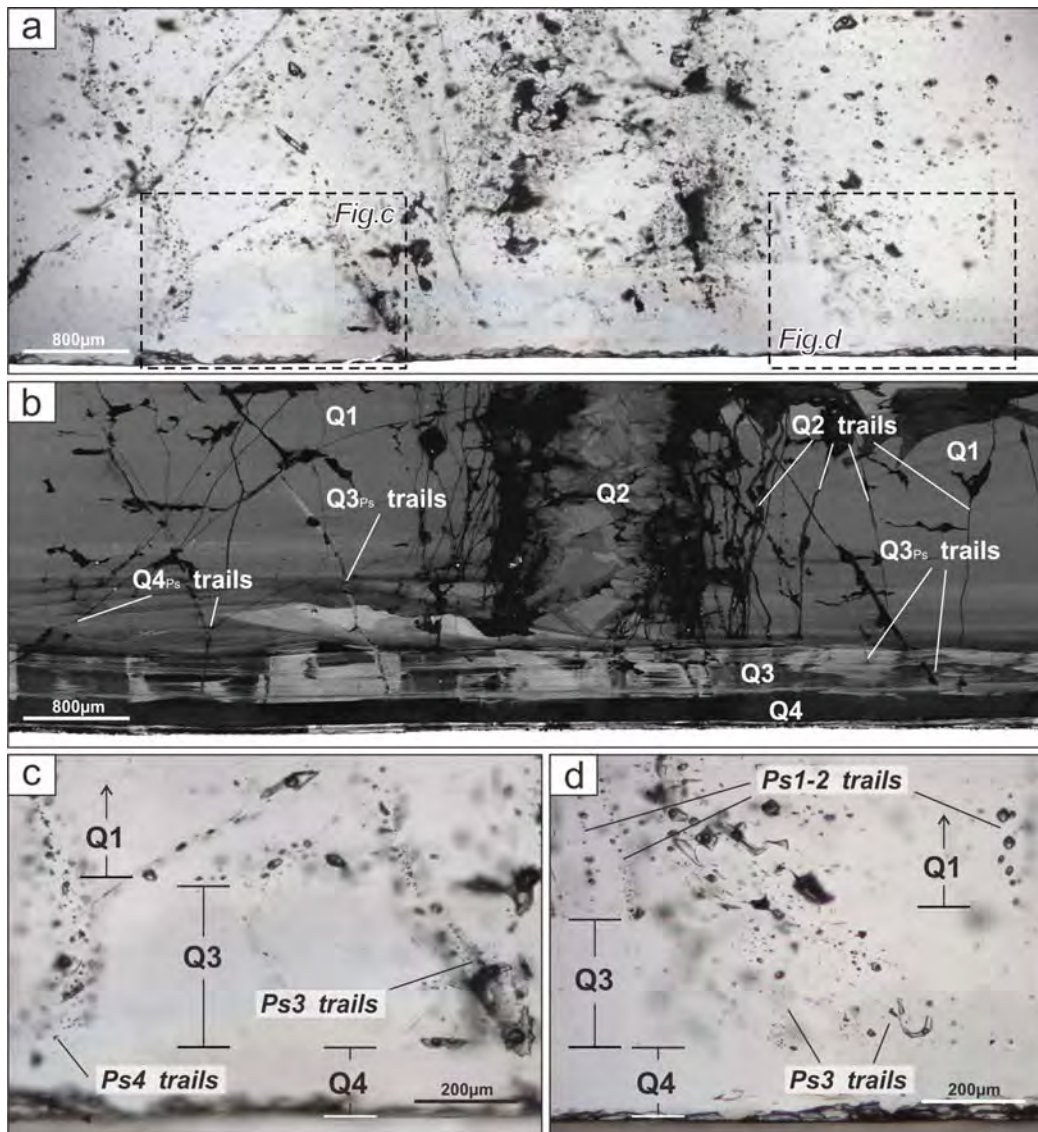
Fig. 7. Magnified photomicrographs of the dashed area in Fig. 5f. (a-b) Transmitted light and CL images illustrating the affinity between pseudosecondary fluid inclusion trails and quartz trails Q2, Q3$_{Ps}$ and Q4$_{Ps}$. (c-d) Magnified area in (a), showing rigorous truncation of Ps1-2, Ps3 and Ps4 trails by the borders of Q1, Q3 and Q4, respectively. The borders between different quartz generations can be defined from CL images although no gravity-derived mineral precipitation zone occurs in the lower part of the crystal.

Fig. 8
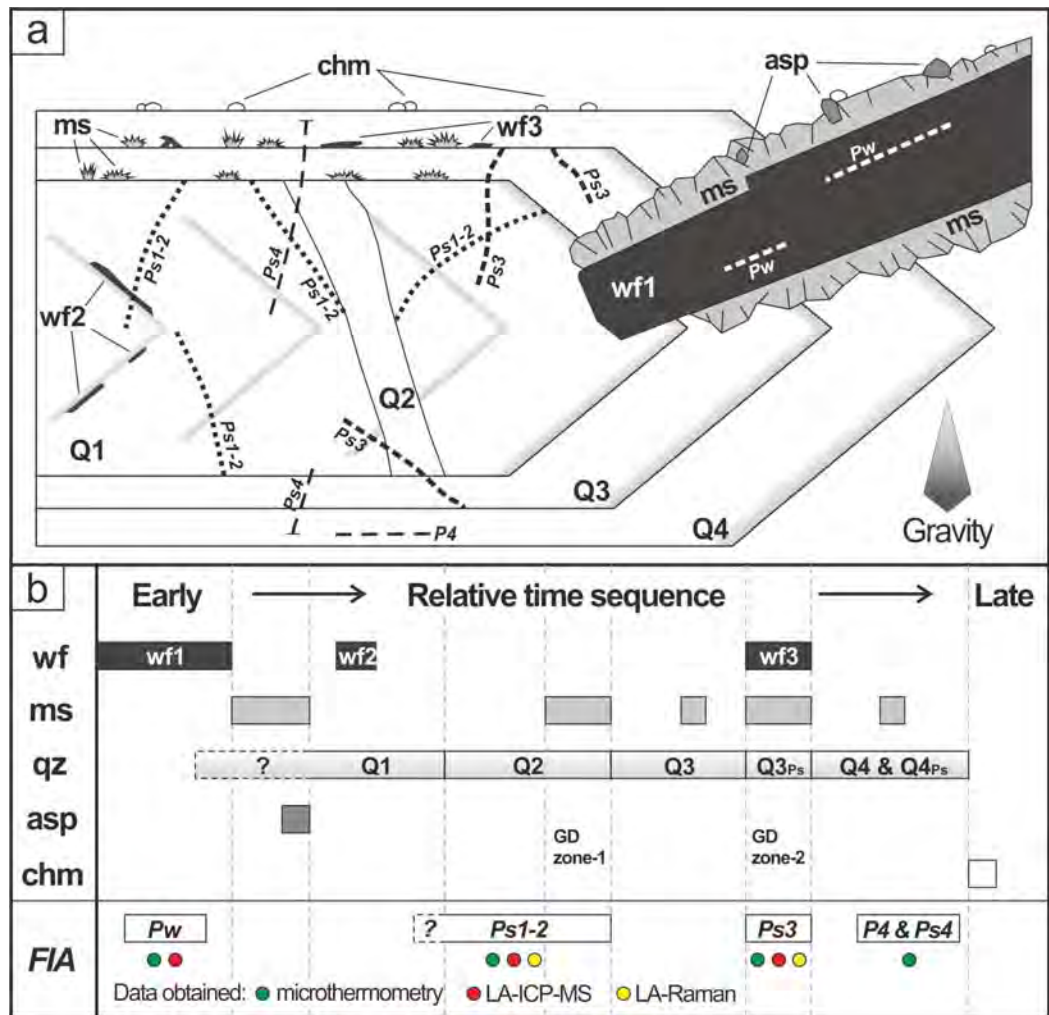
Fig. 8. Summarized petrographic relationship (a) and relative time sequence (b) between different mineral and fluid inclusion generations in the studied sample. Abbreviations: wf = wolframite, qz = quartz, ms = muscovite, asp = arsenopyrite, chm = chamosite.

Fig. 9
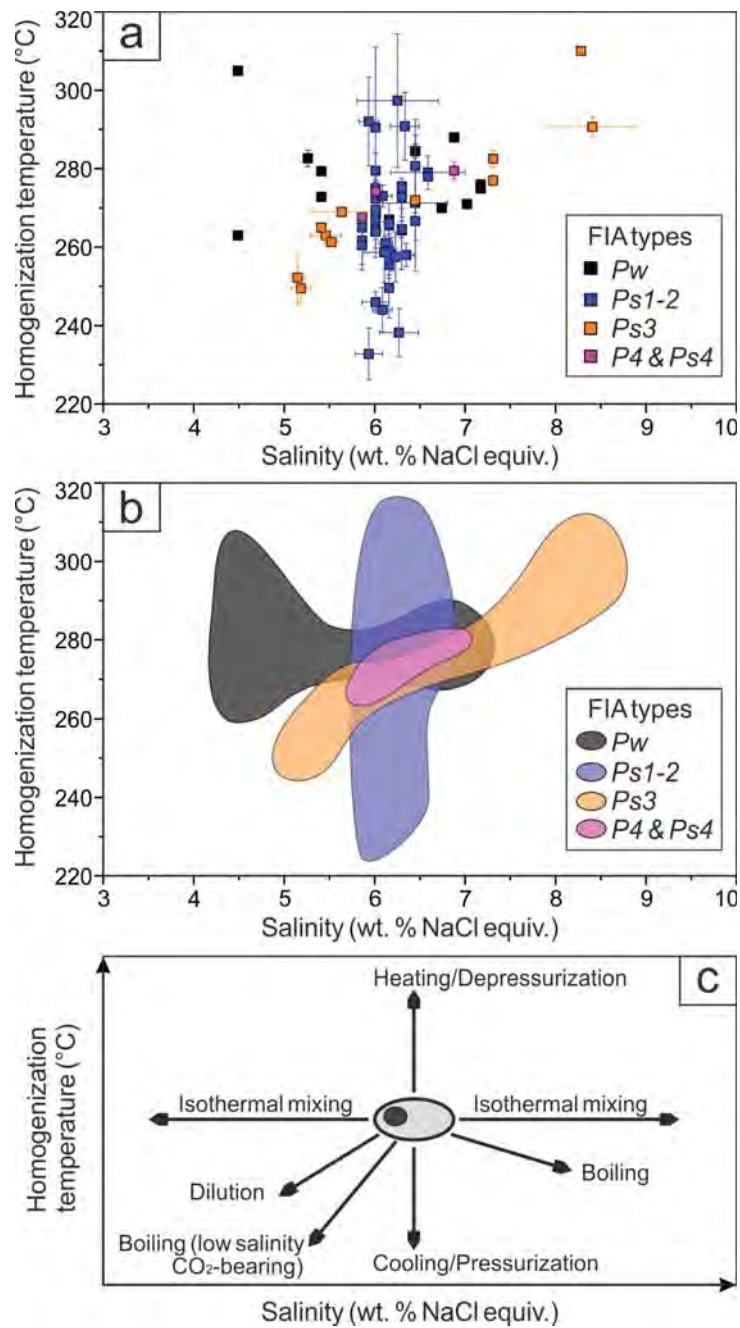
Fig. 9. Homogenization temperature vs. salinity diagrams for all measured FIAs in the studied sample. (a) Plots of mean value of each FIA with 1σ error bars. Data are available in Table 1. (b) Comparison of four FIA data domains derived from (a). (c) Schematic diagram of different fluid evolution processes predicted from the data distribution trends. Modified after Wilkinson (2001). See online version for color interpretation.

Fig. 10
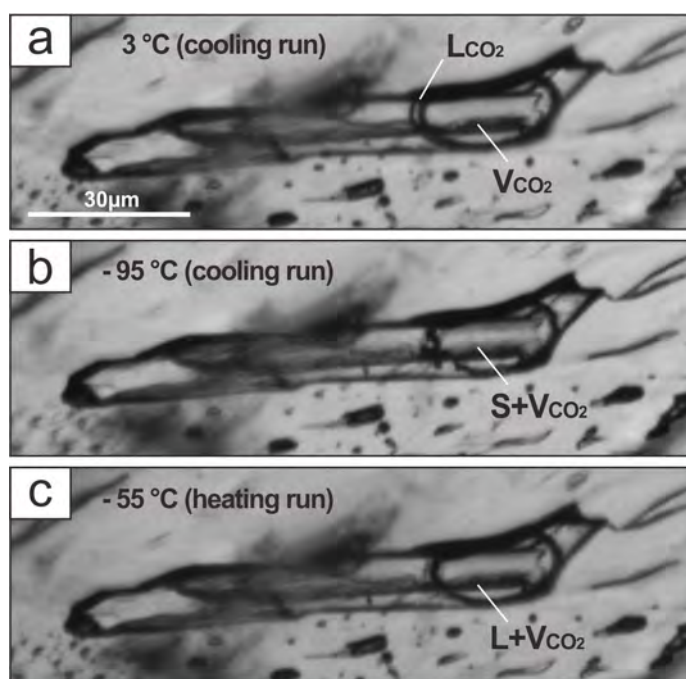
Fig. 10. Identification of CO_2 in a large primary wolframite-hosted fluid inclusion during microthermometry. (a) Liquid CO_2 phase was condensed at ca. 3.0 °C only during cooling run, suggesting phase separation in the metastable absence of clathrate during initial cooling (Diamond, 1992). (b-c) Melting of solid CO_2 phase can be inferred according to the shape of vapor bubble after overcooling to −95 °C and reheating to −55 °C. The solid CO_2 phase melted at ca. −57.2 °C that is lower than the CO_2 triple point at −56.6 °C, indicating possible presence of other gases (Seitz et al., 1987).

Fig. 11
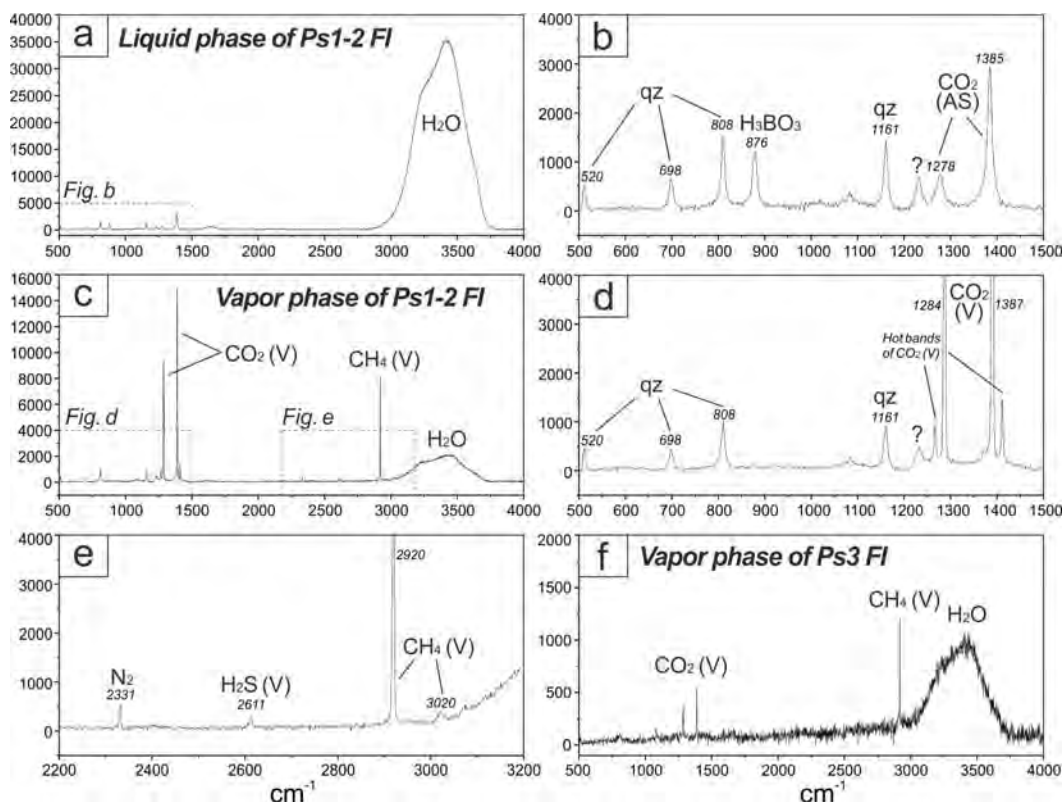
Fig. 11. Representative Raman spectra and relative wavenumbers of liquid and gas compositions of Ps1-2 and Ps3 type fluid inclusions in quartz crystal. All measured at room temperature. (a-b) Raman spectrum collected from the liquid phase of Ps1-2 type fluid inclusion, with magnified area between 500 and 1500 cm^{-1}. The spectrum shows that minor H_3BO_3 and dissolved CO_2 can be detected in addition to the dominant H_2O. (c-e) Raman spectrum collected from the vapor phase of the same Ps1-2 type fluid inclusion measured in (a-b), with magnified areas from 500 to 1500 cm^{-1} and 2200 to 3200 cm^{-1}, respectively. The spectrum shows that CO_2 and CH_4 are the dominant gases in the vapor phase, whereas minor N_2 and H_2S also occur. Note that unattributed peak centered at ca. 1235 cm^{-1} is also detected in both liquid and vapor phases of Ps1-2 type fluid inclusion. (f) Raman spectrum of vapor phase of Ps3 type fluid inclusion, showing significantly weaker CO_2 and CH_4 intensities compared with Ps1-2 fluid inclusion. Abbreviations: AS = aqueous solution; V = vapor.

Fig. 12
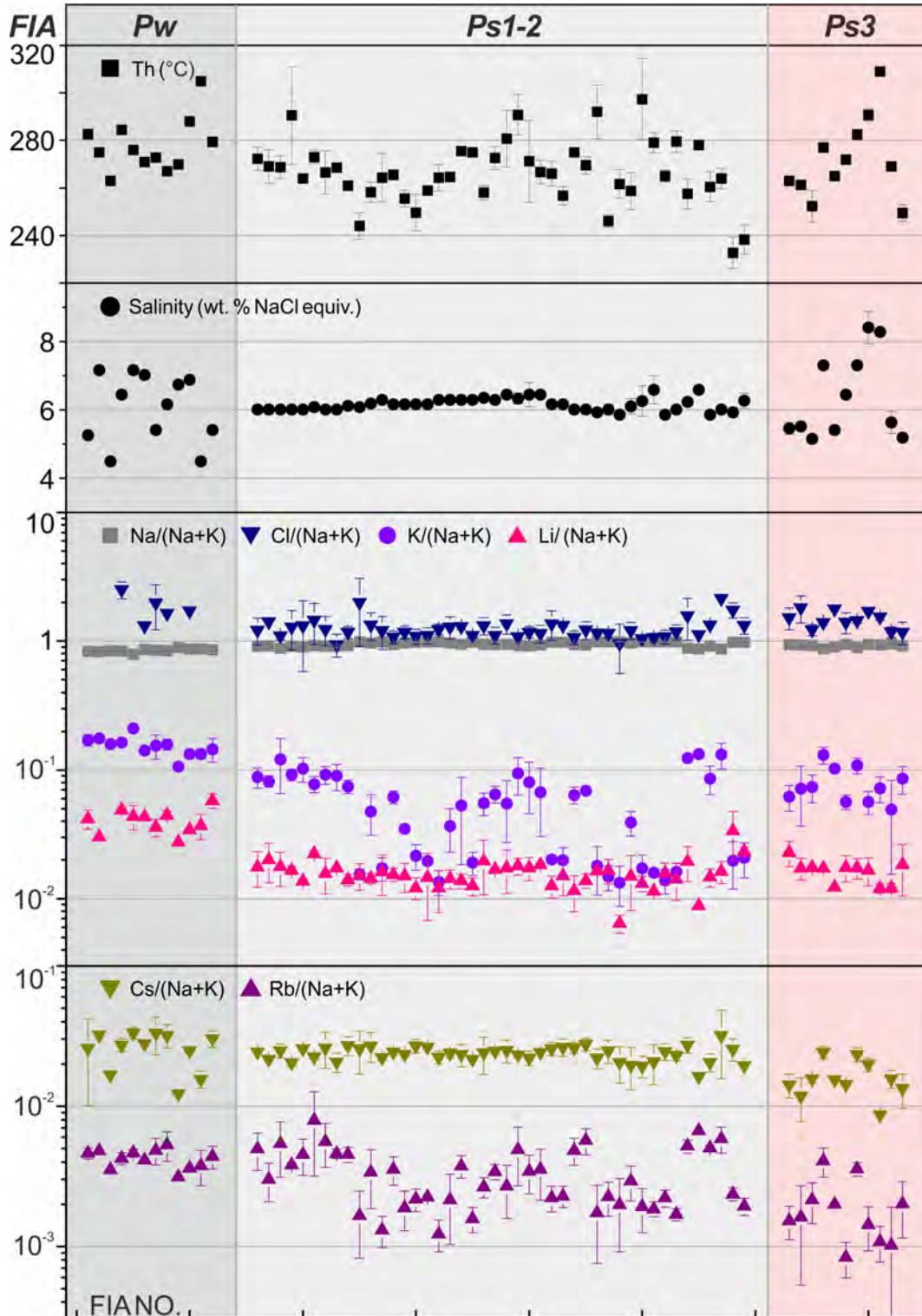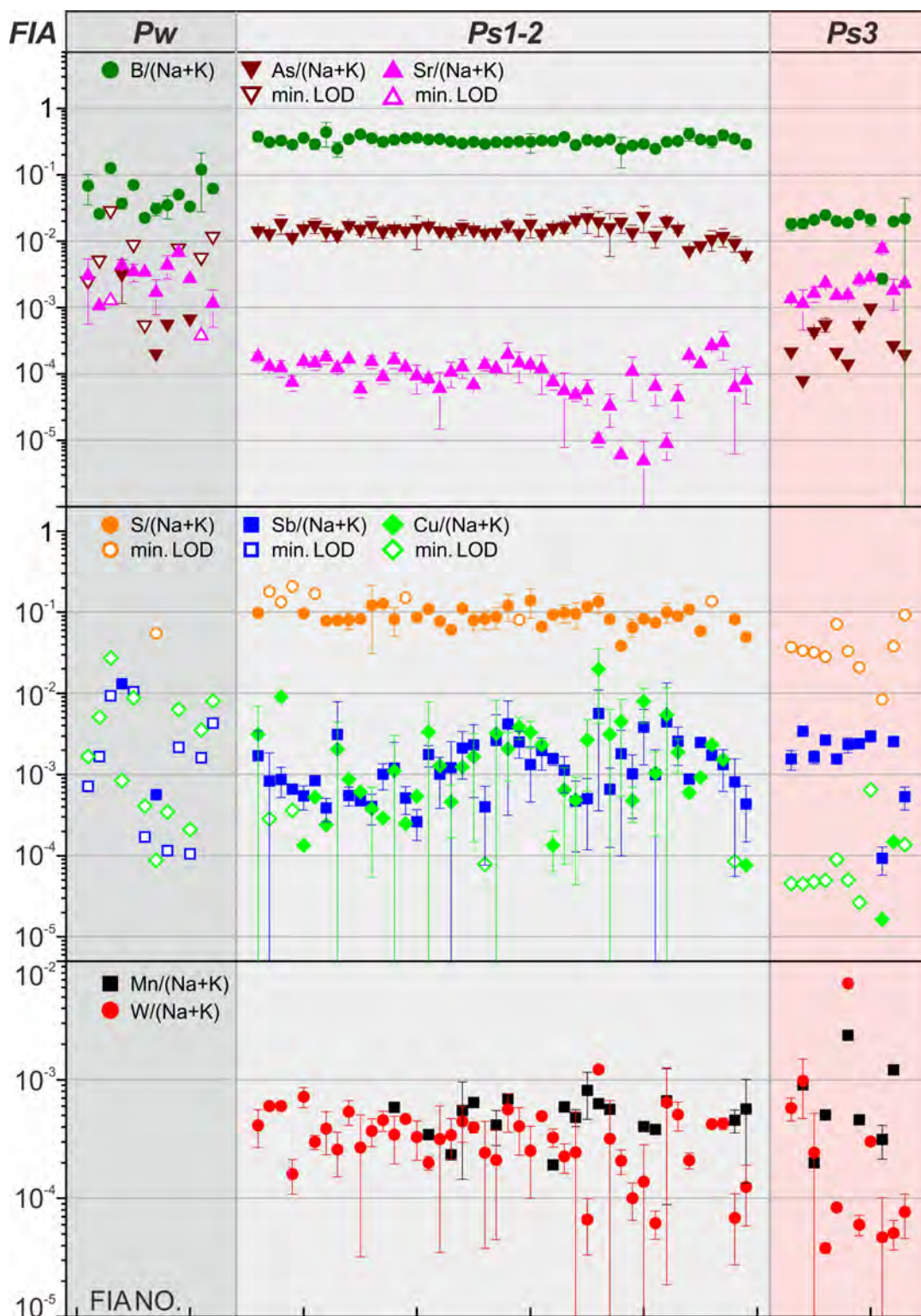
Fig. 12. Summary plots showing average homogenization temperatures (Th), salinities and element concentration ratios X/(Na + K) of studied fluid inclusion assemblages of Pw, Ps1-2 and Ps3 types. All error bars are at 1σ. Within each FIA type the values are ordered according to the FIA No. For As, Sr, S, Sb and Cu, the minimum limits of detection (LODs) in each FIA are also plotted as estimated upper limit for actual values. S in all Pw type inclusions are below LODs in which all except one are too high to be plotted. The plotted LA-ICP-MS data are tabulated in Table 2 while data for all other elements are available in Table S2.

Fig. 13
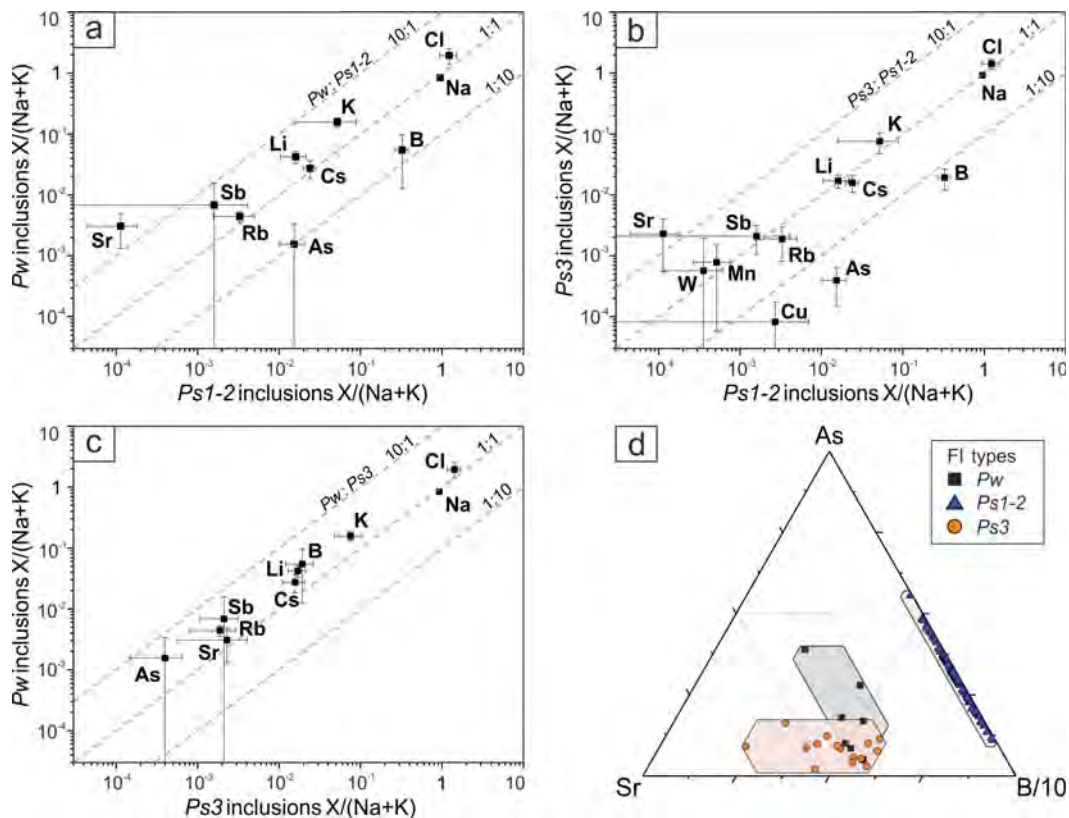
Fig. 13. Comparison of fluid chemistry between Pw, Ps1-2 and Ps3 type fluid inclusions. (a-c) Plots of average element concentration ratios X/(Na + K) of Pw vs. Ps1-2, Ps3 vs. Ps1-2 and Pw vs. Ps3, respectively. All error bars are at 1σ. In each diagram, only those elements detected in both fluid inclusion types are plotted. Most elements have consistent concentration ratios in all fluid inclusions except B, As, Sr and Cu. (d) Ternary plot of B, As, Sr in different fluid inclusion types, showing conspicuously distinct chemical domains with respect to these three elements. Each symbol represents a single fluid inclusion. Same color codes are used in all following figures.

Fig. 14
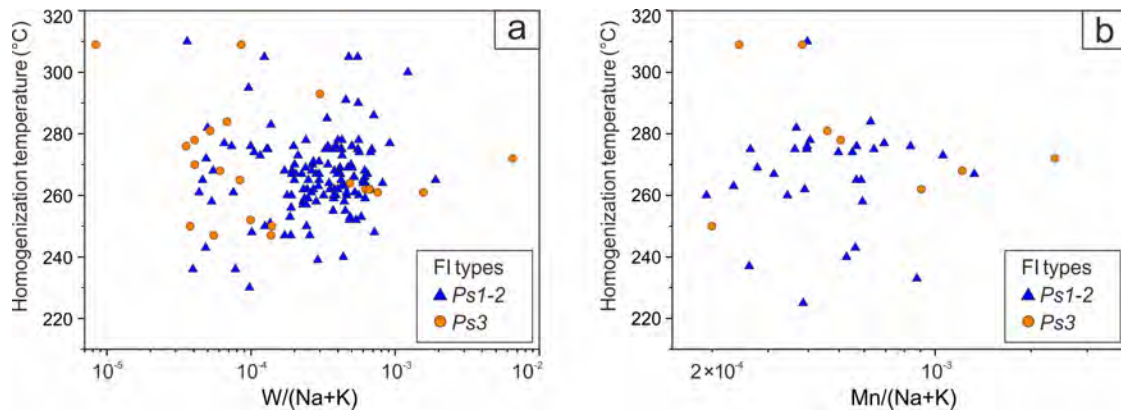
Fig. 14. Plots of homogenization temperatures versus W and Mn concentration ratios X/(Na + K) for all measured Ps1-2 and Ps3 type fluid inclusions. The nearly random-distributed symbols in both (a) and (b) suggest that W and Mn concentrations in ore-forming fluids are not controlled by fluid temperature within the plotted range (i.e. 220 to 320 °C).

Fig. 15
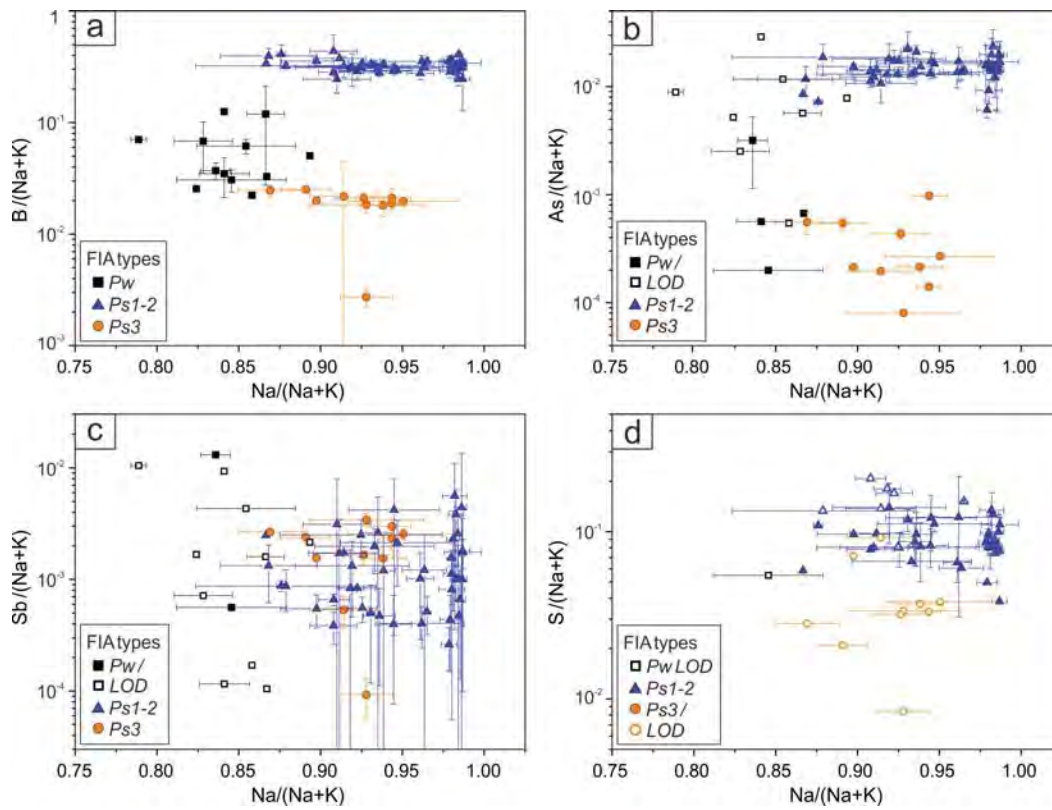
Fig. 15. Plots of element concentration ratios of B, As, Sb and S against Na in Pw, Ps1-2 and Ps3 FIAs. Note Pw inclusions data are slightly to the left because they have higher K concentration. All error bars are at 1σ. The hollow symbols indicate the minimum limits of detection (LODs) of element in each FIA.

Fig. 16
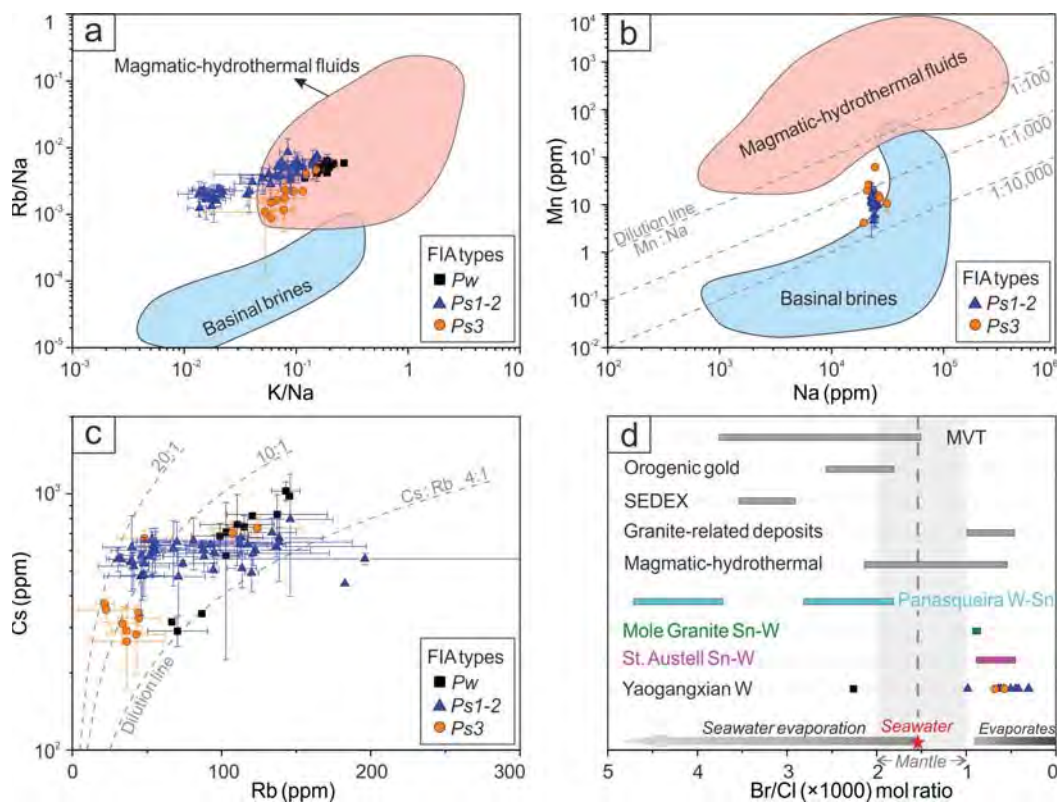
Fig. 16. Diagrams of selected element concentrations and concentration ratios of Pw, Ps1-2 and Ps3 FIAs used for discriminating fluid sources. All error bars are at 1σ. Data for magmatic-hydrothermal fluids and basinal brines in (a) and (b) are sourced from Samson et al. (2008) and Williams-Jones et al. (2010). Br/Cl ranges for evaporates and different ore deposit settings are modified from Lecumberri-Sanchez and Bodnar (2018); fluid Br/Cl values for Panasqueira W-Sn, Mole Granite Sn-W and St. Austell Sn-W deposits are from Polya et al. (2000), Seo et al. (2011) and Irwin and Roedder (1995), respectively. The reference value for seawater (1.54×10^{-3}) is from McCaffrey et al. (1987), whereas the mantle values (ca. $1\text{-}2 \times 10^{-3}$) are from Déruelle et al. (1992), Jambon et al. (1995) and Johnson et al. (2000). Dilution lines are added in (c) and (d) to overcome the miscalculation of absolute concentrations and possible dilution by meteoric water. All diagrams share the same color codes.

Table 1. General characteristics of all measured fluid inclusion in the studied coexisting wolframite and quartz crystals from Yaogangxian

FI type	Host mineral generation	Phase description at room temperature	Size μm	Total number (FIA number)	Salinity wt. %[1]	Average ± σ	Th °C	Average ± σ	Raman gases
Pw	wf1	L-V, liquid-rich	15 ~ 120	28 (12)	4.5 ~ 7.2	5.8 ± 0.9	263 ~ 305	279 ± 11	CO_2[2]
Ps1-2	Q1-2	L-V, liquid-rich	15 ~ 80	147 (44)	5.9 ~ 6.6	6.2 ± 0.2	233 ~ 297	266 ± 14	CO_2, CH_4, N_2, H_2S
Ps3	Q3$_{Ps}$	L-V, liquid-rich	15 ~ 40	27 (11)	5.2 ~ 8.4	6.3 ± 1.2	250 ~ 310	270 ± 17	CO_2, CH_4
P4	Q4	L-V, liquid-rich	5 ~ 10	3 (1)	5.9	5.9	268	268	n.d.
Ps4	Q4$_{Ps}$	L-V, liquid-rich	5 ~ 15	7 (2)	6.0 ~ 6.9	6.2 ± 0.4	274 ~ 280	276 ± 3	n.d.

Notes: Salinity and Th ranges are summarized based on average values of each fluid inclusion assemblage. The average values reported here are calculated using all fluid inclusions of each type, and are presented with 1 standard deviation (± σ). n.d. = not determined.

[1] Apparent salinities of fluid inclusions in wt. % NaCl equiv.

[2] Identified via microthermometry.

Table 2. Summary of salinities, homogenization temperatures and main elemental concentrations of 67 FIAs in coexisting wolframite and quartz from Yaogangxian

FIA (N)[1]	Sa.[2]	Th (°C)	Li (ppm)	B (ppm)	Na (wt. %)	S (ppm)	Cl (wt. %)	K (ppm)	Mn (ppm)	As (ppm)	Cu (ppm)	Rb (ppm)	Sr (ppm)	Sb (ppm)	Cs (ppm)	W (ppm)
Primary FIAs in wolframite (Pw type, N=12)																
81(3)	5.3	283	928 ± 155	1520 ± 752	1.84 ± 0.03	-	-	3827 ± 430	n.d.	-	-	102.9 ± 8.8	66.2 ± 53.6	-	575 ± 349	n.d.
85(1)	7.2	275	918	776	2.51	-	-	5352	n.d.	-	-	145.6	31.9	-	980	n.d.
86(1)	4.5	263	-	2374	1.59	-	-	3004	n.d.	-	-	66.6	-	-	316	n.d.
87(4)	6.5	285	1329 ± 81	1008 ± 179	2.27 ± 0.02	-	6.82 ± 1.02	4467 ± 265	n.d.	86 ± 55	-	115.2 ± 11.3	117.4 ± 12.9	356.5	743 ± 79	n.d.
88(2)	7.2	276	1345 ± 286	2172	2.44 ± 0.01	-	-	6523 ± 158	n.d.	-	-	143.1 ± 9.6	106.6 ± 31.9	-	1026 ± 89	n.d.
89(1)	7.0	271	1268	655	2.52	-	3.85	4164	n.d.	-	-	120.6	100.2	-	820	n.d.
90(5)	5.4	273	817 ± 132	698 ± 160	1.92 ± 0.05	-	4.48 ± 1.81	3522 ± 798	n.d.	4	-	110.4 ± 24.7	38.3 ± 20.9	12.5	759 ± 235	n.d.
91(3)	6.2	267	1158 ± 96	904 ± 356	2.18 ± 0.03	-	4.24	4120 ± 426	n.d.	15	-	137.3 ± 33.6	112.7 ± 43.7	-	831 ± 162	n.d.
92(1)	6.7	270	763	1398	2.48	-	-	2956	n.d.	-	-	86.8	186.1	-	341	n.d.
93(1)	6.9	288	985	942	2.48	-	4.92	3804	n.d.	19	250	103.1	77.8	-	710	n.d.
94(3)	4.5	305	690 ± 153	2235 ± 1722	1.62 ± 0.01	-	-	2498 ± 227	n.d.	-	-	70.5 ± 20.1	-	-	291 ± 38	n.d.
95(3)	5.4	279	1314 ± 182	1397 ± 219	1.93 ± 0.04	-	-	3303 ± 724	n.d.	-	-	98.9 ± 19.2	26.4 ± 15.3	-	684 ± 83	n.d.
Pseudosecondary FIAs in Qtz 1-2 (PS1-2 type, N=44)																
1(3)	6.0	272	438 ± 136	9293 ± 1587	2.26 ± 0.02	2399	3.01 ± 0.73	2189 ± 413	-	354 ± 31	77.5 ± 92	122.6 ± 37.1	4.5 ± 0.8	42.6 ± 43.7	602 ± 16	10.2 ± 3.7
2(2)	6.0	269	497 ± 169	7558 ± 469	2.27 ± 0.01	-	3.47	2021 ± 212	-	321 ± 4	-	74 ± 23	3.2 ± 0.2	20.6 ± 24.8	534 ± 15	14.9
3(3)	6.0	269	444 ± 121	8119 ± 654	2.2 ± 0.09	-	2.78 ± 0.24	3064 ± 1451	-	466 ± 139	221.5	136.8 ± 60.2	3.1 ± 0.9	21.7 ± 8.2	623 ± 55	15.1 ± 1.2
4(2)	6.0	291	412 ± 30	7033 ± 309	2.25 ± 0.01	-	3.19 ± 1.07	2280 ± 240	-	282 ± 23	-	94.5 ± 3.7	1.8 ± 0.5	16.4 ± 1.9	505 ± 32	4 ± 1.3
5(2)	6.0	264	340 ± 19	8875 ± 26	2.23 ± 0.03	2389	3.27 ± 1.81	2553 ± 573	-	382 ± 19	3.3	112.5 ± 33.4	3.8 ± 0.1	13.7 ± 4.6	640 ± 21	17.9 ± 3.3
6(2)	6.1	273	556 ± 24	7179 ± 1366	2.29 ± 0.01	-	3.59 ± 1.21	1929 ± 307	-	428 ± 102	12.9	196 ± 115	3.6 ± 0.8	20.8 ± 0.5	558 ± 29	7.4 ± 0.9
7(4)	6.0	267	391 ± 124	10862 ± 4446	2.25 ± 0.02	1931	3.06 ± 0.81	2283 ± 376	-	344 ± 98	6	138.6 ± 48.9	4.4 ± 1	9.5 ± 3	647 ± 193	9.6 ± 3.8
8(4)	6.0	269	430 ± 7	6070 ± 1550	2.25 ± 0.03	2002 ± 82	2.33 ± 0.48	2233 ± 535	-	305 ± 56	51.4 ± 58	113.7 ± 9.9	3.1 ± 0.6	78 ± 119.1	512 ± 83	6.4 ± 2.6
9(4)	6.1	261	349 ± 36	8509 ± 137	2.3 ± 0.02	1984 ± 446	2.91 ± 0.32	1856 ± 236	-	429 ± 53	21.8	112.8 ± 14.9	4.1 ± 0.1	13.8 ± 3.6	675 ± 97	13.5 ± 3.3
10(2)	6.1	244	367 ± 90	9887 ± 322	2.38 ± 0.03	2026	4.8 ± 2.55	375 ± 41	-	359 ± 55	15	39.9 ± 19.6	1.5 ± 0.4	11.6	619 ± 203	6.5 ± 5.8
11(5)	6.2	258	353 ± 33	8693 ± 1257	2.35 ± 0.05	3016 ± 2205	3.25 ± 0.77	1189 ± 415	-	418 ± 147	9.4 ± 7.9	81.2 ± 32.3	3.7 ± 0.7	9.8 ± 4.1	656 ± 151	9.1 ± 2.7
12(3)	6.3	264	404 ± 139	7841 ± 1203	2.45 ± 0.01	3186	3 ± 0.85	431 ± 90	-	347 ± 70	7.3	32.7 ± 8.3	2.3 ± 0.5	25.1 ± 9	555 ± 28	11.4 ± 2.2

13(9)	6.2	266	383 ± 45	8356 ± 729	2.33 ± 0.01	2032 ± 793	2.67 ± 0.3	1530 ± 181	14.7	381 ± 50	27.6 ± 48	88.1 ± 20.5	4.1 ± 1.1	30 ± 32.1	604 ± 29	8.6 ± 3.7
14(2)	6.2	256	369 ± 94	8692 ± 682	2.37	-	2.87 ± 0.32	861 ± 6	-	349 ± 21	6.1	46.3 ± 14.7	3.1 ± 0.1	12.7 ± 4.7	575 ± 20	11.5 ± 0.7
15(5)	6.2	250	297 ± 57	8721 ± 968	2.39 ± 0.01	2121	2.66 ± 0.35	527 ± 120	-	385 ± 204	13.2	53 ± 9.9	2.3 ± 1.1	6.4 ± 2.7	659 ± 74	8 ± 2.9
16(3)	6.2	259	352 ± 199	8106 ± 478	2.34 ± 0.09	2616 ± 135	2.65 ± 0.5	479 ± 7	8.4	404 ± 40	81.5 ± 111	54.9 ± 1.4	2 ± 0.3	42.1 ± 13.9	626 ± 49	4.7 ± 0.4
17(3)	6.3	264	303 ± 108	8549 ± 669	2.46	1918	3.08 ± 0.3	337 ± 74	-	358 ± 29	32	30.6 ± 7.8	1.5 ± 1.1	25.1 ± 15.5	556 ± 59	7.9 ± 7
18(5)	6.3	265	359 ± 60	7913 ± 459	2.42 ± 0.02	1542	3.24 ± 0.62	923 ± 347	5.9	343 ± 53	11.5 ± 7.4	54.1 ± 28.3	2.7 ± 1.1	30.6 ± 33.5	602 ± 47	8.6 ± 3.2
19(2)	6.3	276	348 ± 40	7453 ± 8	2.4 ± 0.05	2830 ± 344	3.28 ± 0.13	1354 ± 901	14 ± 10.5	412 ± 99	31.1	95 ± 18.9	3.2 ± 1	54.3 ± 32.6	591 ± 101	11.3 ± 3.6
20(2)	6.3	275	313 ± 50	7836 ± 215	2.45 ± 0.01	1999 ± 511	2.76 ± 0.08	476 ± 98	16.1	369 ± 34	41.9 ± 38.2	39.2 ± 8.1	1.7 ± 0.1	58 ± 45	542 ± 6	9.9 ± 1
21(3)	6.4	258	505 ± 238	7422 ± 197	2.41 ± 0.03	2095 ± 559	3.35 ± 0.46	1420 ± 298	-	336 ± 31	-	67.8 ± 10.6	3.5 ± 0.6	10.3 ± 8.5	611 ± 175	6.2 ± 5.1
22(3)	6.3	273	430 ± 17	7794 ± 304	2.38 ± 0.02	2230 ± 644	2.82 ± 0.4	1656 ± 255	10.6 ± 3.5	347 ± 27	81.2 ± 129	86.7 ± 11	3.1	67.1 ± 72.9	628 ± 30	5.3 ± 4.2
23(6)	6.5	281	451 ± 165	8000 ± 746	2.45 ± 0.04	3151 ± 1173	3.54 ± 0.6	1437 ± 736	18	444 ± 85	53.9 ± 32.4	70 ± 29.2	5.1 ± 2.5	109.1 ± 101	649 ± 127	14.7 ± 5.3
24(5)	6.3	291	450 ± 74	7881 ± 512	2.31 ± 0.1	-	2.72 ± 0.13	2429 ± 788	-	328 ± 33	95.5 ± 29.8	121.1 ± 51.2	3.7 ± 1.9	61.9 ± 22.6	585 ± 59	10.1 ± 4.1
26(4)	6.4	271	449 ± 95	8011 ± 2408	2.37 ± 0.11	3663 ± 1517	3.03 ± 0.38	2084 ± 902	-	468 ± 183	86.1 ± 33.5	88.3 ± 27.6	3.6 ± 0.4	34.5 ± 23.4	569 ± 74	6.6 ± 4.1
27(3)	6.5	267	481 ± 12	8487 ± 1083	2.43 ± 0.06	1758	2.98 ± 0.47	1759 ± 975	-	339 ± 34	60.7 ± 7.8	92.7 ± 37.9	3.2 ± 1.9	51.6 ± 21.6	633 ± 14	12.9 ± 0.7
31(3)	6.2	266	307 ± 59	7822 ± 849	2.39	2274 ± 259	3.33 ± 0.88	492 ± 29	4.7	385 ± 27	3.3 ± 1.7	54.3 ± 11.4	1.9 ± 0.4	38.3 ± 6.5	626 ± 67	8 ± 1.4
32(4)	6.2	257	369 ± 112	8982 ± 530	2.39 ± 0.01	2400 ± 593	3.24 ± 0.11	487 ± 124	14.4	403 ± 82	15.8 ± 13.9	55.8 ± 9.8	1.4 ± 1.2	27.6 ± 13	644 ± 91	5.5 ± 1.5
34(4)	6.0	275	279 ± 88	6804 ± 500	2.27 ± 0.01	2342 ± 847	2.59 ± 0.31	1557 ± 242	11.7 ± 1.9	509 ± 72	11.9 ± 10.8	117.5 ± 25.4	1.2 ± 0.2	11.5 ± 8.8	633 ± 52	5.9 ± 7
35(4)	6.0	270	336 ± 43	8146 ± 283	2.27	2870 ± 433	2.97 ± 0.47	1687 ± 63	19.8 ± 8.5	549 ± 235	65 ± 49.7	138.6 ± 29.1	1.4 ± 0.6	12.3 ± 9.4	671 ± 67	1.6 ± 0.8
37(2)	5.9	292	385 ± 19	7443 ± 190	2.31 ± 0.03	3176 ± 923	2.72 ± 0.17	427 ± 183	14.6	469 ± 202	473 ± 378	41.1 ± 24	0.3 ± 0.1	133.9 ± 127	521 ± 96	29.2
38(3)	6.0	246	393 ± 75	8096 ± 70	2.34 ± 0.06	1917 ± 83	2.71 ± 0.15	353 ± 81	13.7	380 ± 239	76 ± 79	53.6 ± 14.7	0.8 ± 0.4	16 ± 13.2	591 ± 119	7.4 ± 8.1
39(3)	5.9	262	149 ± 24	5717 ± 2785	2.29 ± 0.01	887	2.21 ± 0.92	309 ± 108	-	453 ± 152	104 ± 92	46 ± 24.8	0.1	42 ± 39.7	477 ± 141	4.8 ± 1.1
40(3)	6.1	259	361 ± 153	6730 ± 684	2.35 ± 0.1	1604 ± 429	2.94 ± 0.33	951 ± 191	-	332 ± 100	11.8 ± 6	71.1 ± 17.9	2.7 ± 1.7	25 ± 18.5	475 ± 141	2.5 ± 0.9
41(3)	6.3	297	323 ± 27	7225 ± 1069	2.44 ± 0.18	1974 ± 260	2.59 ± 0.25	423 ± 89	9.6 ± 0.2	582 ± 246	193 ± 80	46.9 ± 14.8	0.1 ± 0.1	92.3 ± 55.9	480 ± 96	3.2 ± 3.3
42(2)	6.6	279	298 ± 18	6382 ± 438	2.57 ± 0.16	1853	2.78 ± 0.02	417 ± 52	10 ± 0.1	314 ± 91	28 ± 24.5	48 ± 2.8	1.7 ± 0.9	26.9 ± 28.2	537 ± 138	1.6 ± 0.3
43(6)	5.9	265	368 ± 70	7208 ± 920	2.29	2314 ± 628	2.5 ± 0.31	322 ± 71	15.4 ± 13	456 ± 81	128 ± 147	51.4 ± 7.2	0.2 ± 0.1	103 ± 211.4	569 ± 76	14.9 ± 14.4
44(4)	6.0	280	339 ± 109	7666 ± 822	2.34	2125	2.81 ± 0.36	385 ± 66	-	358 ± 41	45 ± 20	40.1 ± 3.9	1.1 ± 0.6	61.4 ± 30.5	546 ± 43	12.2 ± 3.4

62(2)	6.2	258	506 ± 160	10635 ± 2429	2.26 ± 0.04	2841	4.08 ± 1.51	3205 ± 21	-	187 ± 10	15.5 ± 2.2	133.9 ± 16.2	4.9 ± 0.1	22.7 ± 2.8	705 ± 99	5.4 ± 0.9
67(1)	6.6	278	242	9264	2.38	1607	3.07	3658	-	234	25.2	182.6	3.9	68.3	446	-
70(2)	5.9	261	351 ± 53	7662 ± 1641	2.18 ± 0.03	-	3.18 ± 0.07	2053 ± 531	-	256 ± 90	55.6 ± 4.9	120.2 ± 4.7	6.3 ± 0.6	41.4 ± 1.1	491 ± 77	10.1
73(2)	6.0	264	408 ± 84	9890 ± 1819	2.17 ± 0.05	-	5.3	3300 ± 782	-	293 ± 94	37.6	146 ± 28.6	7.4 ± 3.3	33.3 ± 18.1	795 ± 397	10.7 ± 1
77(4)	5.9	233	797 ± 344	8207 ± 1241	2.31 ± 0.06	1917 ± 233	4.11 ± 0.66	468 ± 195	10.7 ± 2.8	218 ± 58	-	55.6 ± 6.5	1.5 ± 1.4	18.7 ± 16.9	601 ± 110	1.6 ± 1
78(4)	6.3	238	583 ± 68	7112 ± 984	2.44 ± 0.08	1215	3.29 ± 0.5	520 ± 166	13.9 ± 11	151 ± 22	2	48.1 ± 6.7	2 ± 1.1	11 ± 7.4	483 ± 16	3.2 ± 1.8

Pseudosecondary FIAs in Qtz 3 (*PS3 type, N=11*)

28(3)	5.5	263	503 ± 114	398 ± 72	2.07 ± 0.08	-	3.33 ± 0.64	1360 ± 275	-	4.6	-	33.7 ± 9.4	29.9 ± 2.6	34.2 ± 9.1	311 ± 53	12.6 ± 2.4
29(4)	5.5	261	387 ± 71	411 ± 73	2.08 ± 0.07	-	4.1 ± 1.06	1617 ± 800	20.1	1.8	-	36.3 ± 24.9	25.7 ± 15.3	76.9 ± 10	265 ± 93	21.9 ± 11.6
30(4)	5.1	252	367 ± 8	437 ± 48	1.93 ± 0.04	-	2.55 ± 0.27	1539 ± 375	4.2	9 ± 1.2	-	44.6 ± 14	34.1 ± 9	34.6 ± 6.4	327 ± 21	5.1 ± 6
53(2)	7.3	277	523 ± 11	749 ± 80	2.64 ± 0.04	-	4.22 ± 0.1	3979 ± 633	15.5	16.9 ± 4	-	123.7 ± 30.2	71.1 ± 0.5	81.4 ± 1.7	734 ± 77	1.2 ± 0.1
57(1)	5.4	265	272	443	1.99	-	3.95	2279	-	4.7	-	44.4	33.7	34.7	343	1.9
61(2)	6.5	272	455 ± 106	490 ± 17	2.45 ± 0.01	-	3.63 ± 0.68	1469 ± 196	61.5	3.7	-	21.6 ± 6.2	39.7 ± 3.9	60.8 ± 13	372 ± 7	168.9
63(2)	7.3	283	523 ± 92	756 ± 3	2.68 ± 0.03	-	4.33 ± 0.18	3282 ± 481	13.9	16.3 ± 2.1	-	107.1 ± 12.8	78.3 ± 13	72.1 ± 9.3	704 ± 73	1.8 ± 0.3
65(3)	8.4	291	562 ± 136	718 ± 180	3.19 ± 0.19	-	5.4	1908 ± 404	-	30.9	-	48.3 ± 18.2	95.7 ± 5.2	101 ± 11.7	669 ± 49	10.5
69(2)	8.3	309	405 ± 37	92 ± 18	3.12 ± 0.03	-	5.17 ± 0.29	2421 ± 561	10.5 ± 3.4	-	0.6	36.3 ± 10.1	261 ± 46	3.1 ± 1.2	293 ± 10	1.6 ± 1.8
72(2)	5.6	269	274 ± 11	446 ± 10	2.15 ± 0.17	-	2.66 ± 0.14	1103 ± 722	26.7	5.9	3.3	22.5 ± 19.1	40.9 ± 21.7	57.8 ± 8.7	353 ± 37	1.2 ± 0.3
76(2)	5.2	250	387 ± 157	468 ± 495	1.93 ± 0.01	-	2.48 ± 0.56	1823 ± 495	-	4.2	-	42.9 ± 19.6	49 ± 7.3	11.4 ± 3.9	283 ± 86	1.6 ± 0.7

Notes: Data obtained from LA-ICP-MS analysis are presented as average values of each fluid inclusion assemblage with 1 standard deviation (± σ). Standard deviation for salinity and Th of each FIA can be found in Table S2. The absolute compositions were calculated without including boron in the salt correction, so that all elemental concentrations in fluid inclusions with higher boron contain (i.e. Ps1-2) can be overestimated by up to 50 %. Concentrations of other elements e.g. Mg, Al, Ca, Fe, Br, Zn, Sn and Pb refer to Table S2; '-' = all individual inclusion in FIA have values below detection limit; n.d. = not determined.

[1] Number of individual fluid inclusions analyzed in each fluid inclusion assemblage.

[2] Apparent salinities of fluid inclusions in wt. % NaCl equiv.